

CLOSE COMPANIONS TO YOUNG STARS. I. A LARGE SPECTROSCOPIC SURVEY IN CHAMAELEON I AND TAURUS-AURIGA

DUY CUONG NGUYEN^{1,2,3}, ALEXIS BRANDEKER^{1,2}, MARTEN H. VAN KERKWIJK¹, RAY JAYAWARDHANA¹

Received 2011 August 25; accepted by ApJ 2011 November 29

ABSTRACT

We present the results of a multiplicity survey of 212 T Tauri stars in the Chamaeleon I and Taurus-Auriga star-forming regions, based on high-resolution spectra from the Magellan Clay 6.5 m telescope. From these data, we achieved a typical radial velocity precision of $\sim 80 \text{ m s}^{-1}$ with slower rotators yielding better precision, in general. For 174 of these stars, we obtained multi-epoch data with sufficient time baselines to identify binaries based on radial velocity variations. We identified eight close binaries and four close triples, of which three and two, respectively, are new discoveries. The spectroscopic multiplicity fractions we find for Cha I (7%) and Tau-Aur (6%) are similar to each other, and to the results of field star surveys in the same mass and period regime. However, unlike the results from imaging surveys, the frequency of systems with close companions in our sample is not seen to depend on primary mass. Additionally, we do not find a strong correlation between accretion and close multiplicity. This implies that close companions are not likely the main source of the accretion shut down observed in weak-lined T Tauri stars. Our results also suggest that sufficient radial velocity precision can be achieved for at least a subset of slowly rotating young stars to search for hot Jupiter planets.

Subject headings: binaries: spectroscopic — binaries (including multiple): close — stars: pre-main-sequence — stars: formation — stars: low-mass, brown dwarfs — stars: statistics — methods: data analysis — line: profiles — planetary systems

1. INTRODUCTION

Most stars, both in the solar neighborhood and in young clusters are members of binary or multiple systems. Yet, the formation and early evolution of binary and multiple stars is poorly constrained observationally, and not well understood theoretically. For instance, the fraction of wide binaries in dense star-forming regions such as the Orion Nebula Cluster and IC 348 are comparable to that of field stars (Duchêne et al. 1999; Köhler et al. 2006) whereas the frequency of binaries is much higher among young stars in dispersed T associations like Taurus-Auriga (e.g., Simon et al. 1995; Ghez et al. 1997a; Brandeker et al. 2003); for reviews see Mathieu et al. (2000) and Duchêne et al. (2007). Furthermore, high-order multiples are more common in nearby star-forming regions than for solar-type main-sequence stars in the solar neighborhood (Correia et al. 2006).

Some simulations suggest that stars usually form in triples and higher-order multiple systems only to be dispersed later, with the fraction of stars in multiple systems decreasing from 80% down to 40% by about 10 Myrs (Delgado-Donate et al. 2004). Predictions are that the binary fraction is higher among higher mass stars, and that brown dwarfs are never close companions to stars (Goodwin et al. 2004).

While past multiplicity surveys, using speckle imaging and adaptive optics on 4-m class telescopes, have drawn attention to the ubiquity of binaries in star-forming regions (e.g., Ghez et al. 1993; Leinert et al. 1993), their limited contrast and angular resolution have left many key questions unanswered or only partially answered. For instance, the frequency of higher-order multiples is uncertain, and so is the frequency of very low-mass stellar and sub-stellar companions (Ahmic et al. 2007). Multiple systems are probably common.

With adaptive optics on 8-m class telescopes, it has become straightforward to detect all stellar and even all brown dwarf companions down to the deuterium-burning limit with separations of tens of AU for nearby young stars (e.g., Lafrenière et al. 2008). Like Maxted et al. (2008), our radial velocity study is complementary and covers the close separations.

We present the results of a high-resolution spectroscopic survey of 212 stars spanning $\sim 0.2\text{--}3 M_{\odot}$ in the nearby ~ 2 Myr old star-forming regions Chamaeleon I (hereafter Cha I) and Taurus-Auriga (hereafter Tau-Aur). Cha I and Tau-Aur are at distances of ~ 160 pc and ~ 140 pc, respectively (Whittet et al. 1997; Kenyon et al. 1994). Previously, we presented a study of rotation, disk, and accretion signatures for a subsample of 144 stars showing no evidence of spectroscopic companions and broadening functions showing only a single source (Nguyen et al. 2009a); we use the derived projected rotational velocities ($v \sin i$) and accretion signatures ($H\alpha$ 10% width) for this work. Furthermore, we also analyzed the variability in accretion-related emission lines for a subsample of 40 classical T Tauri stars (Nguyen et al. 2009b). Lafrenière et al. (2008) presented a census of wide binaries in Cha I that encompasses

Electronic address: dcnguyen@pas.rochester.edu

¹ Department of Astronomy & Astrophysics, University of Toronto, 50 St. George Street, Toronto, ON M5S 3H4, Canada; nguyen, mhvk, rayjay@astro.utoronto.ca

² Department of Astronomy, Stockholm University, SE-106 91 Stockholm, Sweden; duy.nguyen, alexis@astro.su.se

³ Current address: Department of Physics and Astronomy, University of Rochester, Rochester, NY 14627-0171, USA; dcnguyen@pas.rochester.edu

our sample while Damjanov et al. (2007) investigated circumstellar disks, including the effect of companions on disks, for a subsample of Cha I targets with available near-IR data.

Among the issues we address in this work is the dependence of multiplicity on primary mass, i.e., whether higher mass stars are more likely to be in binaries and multiples than their lower mass counterparts. An increase in wide binaries with increasing mass has been observed for both young stars and field dwarfs (e.g., Kraus & Hillenbrand 2007; Lafrenière et al. 2008). Furthermore, we look at how close-in multiplicity varies between different star-forming regions and the field; the multiplicity of $\sim 0.1\text{--}2 M_{\odot}$ field dwarfs in the solar neighborhood has been studied extensively (e.g., Duquennoy & Mayor 1991; Fischer & Marcy 1992; Raghavan et al. 2010). We also explore whether close companions contribute to the observed difference between classical T Tauri stars (CTTS), which are accreting, and weak-lined T Tauri star (WTTS), which are not accreting based on weak H α emission. Although the source of dichotomy between CTTS and WTTS is currently unknown, the presence of non-accreting 2 Myr old stars is surprising. It has been suggested that the inner disks around weak-lined objects may have been truncated by close binary companions (e.g., Mathieu et al. 2000, and references therein).

2. OBSERVATIONS

Our star sample consists of a magnitude-limited subset ($R \leq 17.6$ for Cha I; $R \leq 13.4$ for Tau-Aur) of targets from Luhman (2004a) for Cha I, and from Leinert et al. (1993), Ghez et al. (1993), Simon et al. (1995), Kohler & Leinert (1998), Briceño et al. (2002) and Luhman (2004b) for Tau-Aur. Our targets span the spectral type range from F2 to M5 based on published classifications. In addition, we observed a sample of 25 slowly rotating velocity standard stars selected from the list of Nidever et al. (2002); these are listed in Table 1 and cover a similar spectral range to our targets. We determined the spectral type for 13 targets without prior classification by fitting their spectra against those of the standard stars, and identifying the best fits.

Our data were taken using the echelle spectrograph MIKE (Bernstein et al. 2003) on the Magellan Clay 6.5-m telescope at the Las Campanas Observatory, Chile. The MIKE instrument is a slit-fed double echelle spectrograph with blue and red arms. For this study, we used only the red region spanning 4 800–9 400 Å in 32 spectral orders. The 0.35'' slit was used with no binning to obtain the highest possible spectral resolution, $R \sim 60\,000$. The pixel scale was 0.14'' pixel $^{-1}$ in the spatial direction, and approximately 0.024 Å pixel $^{-1}$ at 6 500 Å in the spectral direction. The raw data were bias-subtracted and flat-fielded, and before extraction, the scattered background in the spectrograph was subtracted by fitting splines to inter-order pixels. Note that no sky subtraction is done as part of our extraction. For the bright stars studied by Brandeker et al. (in preparation), the sky background is generally insignificant compared to the stellar spectrum, but for the fainter among our targets it is not. As we will discuss below, this generally does not pose a problem for our purpose of inferring binarity. In MIKE, the spatial direction of the projected slit is wavelength de-

TABLE 1
SLOWLY ROTATING RADIAL VELOCITY
STANDARD STARS USED AS TEMPLATES

Name	Spectral Type	RV^a (km s $^{-1}$)
GJ 156	K7	62.597
GJ 729	M3.5	-10.499
G1 205	M1.5	8.665
G1 349	K3	29.836
G1 382	M1.5	7.932
G1 876	M4	-1.591
G1 880	M1.5	-27.317
HD 103932	K4	48.499
HD 111631	K7	5.041
HD 120467	K5.5	-37.806
HD 153458	G0	0.641
HD 172051	G6	37.103
HD 193901	F7	-171.455
HD 217987	M0.5	8.809
HD 83443	K0	28.994
HD 87359	G5	-0.26
HD 88218	G0	36.652
HD 90156	G5	26.934
HD 91638	F8	-4.751
HD 92945	K1.5	22.856
HD 96700	G0	12.769
HR 5447	F2	0.141
LHS 1763	K5	-55.527
NSV 2863	M1	4.724
NSV 6431	M2	15.809

^a Radial velocities are adopted from Nidever et al. (2002).

pendent, and not aligned with the CCD columns. To extract these slanted spectra, we used customized routines running in the ESO-MIDAS environment (described in detail in Brandeker et al., in preparation). For wavelength calibration, we used exposures of a thorium-argon lamp as well as observed telluric absorption lines. Integration times were chosen such that we obtained signal-to-noise ratios (S/N) > 30 per spectral resolution element at 6 500 Å; they typically ranged from 60 to 1 200 seconds depending on seeing. We also applied barycentric correction to all spectra.

We obtained 813 high-resolution optical spectra of 212 members of the Cha I and Tau-Aur star-forming regions. The data were collected on 15 nights during four observing runs between 2006 February and 2006 December.

3. ANALYSIS TECHNIQUES

To find close binaries and higher-order multiples in our sample, we used both broadening function and radial velocity analysis. The former was used to identify double-lined spectroscopic binaries (hereafter SB2s) and triple-lined spectroscopic binaries (hereafter SB3s); these systems are characterized by multiple prominent peaks in their broadening functions. The latter was used to detect single-lined spectroscopic binaries (hereafter SB1s); acceleration would be suggested by significant radial velocity scatter in our data. Both analyses involved fitting the target spectra with comparison spectra to minimize χ^2 ,

$$\chi^2 \equiv \sum_i \left(\frac{Y(\lambda_i) - P(\lambda_i)}{\sigma(\lambda_i)} \right)^2 \quad (1)$$

where Y and σ are the fluxes and uncertainties of the

target spectra, respectively, and P are the fluxes of the comparison spectra. The comparison spectra are produced using template spectra from the observed slowly rotating velocity standard stars. To match a standard star with each target star, we examined the spectra from the three standard stars closest in spectral type to the target, and selected the standard star spectrum that best fits that of the target. For the fits, we masked telluric absorption lines, Li- λ 6708, which is present in young stars but absent in our standard stars, and activity-related emission lines H α , H β , Pa6 through 9, Pa11, Pa14, He I (λ 5876, λ 6678, λ 7065), O I (λ 7774, λ 8446, λ 8456), [O I] (λ 5577, λ 6300, λ 6364), Na I D doublet, Ca II IR triplet, and Fe II 42 multiplet from the spectra. We used χ^2 analysis instead of Fourier techniques for SB1s, or TODCOR techniques (Zucker & Mazeh 1994) for SB2s and SB3s to take advantage of uncertainties at each individual wavelength. We processed data for each echelle order separately to avoid discontinuities resulting from poorly corrected blaze, and combined the output to get our results.

3.1. Broadening Functions

The broadening functions of each target were derived based on the technique described in Rucinski (1999). Our implementation involves computing the discrete broadening function $B(v_j)$ that minimizes χ^2 in Eq. 1 for,

$$P(\lambda_i) = \left[\sum_j B(v_j) \cdot S((1 + v_j/c)\lambda_i) \right] \cdot C(\lambda_i) \quad (2)$$

where B is the broadening function, S is the template spectrum from a slowly rotating standard star, and C is the best-fit polynomial to the continuum. Here, the broadening function is essentially an estimate of the average line profile for a given spectrum.

Our routine to derive the broadening function of a target at a given epoch consists of two steps. First, for each echelle order, we fit the target spectra with comparison spectra to produce a broadening function spanning -120 to $+120 \text{ km s}^{-1}$ with a sampling interval of 6 km s^{-1} . This interval is close to the velocity resolution of the spectrograph, and reduces possible covariance between points from oversampling. Second, we compute the weighted mean of the broadening function across the echelle orders.

For targets that were later identified as SB2 or SB3 candidates, we fit the multiple peaks of their broadening functions with an equal number of analytic rotational broadening functions from Gray (2005) in order to measure their component radial velocities, flux ratios and $v \sin i$. Note, due to our sampling resolution, this technique has a $v \sin i$ lower limit of $\sim 9 \text{ km s}^{-1}$. Furthermore, for well-blended or wide broadening functions, the radial velocity precision is poor using this technique, typically a few 100 m s^{-1} . Thus, for single-peak broadening functions, we rely mostly on radial velocities computed directly from spectra as described in §3.2.

3.2. Radial Velocities

The radial velocities of each target were computed by fitting the target spectra with series of velocity

shifted comparison spectra. This technique computes the velocity shift v_* that minimizes χ^2 in Eq. 1 for,

$$P(\lambda_i, v_*) = (G(v \sin i) * S)[(1 + v_*/c)\lambda_i] \cdot C(\lambda_i) \quad (3)$$

where G is the analytic rotational broadening function from Gray (2005) assuming a limb darkening coefficient of 0.65, $v \sin i$ is the projected rotational velocity of the target star, S is the template spectrum from a slowly rotating standard star, and C is the best-fit polynomial to the continuum. The projected rotational velocity for each target star was computed by fitting the target spectra with a series of template spectra rotationally broadened from 0 to 200 km s^{-1} , and calculating the best fit value (see Nguyen et al. 2009a).

Our routine to estimate the radial velocity of a target at a given epoch consists of four steps. First, for each echelle order, we fitted the target spectra with comparison spectra velocity shifted from -120 to $+120 \text{ km s}^{-1}$ in steps of 10 km s^{-1} , and recorded the velocity value of the best fit for each echelle order. Second, we refined our search to radial velocities within 10 km s^{-1} of the first-pass results in steps of 0.01 km s^{-1} , and revised our estimates accordingly. Third, comparing the results for different orders, we removed outliers using a standard Tukey filter, i.e., values lying 1.5 times the interquartile range below the first quartile and above the third quartile were discarded (see Hoaglin et al. 2000). For a Gaussian distribution, this filter corresponds to removing data points beyond 2.7σ . Fourth, we computed the weighted mean and the associated error in the mean across the echelle orders, and used those values as the radial velocity and measurement uncertainty of the target at that epoch, respectively.

For some targets with heavily veiled spectra (e.g., DR Tau), this technique did not produce consistent radial velocity results. In these cases, we derived the radial velocities by fitting analytic rotational broadening functions to the computed broadening functions (see §3.1), but corrected for veiling. This correction involved adding to Eq. 2 a linear component alongside the rotational broadening function to estimate and account for the contribution from veiling. Furthermore, we considered the overall potential influence of accretion and veiling on our radial velocity estimates by comparing both the estimated radial velocity measurement uncertainties and scatter within the observing runs against the accretion signature H α 10% width (see §5.1). This comparison is illustrated in Fig. 1 & 2. There appears to be no significant difference in the radial velocity measurement uncertainties nor the radial velocity scatter within the observing runs between accretors and non-accretors in Cha I and Tau-Aur.

The aggregated radial velocity results along with stellar characteristics such as spectral type, H α 10% width, and $v \sin i$ for our sample are listed in Tables 2 & 3. The reported radial velocities for our targets incorporate the radial velocities and artificial rotational broadening of the templates. Additional information including brief comments and plots of several spectral lines for each object are provided in Fig. 10 through 37. For a more detailed description of these figures, see §6.

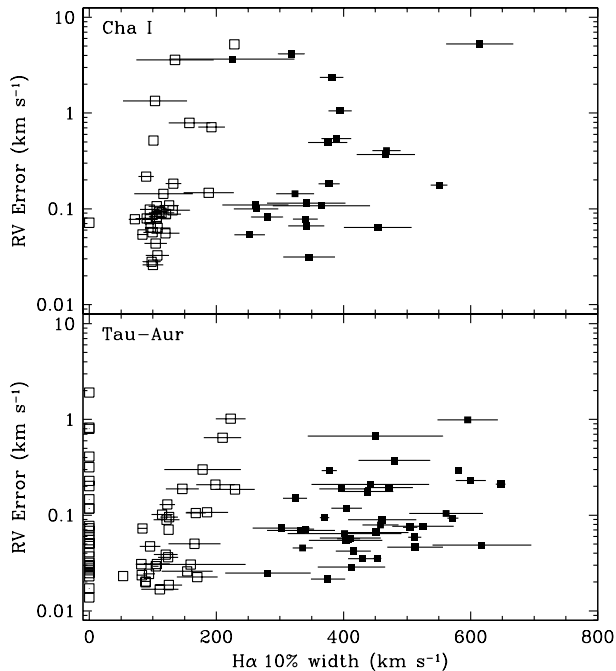


FIG. 1.— The weighted mean radial velocity measurement uncertainty for members of Cha I and Tau-Aur with single-peak broadening functions as a function of the accretion signature $H\alpha$ 10% width. Accretors and non-accretors are denoted by solid and hollow symbols, respectively. There appears to be no significant difference in the radial velocity measurement uncertainties between accretors and non-accretors.

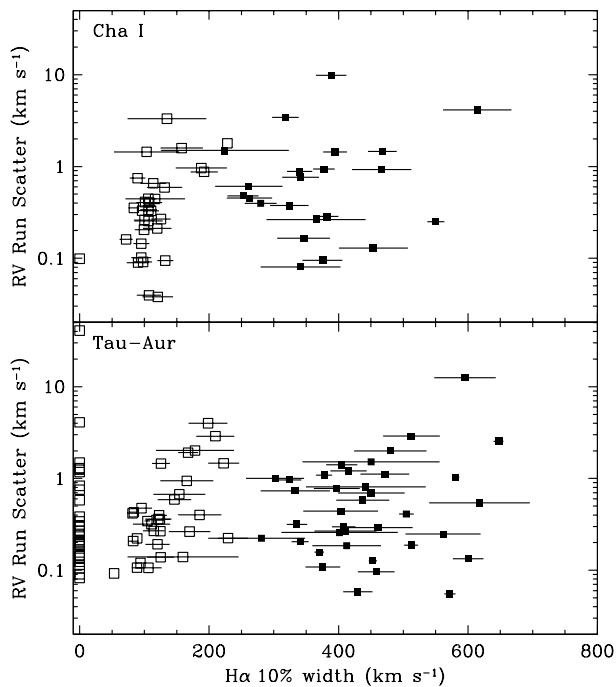


FIG. 2.— Radial velocity scatter within the observing runs for members of Cha I and Tau-Aur with single-peak broadening functions as a function of the accretion signature $H\alpha$ 10% width. Accretors and non-accretors are denoted by solid and hollow symbols, respectively. There appears to be no significant difference in the radial velocity scatter within the observing runs between accretors and non-accretors.

4. IDENTIFYING CLOSE COMPANIONS

Our approach to identifying close companions consists of two basic parts. First, we checked the broadening functions of each star for multiple peaks suggestive of SB2s. Second, we examined the radial velocity measurements for variations consistent with SB1s.

4.1. SB2 Candidates

We identified SB2 candidates as targets that have broadening functions with prominent multiple peaks that cannot be accounted for by non-companion sources (e.g., see V826 Tau; Fig. 16). Plausible non-companion sources include sky or moon contamination, and contribution from a known resolved companion. We discuss these influences below.

An extra peak near the observer's rest frame could be attributed to possible contamination from moonlight or twilight sky. This occurs commonly in our data, since we did not correct for sky in our reduction (see §2). To assess this contamination, we checked the angular distance of the target to the moon and the altitude of the sun below the horizon at the time the data were taken, and we inspected the raw data frames.

Additional peaks in the broadening function may be caused by light from nearby resolved companions. We collected information on known visual binaries by cross-referencing our target list with those of speckle and direct imaging surveys: for Cha I, we used Lafrenière et al. (2008), and for Tau-Aur we checked Leinert et al. (1993), Ghez et al. (1993), Simon et al. (1995), Ghez et al. (1997b), and Kohler & Leinert (1998). To gauge the significance of the visual binaries on the broadening functions, we used the ΔK magnitudes and K -band flux ratios reported in the surveys to calculate corresponding R -band flux ratios. This calculation consists of the following eight steps:

1. Use the spectral type of the targets to estimate effective temperatures T_{eff} (Sherry et al. 2004).
2. With T_{eff} , compute luminosities L from the models of D'Antona & Mazzitelli (1997).
3. With L , compute bolometric magnitudes $M_{\text{bol}} = 4.75 - 2.5 \log(L/L_{\odot})$.
4. Use the spectral type of the targets and the color-temperature relation of Sherry et al. (2004) to compute the bolometric correction BC , and the $V-R$ and $V-K$ colors of the primary stars.
5. Combine the above to calculate the absolute R and K magnitudes of the primary stars.
6. Apply the reported ΔK magnitudes and K -band flux ratios of the systems to derive the absolute K magnitudes of the companions.
7. Use these absolute K magnitudes to estimate the corresponding absolute R magnitudes by interpolating the color-temperature relation of Sherry et al. (2004).
8. Combine the derived absolute R magnitudes of the primary stars and the companions to find the R -band flux ratios of the systems.

Obviously, the above calculation relies on numerous assumptions, and the resulting estimated R -band flux ratios are thus only approximate. However, they suffice for our purpose of gauging whether a significant contribution to the broadening function from a resolved companion is likely.

Our ability to identify SB2 candidates from the broadening functions is limited by several factors. First, the contribution of companions to the broadening function must be sufficiently large to discriminate them from their primary stars. The SB2 candidates we could identify had a flux ratio lower bound of ~ 0.1 . Second, the radial velocity separation of component stars with similar $v \sin i$ must be large enough to distinguish each star in the broadening function. The minimum measurable velocity separation is equal to the sampling interval of 6 km s^{-1} ; however, we find empirically the lower limit of the velocity separation for our identified SB2 candidates is $\sim 10 \text{ km s}^{-1}$. Note, resolved companions are generally in long-period orbits, and thus, the radial velocity separation between the host and the companion is usually small, and the peaks in the broadening function from the pair would likely overlap. Moreover, overlapping contributions from two sources would produce an additional sharp central peak in the broadening function, thus a lack of this feature excludes some targets with only two wide peaks, e.g., T20 and HD 283572, from being identified as SB2s due to bad model fitting. Third, the $v \sin i$ of the component stars with similar radial velocities must be large enough to distinguish each star in the broadening function. For example, see the broadening function of DF Tau in Fig. 29, the two component stars have similar radial velocities and could only be distinguished because of the significant difference in $v \sin i$ between them. Among applicable SB2 candidates, the smallest difference between component star $v \sin i$ is $\sim 24 \text{ km s}^{-1}$.

We identified thirteen SB2s, four suspected SB2s, and four SB3s in our sample. Of the thirteen SB2s, five show significant acceleration based on their broadening functions whereas the other eight display no remarkable radial velocity changes. We re-labeled these latter objects as long-period SB2s. For seven out of the eight long-period SB2s, resolved companions are likely the source of the secondary peaks in their broadening functions, and thus, they are also visual binaries. The one remaining long-period SB2, RX J0443.4+1546, could have a binary separation of a few AU, which would be smaller than can be currently resolved by imaging techniques but large enough not to show a significant change in radial velocity over the time baseline of our observations. The sets of radial velocity measurements for all candidate and suspected SB2s, and SB3s are listed in Tables 4 & 5.

4.2. SB1 Candidates

We identified SB1 candidates as targets that have radial velocity scatter that cannot be accounted for by noise (e.g., see RX J0415.8+3100; Fig. 21). We consider not only measurement noise but also possible intrinsic noise from the star. Of particular relevance are apparent radial velocity changes due to spots, which effectively attenuate light from part of the star. Combined with rotation, this leads to apparent velocity changes on cycles connected to the rotation period of the star. To test the significance of the radial velocity changes of each target, we calculate

several relevant statistics.

First, to evaluate the overall radial velocity scatter of each target, we compute the χ^2 statistic of the radial velocity measurements with the null hypothesis of constant velocity using the relation

$$\chi_{\text{RV}}^2 = \sum_i \left(\frac{v_i - \langle v \rangle}{\sigma_i} \right)^2 \quad (4)$$

where v_i and σ_i are the radial velocities and measurement uncertainties of the target at epochs t_i , respectively, and $\langle v \rangle$ is the weighted mean of the radial velocity of the target. We would like to achieve a confidence level of $> 95\%$ that no single star is mistakenly identified as an SB1 in our sample. Given that we have ~ 200 targets, this condition requires a confidence level of $> 99.97\%$ for correct identification of individual targets. For a typical target observed at four epochs, this implies that we require $\chi_{\text{RV}}^2 > 19.1$ to identify a target as an SB1.

Second, to estimate systematic noise for each target, we consider the measurements for each observing run separately. Since each observing run is only a few days long, velocity changes of a few km s^{-1} on this timescale are much more likely to be due to rotation than to orbits. Specifically, for each target, we calculate the systematic noise during each observing run,

$$\sigma_{\text{N},j} = \sqrt{\sigma_{\text{S},j}^2 - \sigma_{\text{E},j}^2} \quad (5)$$

where $\sigma_{\text{S},j}$ is the weighted standard deviation of the radial velocities for observing run j , and $\sigma_{\text{E},j}$ is the weighted mean of the radial velocity errors for observing run j . The weighted standard deviation is given by

$$\sigma_{\text{S},j}^2 = \left(\frac{N'_j}{N'_j - 1} \right) \frac{\sum_k w_k (v_k - \langle v \rangle_j)^2}{\sum_k w_k} \quad (6)$$

where v_k are the velocities at epochs t_k from observing run j , $\langle v \rangle_j$ is the corresponding weighted mean of the velocities, $w_k \equiv 1/\sigma_k^2$ are the statistical weights based on measurement uncertainties at epochs t_k , and N'_j is the normalized number of frames defined as

$$N'_j \equiv N_j \frac{\langle w \rangle_j^2}{\langle w^2 \rangle_j} \quad (7)$$

where N_j is the number of frames taken of the given target during observing run j . Note, in the case of all equal weights, Eq. 6 reduces to the equation for simple standard deviation. Finally, we adopt as the systematic noise for a given target the weighted mean of the systematic noise for all the observing runs of the target, i.e., $\sigma_{\text{N}} \equiv \sqrt{\langle \sigma_{\text{N},j}^2 \rangle}$.

Third, to re-evaluate the radial velocity scatter of each target with compensation for systematic noise, we add in quadrature the systematic noise σ_{N} of a given target to the radial velocity uncertainties σ_i of the target, and re-evaluate the χ^2 statistic (Eq. 4) using the radial velocities and uncertainties aggregated by observing run, i.e., using v_j and σ_j the weighted means and standard errors of the targets during observing runs j . Analogous to the

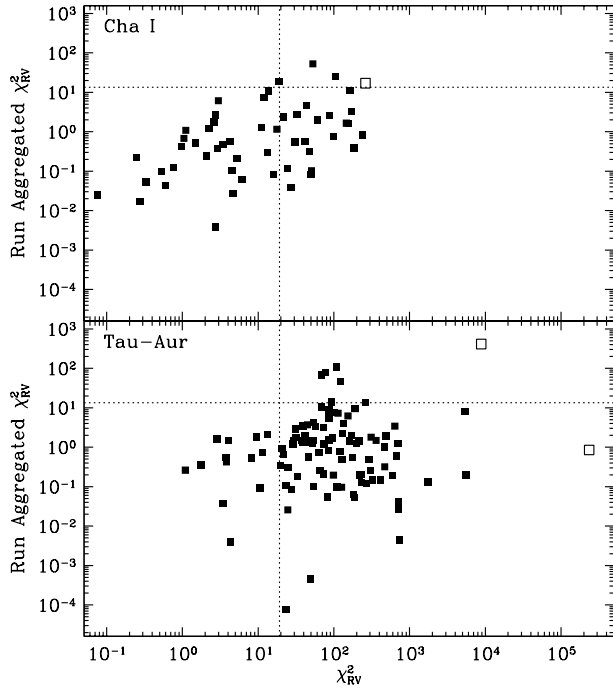


FIG. 3.— Run aggregated χ^2_{RV} for members of Cha I and Tau-Aur with single-peak broadening functions as a function of χ^2_{RV} . Single stars and SB1 candidates are denoted by solid and hollow symbols, respectively. The vertical and horizontal dotted-lines are drawn at $\chi^2_{RV} = 19.1$ and 13.4 , respectively, and represent the typical lower bound criteria of χ^2_{RV} to identify a target as an SB1 in our survey. The single stars in the upper right quadrant have radial velocity variations likely due to star spots. The exceptional SB1 in Tau-Aur, RX J0415.8+3100, has a run aggregated χ^2_{RV} that is well below the threshold of 13.4 because of the large daily RV variations from its short period companion.

assessment for overall radial velocity scatter, for a typical target observed during two observing runs, we look for a run aggregated $\chi^2_{RV} > 13.4$ to identify a target as an SB1. An exception to this guideline applies to SB1s with periods shorter than a few days because their radial velocity oscillations are on the same timescales as the observing runs themselves. To illustrate our χ^2_{RV} criteria visually, we plot in Fig. 3 the run aggregated χ^2_{RV} for our targets as a function of χ^2_{RV} . Note, the single stars in the upper right quadrant of Fig. 3 have radial velocity variations likely due to star spots.

Fourth, we estimate the extent of the radial velocity fluctuations induced by star spots (see also §5.3). Since the influence of star spots on observed radial velocity is related to the rotational velocity of the star, we show in Fig. 4 the radial velocity scatter within the observing runs for targets with single-peak broadening functions in our sample as a function of projected rotational velocity $v \sin i$. For both Cha I and Tau-Aur, the upper bound of the short-period velocity scatter is $\sim 15\%$ of $v \sin i$. Single-line targets with radial velocity scatter larger than this value are likely SB1s.

We identified three SB1s and four suspected SB1s in Cha I and Tau-Aur. The sets of radial velocity measurements for these objects are listed in Table 6.

4.3. Detection Limits

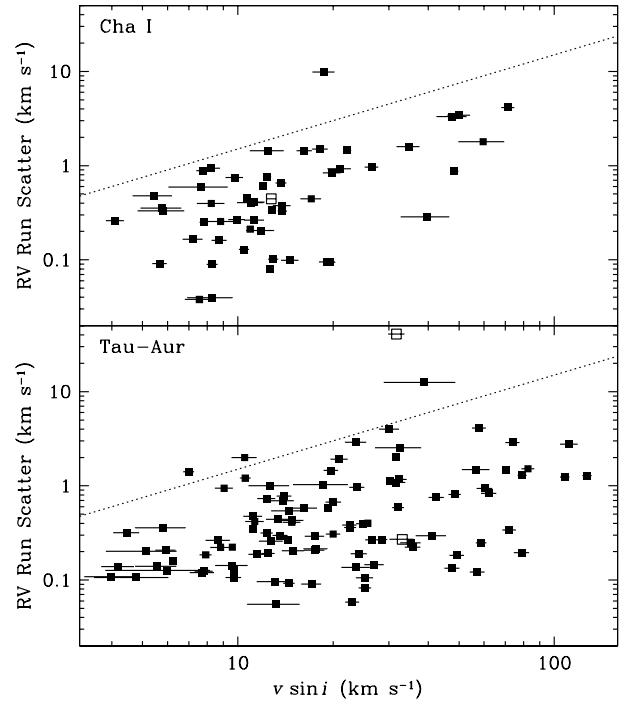


FIG. 4.— Radial velocity scatter within the observing runs for members of Cha I and Tau-Aur with single-peak broadening functions as a function of projected rotational velocity $v \sin i$. Single stars and SB1 candidates are denoted by solid and hollow symbols, respectively. The dotted-line is drawn at 15% of $v \sin i$ and represents the approximate upper bound of the radial velocity scatter. The single stars above this limit have large measurement uncertainties due to poor spectra, and the SB1s below the limit still show individual epoch radial velocity variability that exceeds the threshold.

Both companion mass M_2 and orbital period P contribute to the companion detection limits of radial velocity searches. Furthermore, for each mass and period combination, detection is also affected by orbital elements such as inclination angle i and orbital phase ϕ . Although eccentricity might facilitate or hinder the detection of a companion in an individual case, the effect is canceled out statistically (Fischer & Marcy 1992).

To derive the probability of detection for a given point in the (M_2, P) parameter space, we simulate binaries in circular orbits with systematic combinations of i selected incrementally from a $\cos i$ distribution, and ϕ selected incrementally from a uniform distribution spanning their full ranges. For each combination of orbital elements, we generate 1000 sinusoidal radial velocity curves, and add random errors drawn from a normal distribution centered on zero and with a chosen rms value $\sigma_{\text{noise}} = 0.34 \text{ km s}^{-1}$ which is equal to the typical intrinsic noise in our actual stars. Furthermore, like our typical observations of actual stars, we sample each simulated radial velocity curve four times (e.g., at epochs $t = 0, 0.2, 2$ and 30 days), and we adopt as measurement uncertainty the approximate median value of 0.10 km s^{-1} from our actual data. The χ^2 and minimum velocity scatter conditions described in §4.2 are used as detection criteria for the simulations. For a given (M_2, P) pair, we define the detection probability as the fraction of successful detections over the number of trials for that point. The result of these simulations in the (M_2, P) plane for a typical T Tauri star

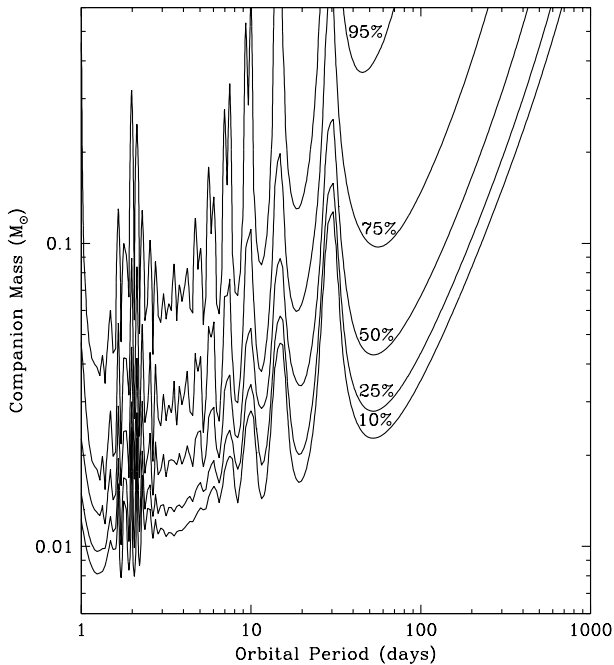


FIG. 5.— Detection probabilities for a given companion mass and orbital period for typical T Tauri stars in our sample ($0.6 M_{\odot}$; $v \sin i = 15 \text{ km s}^{-1}$) observed four times at epochs $t = 0, 0.2, 2$ and 30 days and assuming a measurement uncertainty of 0.1 km s^{-1} . At each point in the (M_2, P) space, the inclination angle i and the orbital phase ϕ were incremented over their full range. For each combination of orbital elements, 1000 radial velocity curves were generated, and Gaussian noise with an rms value of 0.34 km s^{-1} was added to each curve in Monte Carlo fashion to represent the typical intrinsic noise in our actual sample. The detection criteria used are the χ^2 and minimum velocity scatter conditions described in §4.2.

in our sample ($0.6 M_{\odot}$; $v \sin i = 15 \text{ km s}^{-1}$) is shown in Fig. 5 as iso-probability curves of detection. We see for example that we have a 75% probability of detecting a companion of mass $0.1 M_{\odot}$ with a period of 60 days if the typical $0.6 M_{\odot}$ primary star has been observed four times with our 30 day baseline. From Fig. 5, we also deduce that detection biases vary significantly for orbital periods $\lesssim 50$ days. This is due to aliasing from the sampling times.

The selection criteria for our study contain biases which affect a determination of the multiplicity rate. Specifically, a magnitude-limited sample favors the inclusion of SB2s (Branch 1976). This is especially the case for young stars where the dependence of luminosity on mass is comparatively gradual, i.e., $L \propto M^{\alpha}$, with $\alpha \sim 2$ for pre-main sequence stars rather than $\alpha \sim 4$ for stars on the main sequence.

5. RESULTS AND DISCUSSION

In our entire sample of 212 members of Cha I and Tau-Aur, we have identified a total of 12 systems that show acceleration due to close companions (three SB1s, five SB2s and four SB3s) and 7 systems for which we suspect this is the case. We will discuss these systems individually in §6. To reduce sampling bias in our close companion statistics, we trim our sample to include only targets that have observations spanning multiple observing runs (> 25 days). This ensures that all targets included for statistics have observations with time base-

lines sufficiently long to capture the radial velocity scatter from most SB1s. With this condition, there are 11 systems with close companions and 6 systems with suspected close companions from a final statistical sample of 174 systems. Of the 11 systems with close companions, three are SB1s, five are SB2s, and three are SB3s.

Below, we will first look for differences between our two regions, with primary mass and accretion, and with stars in the field. Second, we will look at possible non-companion contributions to radial velocity variations. Third, we will discuss 13 somewhat puzzling stars that have mean velocities that deviate from the velocity of the cluster, yet appear to be members from all other indicators.

5.1. Comparison of Binary Populations

We first compare the multiplicity fraction (MF) in Cha I and in Tau-Aur with each other. The Chamaeleon I and Taurus-Auriga star-forming regions are both T associations of similar age. Previous surveys using speckle and direct imaging show a similar multiplicity fraction for both regions (Lafrenière et al. 2008). The multiplicity fractions $\text{MF} = (\text{SB1} + \text{SB2} + \dots) / (\text{Singles} + \text{SB1} + \text{SB2} + \dots)$ we find, using high-resolution spectroscopy, in our sample are $0.07^{+0.05}_{-0.03}$ (4/61) for Cha I, and $0.06^{+0.03}_{-0.02}$ (7/113) for Tau-Aur.

Initially, to compare the multiplicity fractions, we used the binomial distribution comparison method described in Brandeker et al. (2006). However, that method could not reject the hypothesis that the close multiplicity probabilities of Cha I and Tau-Aur are equal, with any significance. Therefore, we instead compare the multiplicity fractions formally from first principles as follows. For random variables Q and R , the likelihood P that Q is greater than R is given by the formula

$$P[Q > R] = \int_{-\infty}^{+\infty} \left(f_Q(x) \int_{-\infty}^x f_R(y) dy \right) dx \quad (8)$$

where f_Q and f_R are the probability distribution functions of Q and R , respectively. In our case, the random variables are the underlying multiplicity fractions of stellar populations. By sampling a population, we will find k binaries out of n targets with the outcome governed by the binomial distribution $B(n, p)$ where p is the true multiplicity fraction of the population. Consequently, the probability distribution function of p given k observed binaries out of n targets is

$$f(p|k, n) = (n+1) \binom{n}{k} p^k (1-p)^{n-k} \quad (9)$$

Applying this function to Eq. 8, we get the likelihood that the multiplicity fraction of population Q is greater than that of population R is

$$P[p_Q > p_R] = \int_0^1 \left(f(p_Q|k_Q, n_Q) \int_0^{p_Q} f(p_R|k_R, n_R) dp_R \right) dp_Q \quad (10)$$

By substituting the MF results from Cha I and Tau-Aur into this formula, we find the likelihood that the MF of Cha I is greater than that of Tau-Aur is only 58%.

Therefore, the two regions have similar MF values. Subsequently, we will use the combined results when making comparisons with those of other populations, and between various sub-populations in our sample determined by physical characteristics.

To investigate the change in close multiplicity as a function of primary mass, we divide our sample into two bins of nearly equal number and calculate the MF in each bin. We find multiplicity fractions of $0.06^{+0.03}_{-0.02}$ (6/98) for F–K spectral type targets, and $0.07^{+0.04}_{-0.03}$ (5/76) for M spectral type targets. There is no clear dependence in the spectroscopic regime of multiplicity fraction on primary mass: the likelihood that the multiplicity fraction of the F–K type stars is greater than that of M-type stars is only 44%. This is in stark contrast to the results of imaging surveys (e.g., Lafrenière et al. 2008) which show, for Chamaeleon I, Taurus, Upper Scorpius A and field stars, a marked increase in wide companions with increasing primary mass.

To address the question of whether close companions are responsible for the observed difference between classical and weak-lined T Tauri stars from §1, we measure the full width of H α at 10% of the peak (hereafter, H α 10% width) of our targets to differentiate accretors and non-accretors. As suggested by previous spectroscopic studies (e.g., Jayawardhana et al. 2003), we classify accretors or CTTSs as stars with H α 10% widths larger than 200 km s^{-1} after subtracting rotational broadening. We measured H α 10% widths previously for a subsample of our targets (Nguyen et al. 2009a), and apply the same technique here. Five targets in our statistical sample did not have reliable measurements for H α 10% width. Of the remaining 169 targets, we find a close binary fraction of $0.08^{+0.04}_{-0.03}$ (8/104) and $0.05^{+0.04}_{-0.02}$ (3/65) for non-accretors and accretors, respectively. The populations of WTTS and CTTS have statistically similar close binary fractions: the likelihood from our data that the true multiplicity fraction of WTTSs is greater than that of CTTSs is 75% which is approximately 1σ . Therefore, we cannot say confidently that close companions are the main source of the attenuated accretion in weak-lined T Tauri stars.

Finally, we compare our multiplicity fractions with values for field stars from the G dwarf survey of Duquennoy & Mayor (1991), the M dwarf surveys of Fischer & Marcy (1992), and the nearby solar-type (\sim F6–K3) dwarf survey of Raghavan et al. (2010). Comparison between our sample and those of the field population is not straightforward because the surveys have different time baselines and companion mass sensitivities. Specifically, we observed each of our stars typically at four epochs with baselines of up to several months whereas the aforementioned field dwarf surveys generally had more than a dozen observations per star spanning a four year interval. Furthermore, the field dwarf surveys are sensitive to companions having masses less than the primary mass, extending to the hydrogen burning limit, $0.08 M_{\odot}$ whereas our survey should detect $\sim 50\%$ of sub-stellar companions with masses of $0.05 M_{\odot}$ for orbital periods $\lesssim 100$ days.

A meaningful comparison of multiplicity fractions requires that we correct for the differences in the detection completeness of the surveys. To accomplish this, we re-

strict our statistical comparison to common orbital periods and companion mass ranges. Since our stars are typically observed four times, to determine the likely range of companion masses and orbital periods for our survey we make use of probability theory.

Let $\mathcal{M}(m, p)$ be the a priori distribution of multiplicity rates for our star population in the companion mass and orbital period (M_2, P) space. In the same space, let $\mathcal{D}(m, p)$ be the detection success rates of our observing scheme, i.e., the results of our simulations in §4.3. Using Bayes’ theorem (Bayes et al. 1763), from the prior distribution $\mathcal{M}(m, p)$, and the likelihood function $\mathcal{D}(m, p)$, we calculate the probability \mathcal{P} that a detected companion is in the given intervals $[M_{2,\min}, M_{2,\max}]$ and $[P_{\min}, P_{\max}]$,

$$\mathcal{P} = \frac{\sum_{m=M_{2,\min}}^{M_{2,\max}} \sum_{p=P_{\min}}^{P_{\max}} \mathcal{M}(m, p) \mathcal{D}(m, p)}{\sum_m \sum_p \mathcal{M}(m, p) \mathcal{D}(m, p)} \quad (11)$$

Since we have no prior knowledge about the multiplicity rates, we use the most ignorant prior distribution $\mathcal{M}(m, p) = 1$, and assume companions can have masses up to that of the primary star. Furthermore, we do not expect orbital periods of our binary systems to be much less than a day (see Appendix A). From our simulation results, we estimate that 95% of our detected companions have stellar masses with orbital periods up to ~ 200 days. In this range, the mean detection probability is 0.87. Therefore, we estimate a corrected MF of $(11/174) \times 0.95 \div 0.87 = 0.07^{+0.03}_{-0.02}$ in the companion mass and orbital period intervals $[0.08 M_{\odot}, 0.6 M_{\odot}]$ and $[1 \text{ d}, 200 \text{ d}]$, respectively. In the same range, counting the companion detections of Duquennoy & Mayor (1991) and Fischer & Marcy (1992), we find an MF of $0.09^{+0.03}_{-0.02}$ and $0.03^{+0.04}_{-0.02}$ for field G and M dwarfs, respectively. Furthermore, for the nearby solar-type dwarfs of Raghavan et al. (2010), we find an MF of $0.073^{+0.014}_{-0.012}$. Thus, we do not find a significant difference with the field. The results are illustrated graphically in Fig. 6.

5.2. Mass Dependence

The observed fraction of T Tauri stars with spectroscopic companions in our sample does not depend on stellar mass. This result contrasts those of imaging multiplicity surveys (e.g., Kraus & Hillenbrand 2007; Lafrenière et al. 2008) where there is an observed trend of increasing wide binary fraction with increasing primary mass. One possibility is that primary mass is important for binaries with wide separations because of dynamical interactions within the cluster. Dynamical interactions can only eject companions if there is sufficient kinetic energy. Moreover, the kinetic energy of a passing star must be greater than the gravitational binding energy of the binary for break up to occur. Binding energy is proportional to primary mass, so higher mass stars are more likely than their lower mass counterparts to hold onto their companions. However, companions in tight orbits are so strongly bound to their primary star that disruption from dynamical interaction is unlikely regardless of the primary mass.

Primary mass becomes important at binary separations where the total energy of the binary system is comparable to the kinetic energy of a passing star. By

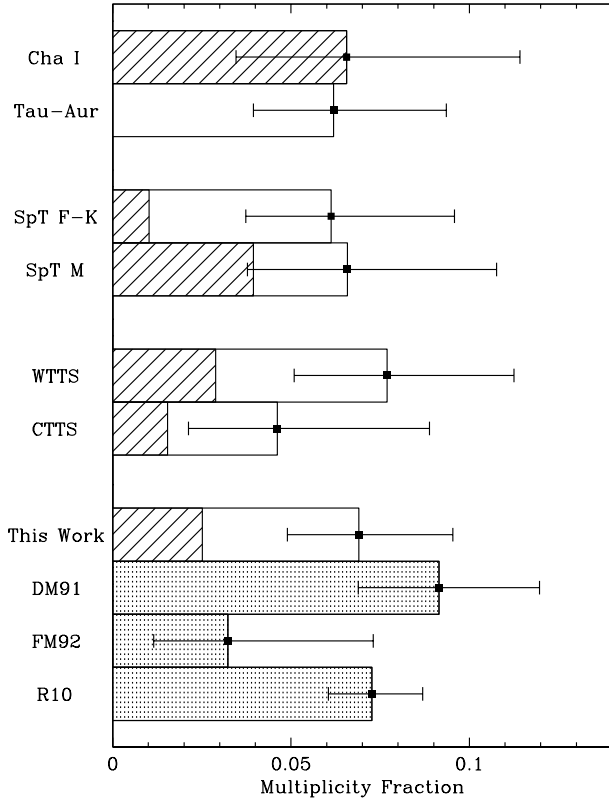


FIG. 6.— Comparisons of the multiplicity fractions of various sub-populations in Cha I and Tau-Aur, and between this work and those of Duquennoy & Mayor (1991) (DM91), Fischer & Marcy (1992) (FM92), and Raghavan et al. (2010) (R10). The contribution from the Cha I sample is denoted by striped areas. The unshaded areas represent the contribution from the Tau-Aur sample. The results from the field dwarf surveys of DM91, FM92 and R10 are stippled, and count only companions with stellar masses and orbital periods between 1 and 200 days which is comparable to the detection coverage of this work. For the comparison with the field dwarf surveys, the multiplicity fraction for this work has been corrected for detection sensitivity.

equating the energies, we get the following relation for this transitional binary separation distance r_*

$$r_* = \frac{M_1}{M_3} \frac{GM_2}{v^2} \quad (12)$$

where M_1 , M_2 and M_3 are the masses of the primary, secondary and passing star, and v is the relative velocity of the encounter. We can estimate the typical encounter velocity from the velocity dispersion of the clusters. From our single stars, we estimate that the radial velocity dispersions σ_{RV} of Chamaeleon I and Taurus-Auriga are 1.7 km s^{-1} and 3.6 km s^{-1} , respectively. If we assume three-dimensional symmetry, then the average velocity between stars is $(4/\sqrt{\pi}) \sigma_{RV}$ which amounts to $\sim 3.8 \text{ km s}^{-1}$ and $\sim 8.1 \text{ km s}^{-1}$ for Cha I and Tau-Aur, respectively. Applying these values to Eq. 12 and assuming $M_1/M_3 \sim 1$, we find primary mass becomes important to ejection at binary separations of $\sim 63 (M_2/M_\odot)$ AU in Chamaeleon I, and $\sim 14 (M_2/M_\odot)$ AU in Taurus-Auriga. These separations are in the regime of imaging surveys.

Although scattering events are possible for binaries with separations of tens of AU in Cha I and Tau-Aur, the likelihood of an encounter depends on the stellar

densities of the star-forming regions. Moreover, the interaction timescale τ is roughly equal to $(\sigma n v)^{-1}$ where σ is the encounter cross-sectional area (πr_*^2), n is the stellar density, and v is the average relative velocity between stars. For a typical wide binary in Cha I and Tau-Aur, at current densities of $\lesssim 100 \text{ pc}^{-3}$ (Oasa et al. 1999; Joergens 2006), the interaction timescale is of order a few Gyr or longer. The interaction timescale only becomes comparable to the current cluster age for binaries with separations of $\gtrsim 10^4$ AU. Visual binaries with separations much less than this show a mass dependence. Therefore, if dynamical interaction is a major source of the mass dependence of wide binaries, then those stars must have emerged from subgroups with stellar densities several orders of magnitude higher than their current sparse environment.

There is observational evidence that stellar density may not solely influence the frequency of wide binaries. The wide binary frequency in the periphery of the ONC is similar to that in the core, where stellar densities are two orders of magnitude higher (Köhler et al. 2006). While this trend is not observed by Reipurth et al. (2007), both wide binary frequencies in the ONC are observed to be several times lower than those of Chamaeleon I and Taurus-Auriga. If the initial binary fractions in these regions were similar, we would expect a much higher number of binaries in the ONC periphery than observed. Aside from the dense subgroup scenario mentioned above, one possible explanation is that the initial binary frequency differs significantly between star-forming regions. This suggests that the binary formation rate is influenced by environmental conditions.

5.3. Radial Velocity Scatter

One obvious source of stellar radial velocity fluctuations over time is a close companion. However, close companions are not the only plausible explanation for oscillatory radial velocity behaviour. Periodic variations in radial velocity, especially in young stars using measurements at optical wavelengths, can be caused by star spots (e.g., see Huerta et al. 2008; Huélamo et al. 2008). To gauge the maximum amplitude of this effect, let us consider a star spot on the equator of a star observed edge-on. For simplicity, we will model the star as a rigid unit sphere, and the star spot as a black spherical cap. A spherical cap is the region of a sphere which is cut off by a plane. We will ignore limb darkening, and assume the face of the star is a uniformly illuminated stellar disk. From this model, with the stellar rotation about the y-axis, and the line of sight to the observer along the z-axis, the observed net radial velocity shift caused by the star spot is

$$\Delta v = \frac{\iint_T v_0 x \, dy \, dx}{\iint_S dy \, dx - \iint_T dy \, dx} \quad (13)$$

where S is the region of the stellar disk (a unit circle), T is the region of the star spot projected onto the stellar disk, and v_0 is the linear rotational velocity of the star at the equator. Here, the numerator represents the radial velocity contribution integrated over the area of the star spot, and the denominator accounts for the observed surface area of the star, and effectively normalizes the radial

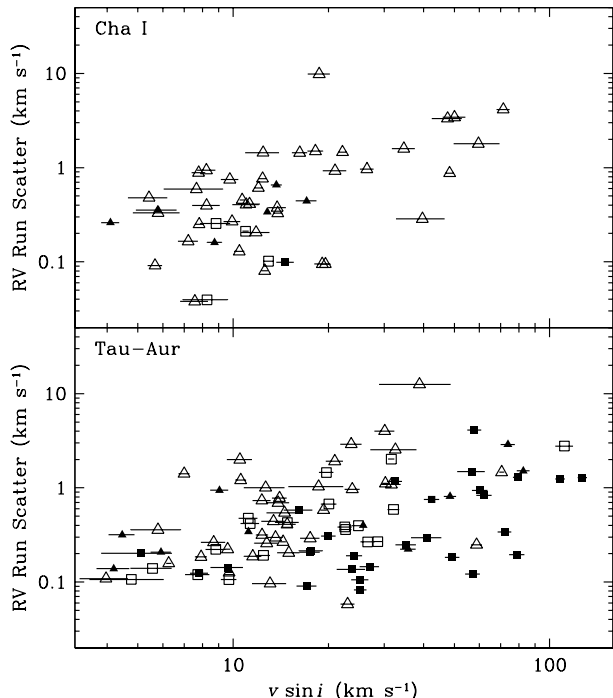


FIG. 7.— Radial velocity scatter within the observing runs for single non-accretors in Cha I and Tau-Aur as a function of projected rotational velocity $v \sin i$. The stars have been grouped by $H\alpha$ equivalent width. Hollow triangles represent stars with $H\alpha$ EW < -3 . Solid triangles indicate stars with $H\alpha$ EW in the range of $[-3, -1.5]$. Hollow squares represent stars with $H\alpha$ EW in the range of $[-1.5, 0]$. Solid squares indicate stars with $H\alpha$ EW ≥ 0 . There is an increase in radial velocity scatter with $v \sin i$. However, the groups by $H\alpha$ EW are not well separated from each other.

velocity result.

Evaluating Eq. 13 over all rotational phases, we find that a star spot covering 10% of the stellar surface can produce a theoretical maximum RV oscillation semi-amplitude of $\sim 0.20 v_0$. This amplitude is similar to the RV scatter upper bound of 15% $v \sin i$ observed in our sample. However, real star spots do not affect all spectral features equally nor do they have identical impact at all optical depths. A technique such as line bisector analysis, which probes radial velocity bias at different depths, is required to properly assess the contribution of star spots on variations in radial velocity.

The net effect of star spots on radial velocity measurements relies on the asymmetry that the spots produce on the stellar surface. In terms of contribution to radial velocity bias, multiple star spots can partially negate one another at different rotational phases. Therefore, since the total number of star spots, not their effective asymmetry, is connected to stellar activity, we do not necessarily expect a correlation between activity and radial velocity scatter. In Fig. 7, we show the radial velocity scatter over time for single non-accretors grouped by $H\alpha$ equivalent width, an activity indicator, in our sample and as a function of $v \sin i$. As expected, the upper bound of RV scatter increases with $v \sin i$. More importantly, there is no clear separation of stars by $H\alpha$ equivalent width. Thus, while spot-induced RV variability obviously requires some activity, it is perhaps not surprising that the level of activity does not correlate well with the amount of variability.

5.4. Radial Velocity Outliers

The targets in our original sample were identified as either members of Cha I by Luhman (2004a), or members of Tau-Aur by Leinert et al. (1993), Ghez et al. (1993), Simon et al. (1995), Kohler & Leinert (1998), Briceño et al. (2002) and Luhman (2004b) based on a combination of one or more indicators such as Li- $\lambda 6708$ absorption, reddening, emission lines, and IR excess emission. However, we find among the 151 single stars in our statistical sample that five stars in Cha I, and eight stars in Tau-Aur have overall radial velocities that deviate substantially from the velocities of their associated clusters, i.e., the weighted mean velocities of these targets are Tukey outliers with respect to the rest of the sample. Moreover, for identifying these outliers, we adopted the median cluster radial velocity of 15.3 km s^{-1} , and limits of 12.9 and 17.2 km s^{-1} for Cha I. For Tau-Aur, we used a median radial velocity of 16.2 km s^{-1} , and limits of 10.3 and 22.3 km s^{-1} . Stars with radial velocities that exceed the outlined ranges are indicated in Table 2. We examine several possible sources for these abnormal mean radial velocities.

First, to see if localized phenomena in the star-forming regions are responsible for the radial velocity anomalies, we examine the positions of the radial velocity outliers on the sky. The projected spatial distributions of Cha I and Tau-Aur are shown in Fig. 8. From the plots, we see no pattern in the spatial distribution of the radial velocity outliers, i.e., the radial velocity deviations are not confined to a particular area within the star-forming regions. Hence, it is unlikely that the radial velocity outliers in Cha I and Tau-Aur are the result of peculiarities in specific parts of the clusters.

Next, we examine the possibility that the targets with unusual mean radial velocity are the result of ejection from past multiple systems. If this is the case, we would expect the radial velocity outliers to have masses generally lower than the rest of the sample. The weighted mean radial velocity as a function of stellar mass derived from the models of D’Antona & Mazzitelli (1997) for our $\sim 2 \text{ Myr}$ old sample is shown in Fig. 9. We see from the plots that the targets with outlying radial velocities have masses spanning the full range of the sample. In addition, we expect that ejected stars from previous multiple systems should show little or no accretion because we do not expect that ejected stars would carry away with them a substantial portion of the material surrounding the original system. However, we find that 3 out of the 13 radial velocity outliers are CTTSS. Therefore, from the accretion and mass distribution findings, we conclude that ejection is not likely the main source of radial velocity outliers in our sample.

Finally, we check if the anomalous radial velocities could be caused by unseen companions. The lower bound of flux ratio for our identified SB2 candidates was ~ 0.1 . Using the models of D’Antona & Mazzitelli (1997) and assuming a stellar age of 2 Myr , if our lowest mass RV outlier ($0.19 M_{\odot}$) had a companion of mass $\lesssim 0.08 M_{\odot}$, we would not detect it as an SB2. This is also the case if we use instead the models of Baraffe et al. (1998). Furthermore, our SB1 detection success rate for such a binary system from Monte Carlo simulations assuming a circular orbital period $> 1 \text{ yr}$ is less than 2%. For a one-

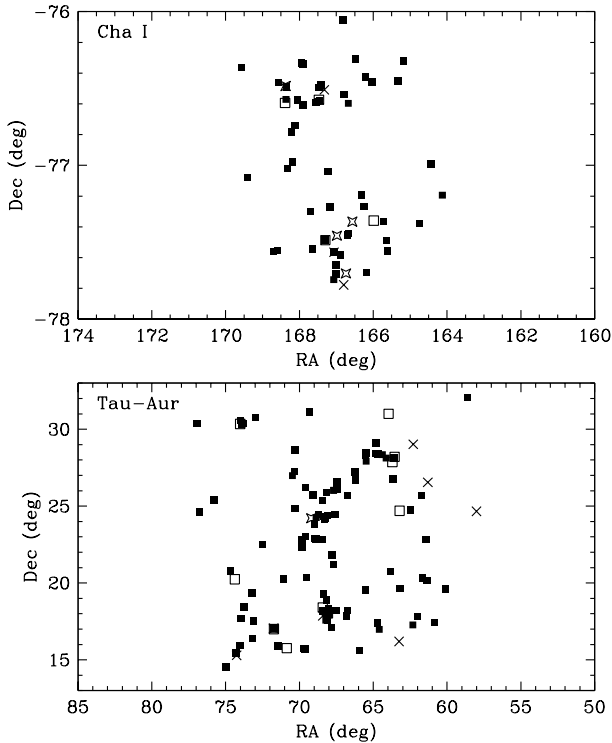


FIG. 8.— The spatial distribution of targets in our sample of Cha I and Tau-Aur. The solid symbols represent single stars that have mean radial velocities consistent with their respective clusters. Objects with mean radial velocities that are outliers with respect to their clusters are denoted by cross symbols for those moving faster away from us, and starred symbols for those moving more toward us. Spectroscopic binaries are plotted as hollow symbols. The distribution of radial velocity outliers shows no particular pattern.

year period, the primary star would have an expected semi-amplitude of $\sim 5 \text{ km s}^{-1}$, which is consistent with the radial velocity differences we observe of the low mass outliers in our sample. Similarly, if our highest mass RV outlier ($2.8 M_{\odot}$) had a $2 M_{\odot}$ companion in a circular orbit with a period of > 1000 days, we would not likely identify it as a binary. For a 1000-day period, the primary star would have a semi-amplitude of up to $\sim 15 \text{ km s}^{-1}$ which is consistent with the radial velocity deviations we observe in the high mass outliers. The results for the rest of the radial velocity outliers are similar. Thus, some of the single stars with an overall radial velocity inconsistent with their cluster velocity may be long period SB1s, i.e., they would not affect our comparisons with, e.g., the field population.

6. NOTES ON INDIVIDUAL SOURCES

For each object in our survey, we provide brief comments and plots in Fig. 10 through 37. Each figure consists of four main sections as follows:

1. In the upper left, basic data and measurements are listed: these are the star-forming region, object name, coordinates, spectral type, estimated S/N at H α , H α 10% width, $v \sin i$, Ca II- $\lambda 8662$ equivalent width, and *Spitzer Space Telescope* [3.6] - [8.0] IRAC color magnitude (Fazio et al. 2004).
2. In the upper right, radial velocity curves are plotted. The error bars are the weighted standard devi-

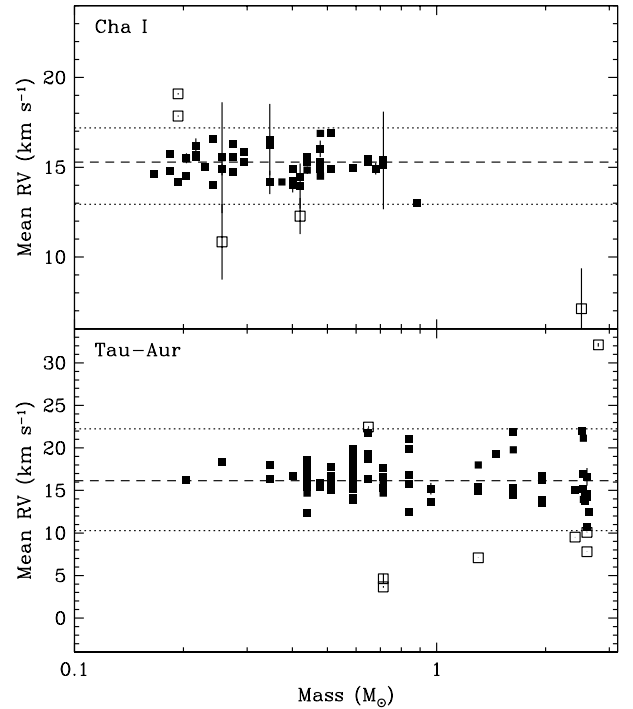


FIG. 9.— Mean radial velocity as a function of stellar mass derived from the models of D’Antona & Mazzitelli (1997) for our sample from Cha I and Tau-Aur ($\sim 2 \text{ Myr}$ old). The solid symbols represent single stars that have mean radial velocities consistent with their respective clusters. Objects with mean radial velocities that are outliers with respect to their clusters are denoted by hollow symbols. The dashed-lines show the median radial velocity of the single stars. The Tukey outlier threshold is delineated by the dotted-lines. There appears to be no mass preference for radial velocity outliers.

ation of the radial velocity estimates over all echelle orders for a given epoch. The dotted-line is the weighted mean of the radial velocities. For SB2s and SB3s, the radial velocities of the secondary and tertiary objects are plotted as hollow squares and diagonal crosses, respectively.

3. In the lower panels, there are five columns of plots with each row representing a different observed epoch: from left to right, these are the broadening function (see §3.1), H α , Li- $\lambda 6708$, Ca II- $\lambda 8662$, and Mg I- $\lambda 8807$. The dotted-line in the broadening function shows the observer’s rest frame velocity, and is used primarily to check for moonlight and twilight sky contamination. The H α and Ca II- $\lambda 8662$ plots are provided to gauge activity. Stellar youth is indicated by Li- $\lambda 6708$ absorption. The Mg I- $\lambda 8807$ line is shown because it should be present in stars spanning the spectral type range of our sample, and shows graphically the overall quality of the data for that epoch.
4. In the caption, we outline our reasons for classifying the object as with or without spectroscopic companions, and provide a short discussion on the object. This discussion makes note of, but is not limited to, possible contaminations from moonlight, twilight sky, or nearby visual companions, and support for cluster membership for radial velocity outliers and objects without clear Li- $\lambda 6708$ absorption.

Among our complete sample, we found three SB1s, five (short-period) SB2s, and four SB3s. We will discuss individual sources grouped in reverse order below.

6.1. SB3: Triple-lined Spectroscopic Binaries

T55 (Ass Cha T 2-55, CHXR 61)— (Fig. 10) This is a previously unknown SB3 consisting of two rapidly accelerating sources and a stable brighter component. This system had not previously been studied spectroscopically, and no resolved companions were found by Lafrenière et al. (2008).

For the close orbit, from the four reliable sets of velocity measurements and assuming a circular orbit, we infer a mass ratio of $q \sim 0.8$ and a center-of-mass velocity of $\gamma \sim 12 \text{ km s}^{-1}$. The maximum observed velocity separation is $\Delta v \simeq 150 \text{ km s}^{-1}$, and the rapid change between the third and fourth epoch suggests a short period, of at most a few days. We do not have sufficient measurements to determine the period uniquely, but we can derive some constraints. Assuming a total radial velocity amplitude $v_{\text{tot}} \simeq \Delta v$, one can estimate the total mass as $M \sin^3 i \simeq v_{\text{tot}}^3 P / 2\pi G \simeq 0.3(P/1 \text{ d}) M_{\odot}$ and the projected semi-major axis as $a \sin i = v_{\text{tot}} P / 2\pi = 3(P/1 \text{ d}) R_{\odot}$. We also have the following constraints. First, given the M4.5 spectral type, the expected mass of the brighter, stationary component, is $M_A \sim 0.2 M_{\odot}$. The other stars should be less massive, so the period cannot be much longer than one day. Second, the radius of the brighter star should be around $1 R_{\odot}$ and, given the flux ratios of 0.4 and 0.2, components B and C should have radii around 0.6 and $0.5 R_{\odot}$, respectively. For these components to fit in the orbit, the period can also not be much shorter than 1 day. Independent of the precise period, the orbit is sufficiently close-in such that it should be circularized, and the rotation of the stars synchronized. From the observed rotational broadenings of 34 and 31 km s^{-1} , one infers rotation periods of $P \sin i = 2\pi R \sin i / v \sin i \simeq 0.8 \text{ d}$. From all evidence, we thus conclude that the orbital period is $P \sim 0.8 \text{ d}$. Given the mass ratio of $q \sim 0.8$, the individual masses are $M_{B,C} \sin^3 i \simeq (0.14, 0.12) M_{\odot}$.

For the outer orbit, from the fact that we do not see variations larger than a few km s^{-1} on our ~ 300 day baseline, we can only limit the period to be longer than $\gtrsim 2 \text{ yr}$. A long period is also suggested by the velocity separation of $\lesssim 5 \text{ km s}^{-1}$ between the close binary center-of-mass and component A.

RX J0412.8+2442 (V1198 Tau)— (Fig. 11) This is a previously unknown SB3 consisting of two rapidly accelerating sources (with a maximum velocity difference of at least 115 km s^{-1}), and a stable fainter component, which is likely a less massive star in a wide orbit. The B and C components have a flux ratio of 0.88 ± 0.12 and 0.36 ± 0.04 to the A component, respectively. Based on the spectral type of G9 for the primary and the flux ratios, we find that the secondary is likely of G9/K0 type, and the tertiary a K1. Given the high theoretical mass of the inner binary ($2.23 M_{\odot} + 2.16 M_{\odot}$), its maximum separation is $\max(a_{\text{tot}}) = 0.3 \text{ AU}$. On the other hand, the tertiary shows a velocity difference to the A–B center-of-mass that is smaller than 3 km s^{-1} , implying a maximum possible separation of 600 AU between the C component and the A–B mass center. Kohler & Leinert (1998) observed this system with high spatial resolution

using speckle interferometry, but found no spatially resolved companions with a limiting contrast ratio of 0.13 at $0''.13$ (corresponding to the projected distance of 18 AU at 140 pc). The flux ratio between A+B and C is estimated to be 0.19 in R and 0.23 in K ; thus, it should be detected easily outside $0''.13$ by Kohler & Leinert (1998). The possibilities remain that we are seeing the tertiary in a strongly inclined orbit, in a special position in its orbit, or both. Note, the systemic radial velocity of this SB3 is $\sim 30 \text{ km s}^{-1}$, which deviates from the cluster radial velocity of $\sim 16 \text{ km s}^{-1}$, and makes this an RV outlier.

V773 Tau (HD 283447, HIP 19762, HBC 367)— (Fig. 12) This is an SB3 and previously known quadruple system (Duchêne et al. 2003; Woitas 2003). The fourth component is an infrared companion, which explains its absence from our spectra. Of the other three, two are in a tight 51-day (2.8 mas , 0.38 AU) orbit (Boden et al. 2007), and the third in a 46-yr orbit around A–B (Duchêne et al. 2003). The radial velocities of the A and B components computed by (Boden et al. 2007) do not match well with the radial velocities we estimate from decomposing the derived broadening functions of the system. This is because the broadening functions have broad and blended peaks, which are difficult to decompose reliably to estimate radial velocities.

LkCa 3 A (HBC 368, V1098 Tau)— (Fig. 13) This is an SB3 consisting of three sources, all of which show acceleration over our one month baseline. The source is listed as an SB1 in the review of Mathieu (1994), with period $P = 12.941 \text{ d}$, eccentricity $e = 0.2$, projected semi-major axis of relative orbit $a \sin i = 0.032 \text{ AU}$, and center-of-mass velocity $\gamma = 14.9 \text{ km s}^{-1}$. However, it is not clear how reliable the numbers are given the additional components we see. It was found to have a resolved companion with a separation of $0''.47$ – $0''.491$, LkCa 3 B, by Leinert et al. (1993) and Ghez et al. (1993). We see no direct evidence for this component in our broadening function, even though it should contribute given the flux ratio, and in epoch 2 none of the other components overlap with its expected velocity (roughly the cluster velocity). Perhaps, it is fainter in R than estimated, it rotates relatively rapidly, or the resolved companion could itself be a close spectroscopic binary which would not necessarily match the system velocity. Nevertheless, we should caution that especially the velocity of the slowest and brightest component, LkCa 3 Aa, may be somewhat biased.

6.2. SB2: Double-lined Spectroscopic Binaries

CHXR 12— (Fig. 14) This is a previously unknown SB2 with no spatially detected companions (Lafrenière et al. 2008). The measured spectral type is M3.5 for the primary, and the flux ratio 0.2 ± 0.08 implies M6 for the secondary, assuming an age of 2 Myr . This corresponds to a system mass of $0.2 M_{\odot} + 0.14 M_{\odot} = 0.34 M_{\odot}$. This total mass is close to that calculated using the estimated mass ratio of ~ 0.43 derived from the method outlined in Wilson (1941). Given the maximum observed velocity separation is $\Delta v \sim 33 \text{ km s}^{-1}$, we find the widest possible spatial separation to be 0.3 AU , well within the 13 AU limit reported by Lafrenière et al. (2008).

T42 (Ass Cha T 2-42, FM Cha, HBC 579)— (Fig. 15) This is a previously unknown SB2 with no spatially detected companions (Lafrenière et al. 2008). The measured spectral type is K5 for the primary, and the flux ratio to the secondary is 0.8 ± 0.3 , corresponding to a system mass of $0.70 M_{\odot} + 0.65 M_{\odot} = 1.35 M_{\odot}$. This total mass is similar to the value calculated from the mass ratio of ~ 0.81 estimated using the method of Wilson (1941). Given the maximum observed velocity separation is $\Delta v \sim 40 \text{ km s}^{-1}$, we find the widest possible spatial separation to be 0.8 AU, undetectable by Lafrenière et al. (2008).

V826 Tau (HBC 400)— (Fig. 16) This is an SB2, and the first spectroscopic binary pre-main sequence (PMS) star to be confirmed (Mundt et al. 1983). Reipurth et al. (1990) refined the orbital elements and found a period of 3.9 days. Furthermore, the extrapolated radial velocities from the orbital elements are consistent to within a few km s^{-1} of our radial velocities estimates, which is well-matched given very short-period and the radial velocity semi-amplitudes of $\sim 18 \text{ km s}^{-1}$. By comparing $M \sin^3 i$ dynamical masses to masses from theoretical evolutionary tracks, they infer the inclination $i = 13^{\circ} \pm 1^{\circ}$. Because of the cubic dependence on inclination, this estimate is not sensitive to the determined mass, and using more modern models by D’Antona & Mazzitelli (1997) only changes the best fit inclination to $14^{\circ}.9$. Assuming that the rotations of the stars are tidally locked together with their measured $v \sin i = 4.2 \text{ km s}^{-1}$, they derive stellar radii of $1.44 R_{\odot}$. This is consistent with the $1.4 R_{\odot}$ expected from a 2 Myr old K7 star (D’Antona & Mazzitelli 1997), but inconsistent with our measurement of $v \sin i \sim 8.9 \text{ km s}^{-1}$, which would double the radii. However, the broadening function technique we used to measure $v \sin i$ of SB2 components has a lower limit of $\sim 9 \text{ km s}^{-1}$ for our spectra (see §3.2). Therefore, we cannot refute the previously published rotational velocities for this binary, and the stars could very well be in synchronous rotation with their orbit. Unfortunately, the close to pole-on inclination of the system makes it potentially difficult to measure periods from photometric modulation by star spots. We measure a flux ratio of 0.88 ± 0.06 which is in fair agreement with the mass ratio of 1.0 estimated using the method of Wilson (1941). Using high-resolution speckle interferometry, Leinert et al. (1993) did not find any additional companions.

DQ Tau (HBC 72)— (Fig. 17) This is a known SB2, first reported by Mathieu et al. (1997) to have a period of 15.8 days, and a circumbinary disk. The radial velocities extrapolated from the orbital elements given by Mathieu et al. (1997) are consistent to within a few km s^{-1} of our measured radial velocities, which is not a bad match given the estimated radial velocity semi-amplitudes of $\sim 20 \text{ km s}^{-1}$. No spatially resolved companions were found in a high-resolution search using speckle interferometry by Leinert et al. (1993), but Boden et al. (2009) resolved the spectroscopic binary to a 0.96 mas semi-major axis orbit, corresponding to 0.13 AU at the 140 pc distance to the system.

HBC 427 (V397 Aur)— (Fig. 18) This is an SB2 in our data with a flux ratio between the components of

0.157 ± 0.014 . The system was first noted as an SB1 by Walter et al. (1988), and subsequently monitored to find an orbital solution. An astrometric-spectroscopic orbital solution was derived by combining 58 RV measurements distributed over 14 yr (using the *Center for Astrophysics Digital Speedometers*) with 14 spatially resolved astrometric measurements spanning 3.3 yr (using the *Fine Guidance Sensor* on the *Hubble Space Telescope*) by Steffen et al. (2001). They determined for the binary system an orbital period of $6.913 \pm 0.033 \text{ yr}$, and dynamical masses of $1.45 \pm 0.19 M_{\odot}$ and $0.81 \pm 0.09 M_{\odot}$. Furthermore, they find a V-band flux ratio of 0.11, which translates to an R-band flux ratio of 0.17 assuming colors of an K5 and M2 atmosphere for the primary and secondary, consistent with our finding of 0.157 ± 0.014 . Given their orbital elements, our observing epochs range between orbital phase 0.951 and 0.963. This is close to the maximum RV separation of the components at the heliocentric RV 4 km s^{-1} and 35 km s^{-1} , respectively, which are close to our derived velocities of $4\text{--}6 \text{ km s}^{-1}$ and $32\text{--}35 \text{ km s}^{-1}$.

T31 A (VW Cha)— (Fig. 19) T31 A is a suspected SB2. The entire system T31 is a known hierarchical quadruple system with a wide companion (C) at $16''.8$ (Correia et al. 2006) and a tight $0''.1$ binary (Ba,Bb) located $0''.7$ from the primary A (Brandeker et al. 2001). A previously reported companion (D) at $2''.7$ (Ghez et al. 1997a) has not been confirmed (Brandeker et al. 2001; Correia et al. 2006). Our spectra of the primary show evidence for two components (Aa,Ab) separated by 20 km s^{-1} , with a tentative flux ratio of 0.7 ± 0.3 . The near-equal brightness of the components and good seeing conditions at the time of observations precludes the observed spectral components to be due to contamination by the known spatially resolved companions. Melo (2003) reports the presence of three components in the cross-correlation function, one which they attribute to contamination by component B. Guenther et al. (2007) speculate that their observed erratic RV variability, and the asymmetric shape of the cross-correlation function are due to B contributing a varying amount of light, depending on the precise placement of the $2''.0$ wide optical fiber. They do not rule out T31 A being SB2, however, and we think this a more likely explanation given the small flux contribution by B, which has a A–B $\Delta K \sim 1.74$ or an R-band flux ratio of ~ 0.03 .

For the primary A, we derive a spectral type of K3, which is slightly earlier than the K5/K7 found by Brandner & Zinnecker (1997), but later than K2 found by Appenzeller & Mundt (1989). For Ba+Bb, we find a spectral type of K7, same as Brandner & Zinnecker (1997), while we did not observe component D. With a radial velocity difference of 24 km s^{-1} , the widest possible separation would be 3 AU, which corresponds to observing the $2 M_{\odot}$ system edge-on. AO observations rule out any projected separation greater than 75 mas, which corresponds to 12 AU at an assumed distance of 160 pc (Lafrenière et al. 2008).

6.3. SB1: Single-lined Spectroscopic Binaries

T39 B (Ass Cha T 2-39, CHXR 36)— (Fig. 20) This is an SB1 that is part of a known visual triple system, T39, consisting of an inner $1''.2$ binary (Aa,Ab) of spectral

types K7 and M1.5, and an outer 4''5 component (B) of spectral type M1.5 (Reipurth & Zinnecker 1993). We obtained separate spectra of all three components (for T39 Aa & Ab). Components Aa and Ab show no evidence of additional companions. Therefore, since component B is an SB1, T39 is a quadruple system. The observed change in radial velocity of T39 B is 2.6 km s^{-1} over 0.8 yr.

RX J0415.8+3100 (V952 Per)— (Fig. 21) This is an SB1 with a substantial RV variability amplitude of at least 70 km s^{-1} during a period on the order of two days. Recall, the mass function equation $(m_2 \sin i)^3 / (m_1 + m_2)^2 = K_1^3 P (1 - e^2)^{3/2} / 2\pi G$ where m_1 and m_2 are the primary and secondary masses, i is the inclination angle, K_1 is the radial velocity semi-amplitude of the primary mass, P is the orbital period, e is the orbital eccentricity, and G is the gravitational constant. If we assume a primary star mass of $2.5 M_\odot$ (G6 type and 2 Myr), an RV semi-amplitude of 35 km s^{-1} , an orbital period of 2 d, and a circular orbit, then we estimate a companion mass of at least $0.42 M_\odot$ (M1 type). Given these mass estimates, the *R*-band flux ratio between the primary and an M1 companion would only be ~ 0.01 , which explains why the companion is not visible in our optical spectra. Kohler & Leinert (1998) report on an additional companion at 0''.94, making this system triple.

RX J0457.5+2014 (V1354 Tau)— (Fig. 22) This is an SB1 that shows a modest but significant 6 km s^{-1} increase in RV over 31 days. Kohler & Leinert (1998) report a companion B at 6''.86, which is too distant to be responsible for the radial velocity change of component A. Therefore, this system is triple.

7. SUMMARY AND CONCLUDING REMARKS

Binary and higher-order multiple systems are prevalent in young clusters, and studying the statistical properties of these systems offers indirect constraints on star formation. Here, we present a spectroscopic study of multiplicity for young stars in the Chamaeleon I and Taurus-Auriga star-forming regions. Our main results are as follows.

1. The spectroscopic multiplicity fractions for Cha I and Tau-Aur are similar to each other, and to those of field stars in the same mass and period regime (for details, see §5.1). This finding implies that the overall fraction of short period stellar companions could stabilize after initial formation.
2. Close multiplicity is not seen to depend on primary mass. The mass of the host star can become important in the separation regime of imaging surveys. For discussion, see §5.2.
3. There is no strong correlation between accretion and the frequency of systems with close companions, and thus, close stellar companions are unlikely the principal source of the accretion cutoff observed in WTTS (see §5.1). Moreover, if close companions are responsible solely for the accretion difference between CTTs and WTTSs then there should be a disparity in the proportion of spectroscopic binaries between these two populations, but this is not seen in our survey of Cha I and Tau-Aur.

By undertaking this extensive spectroscopic survey of T Tauri stars, we have gained some insight that could be beneficial to future efforts. First and foremost, we now know the main limiting factor for a radial velocity study of young stars is the strong intrinsic noise present in some objects. This noise would need to be reduced in some way in order both to detect lower mass companions more effectively, and to extend the measurement to longer orbital periods. Our radial velocity precision is sufficient to detect, at the time of this writing, a few dozen of the known hot Jupiter planets, which have radial velocity semi-amplitudes of a few 100 m s^{-1} . If such planets were to be detected around pre-main sequence stars, it would provide direct constraints on their formation and migration timescales. For young stars, one way to reduce the intrinsic noise is to observe at infrared wavelengths (Martín et al. 2006; Huélamo et al. 2008). Another option is to average out the noise by observing over its characteristic period, i.e., the rotation period of the noisy star. To some extent, we have already done this by taking multiple spectra of the same targets during an observing run. Ideally, one would multiplex observations, e.g., by using multiple fibers as in VLT/FLAMES. This solution may not be suitable for star-forming regions like Taurus-Auriga, which span a large area of the sky, but it would probably be quite useful for compact regions like Chamaeleon.

We have also learned that our high resolution and S/N were extremely beneficial. It was probably a major reason we could find so many SB2 candidates; being able to resolve the stellar rotation helped us to determine the stability of the broadening functions. Less clear is whether one would really need the large spectral range, or whether a few well-chosen echelle orders would suffice. This consideration is relevant since it would determine whether or not multiplexing is feasible.

This paper was significantly improved by the many detailed suggestions from an anonymous referee. We would like to thank David Lafrenière, Robert Mathieu, Brian Lee, Russel White, and Eric Mamajek for enlightening discussions relating to the work presented in this paper. This paper includes data gathered with the 6.5 meter Magellan Telescopes located at Las Campanas Observatory, Chile. We would like to thank the Magellan staff for their tenacious effort and dedication in accommodating our aggressive observing program. This work was supported in part by Stockholm University grant dnr 301-3014-08 to DCN, Swedish National Space Board (contract 84/08:1) to AB, and NSERC grants to R.J. and M.H.vK., and by a fellowship to R.J. from the Radcliffe Institute for Advanced Study at Harvard University.

A. ESTIMATING SHORTEST POSSIBLE ORBITAL PERIODS

We define a close binary system as two bodies in orbit about a common center of mass where there is no consistent exchange of material between them, i.e., each object does not extend beyond its Roche lobe. The effective radius r_L of a Roche lobe for an object with mass M_1 in a binary system from the approximation of Eggleton (1983) is

$$r_L = \frac{0.49 q^{2/3}}{0.6 q^{2/3} + \ln(1 + q^{1/3})}, \quad 0 < q < \infty \quad (14)$$

where q is the mass ratio M_1/M_2 , and r_L is in units of the orbital separation. Furthermore, the orbital period P in days for an object that just fills its Roche lobe is

$$P(q, \rho) = 0.1375 \left(\frac{q}{1+q} \right)^{1/2} r_L^{-3/2} \rho^{-1/2} \quad (15)$$

where ρ is the mean density of the object in cgs units. Therefore, the theoretical shortest orbital period P_{\min}

of a binary system is

$$P_{\min} = \min\{\max[P(q, \rho_2), P(1/q, \rho_1)] \text{ for } 0 < q \leq 1\} \quad (16)$$

where ρ_1 and ρ_2 are the mean densities of the primary and secondary objects, respectively. Using the densities derived from the models of D'Antona & Mazzitelli (1997), we estimate the shortest possible orbital period for a typical ~ 2 Myr old T Tauri star in our survey ($0.6 M_{\odot}$; $1.4 R_{\odot}$) with a stellar mass companion is approximately 0.8 days.

REFERENCES

- Ahmic, M., Jayawardhana, R., Brandeker, A., Scholz, A., van Kerkwijk, M. H., Delgado-Donate, E., & Froebrich, D. 2007, *ApJ*, 671, 2074
- Appenzeller, I., & Mundt, R. 1989, *ARA&A*, 1, 291
- Baraffe, I., Chabrier, G., Allard, F., & Hauschildt, P. H. 1998, *A&A*, 337, 403
- Bayes, T., Price, R., & Canton, J. 1763, *Philosophical Transactions of the Royal Society of London*, 53, 370
- Bernstein, R., Sheckman, S. A., Gunnels, S. M., Mochnacki, S., & Athey, A. E. 2003, *SPIE*, 4841, 1694
- Boden, A. F., Akeson, R. L., Sargent, A. I., Carpenter, J. M., Ciardi, D. R., Bary, J. S., & Skrutskie, M. F. 2009, *ApJ*, 696, L111
- Boden, A. F., Torres, G., Sargent, A. I., Akeson, R. L., Carpenter, J. M., Boboltz, D. A., Massi, M., Ghez, A. M., Latham, D. W., Johnston, K. J., Menten, K. M., & Ros, E. 2007, *ApJ*, 670, 1214
- Branch, D. 1976, *ApJ*, 210, 392
- Brandeker, A., Jayawardhana, R., Khavari, P., Haisch, K. E., & Mardones, D. 2006, *ApJ*, 652, 1572
- Brandeker, A., Jayawardhana, R., & Najita, J. 2003, *AJ*, 126, 2009
- Brandeker, A., Liseau, R., Artymowicz, P., & Jayawardhana, R. 2001, *ApJ*, 561, L199
- Brandner, W., & Zinnecker, H. 1997, *A&A*, 321, 220
- Briceño, C., Luhman, K. L., Hartmann, L., Stauffer, J. R., & Kirkpatrick, J. D. 2002, *ApJ*, 580, 317
- Correia, S., Zinnecker, H., Ratzka, T., & Sterzik, M. F. 2006, *A&A*, 459, 909
- Damjanov, I., Jayawardhana, R., Scholz, A., Ahmic, M., Nguyen, D. C., Brandeker, A., & van Kerkwijk, M. H. 2007, *ApJ*, 670, 1337
- D'Antona, F., & Mazzitelli, I. 1997, *Memorie della Societa Astronomia Italiana*, 68, 807
- Delgado-Donate, E. J., Clarke, C. J., Bate, M. R., & Hodgkin, S. T. 2004, *MNRAS*, 351, 617
- Duchêne, G., Bouvier, J., & Simon, T. 1999, *A&A*, 343, 831
- Duchêne, G., Delgado-Donate, E., Haisch, K. E., Loinard, L., & Rodríguez, L. F. 2007, in *Protostars and Planets V* ed. B. Reipurth, D. Jewitt, & K. Keil (Tucson, AZ: Univ. Arizona Press), 379
- Duchêne, G., Ghez, A. M., McCabe, C., & Weinberger, A. J. 2003, *ApJ*, 592, 288
- Duquenois, A., & Mayor, M. 1991, *A&A*, 248, 485
- Eggleton, P. P. 1983, *ApJ*, 268, 368
- Fazio, G. G., et al. 2004, *ApJS*, 154, 10
- Fischer, D. A., & Marcy, G. W. 1992, *ApJ*, 396, 178
- Ghez, A. M., McCarthy, D. W., Patience, J. L., & Beck, T. L. 1997a, *ApJ*, 481, 378
- Ghez, A. M., Neugebauer, G., & Matthews, K. 1993, *AJ*, 106, 2005
- Ghez, A. M., White, R. J., & Simon, M. 1997b, *ApJ*, 490, 353
- Goodwin, S. P., Whitworth, A. P., & Ward-Thompson, D. 2004, *A&A*, 414, 633
- Gray, D. F. 2005, *The Observation and Analysis of Stellar Photospheres* (Cambridge: Cambridge Univ. Press)
- Guenther, E. W., Esposito, M., Mundt, R., Covino, E., Alcalá, J. M., Cusano, F., & Stecklum, B. 2007, *A&A*, 467, 1147
- Hoaglin, D. C., Mosteller, F., & Tukey, J. W. 2000, *Understanding Robust and Exploratory Data Analysis* (New York: Wiley)
- Huélamo, N., Figueira, P., Bonfils, X., Santos, N. C., Pepe, F., Gillon, M., Azevedo, R., Barman, T., Fernández, M., di Folco, E., Guenther, E. W., Lovis, C., Melo, C. H. F., Queloz, D., & Udry, S. 2008, *A&A*, 489, L9
- Huerta, M., Johns-Krull, C. M., Prato, L., Hartigan, P., & Jaffe, D. T. 2008, *ApJ*, 678, 472
- Ireland, M. J., & Kraus, A. L. 2008, *ApJ*, 678, L59
- Jayawardhana, R., Mohanty, S., & Basri, G. 2003, *ApJ*, 592, 282
- Joergens, V. 2006, *A&A*, 448, 655
- Kenyon, S. J., Dobrzycka, D., & Hartmann, L. 1994, *AJ*, 108, 1872
- Köhler, R., & Leinert, C. 1998, *A&A*, 331, 977
- Köhler, R., Petr-Gotzens, M. G., McCaughrean, M. J., Bouvier, J., Duchêne, G., Quirrenbach, A., & Zinnecker, H. 2006, *A&A*, 458, 461
- Kraus, A. L., & Hillenbrand, L. A. 2007, *ApJ*, 662, 413
- Lafrenière, D., Jayawardhana, R., Brandeker, A., Ahmic, M., & van Kerkwijk, M. H. 2008, *ApJ*, 683, 844
- Leinert, C., Zinnecker, H., Weitzel, N., Christou, J., Ridgway, S. T., Jameson, R., Haas, M., & Lenzen, R. 1993, *A&A*, 278, 129
- Luhman, K. L. 2004a, *ApJ*, 602, 816
- . 2004b, *ApJ*, 617, 1216
- Martín, E. L., Guenther, E., Osorio, M. R. Z., Bouy, H., & Wainscoat, R. 2006, *ApJ*, 644, L75
- Mathieu, R. D. 1994, *ARA&A*, 32, 465
- Mathieu, R. D., Ghez, A. M., Jensen, E. L. N., & Simon, M. 2000, in *Protostars and Planets IV*, ed. V. Mannings, A. P. Boss, & S. S. Russell (Tucson, AZ: Univ. Arizona Press), 703
- Mathieu, R. D., Stassun, K., Basri, G., Jensen, E. L. N., Johns-Krull, C. M., Valenti, J. A., & Hartmann, L. W. 1997, *AJ*, 113, 1841
- Maxted, P. F. L., Jeffries, R. D., Oliveira, J. M., Naylor, T., & Jackson, R. J. 2008, *MNRAS*, 385, 2210
- Melo, C. H. F. 2003, *A&A*, 410, 269
- Mundt, R., Walter, F. M., Feigelson, E. D., Finkenzeller, U., Herbig, G. H., & Odell, A. P. 1983, *ApJ*, 269, 229
- Nguyen, D. C., Jayawardhana, R., van Kerkwijk, M. H., Brandeker, A., Scholz, A., & Damjanov, I. 2009a, *ApJ*, 695, 1648
- Nguyen, D. C., Scholz, A., van Kerkwijk, M. H., Jayawardhana, R., & Brandeker, A. 2009b, *ApJ*, 694, L153
- Nidever, D. L., Marcy, G. W., Butler, R. P., Fischer, D. A., & Vogt, S. S. 2002, *ApJS*, 141, 503
- Oasa, Y., Tamura, M., & Sugitani, K. 1999, *ApJ*, 526, 336
- Raghavan, D., McAlister, H. A., Henry, T. J., Latham, D. W., Marcy, G. W., Mason, B. D., Gies, D. R., White, R. J., & ten Brummelaar, T. A. 2010, *ApJS*, 190, 1
- Reipurth, B., Lindgren, H., Nordstrom, B., & Mayor, M. 1990, *A&A*, 235, 197
- Reipurth, B., & Zinnecker, H. 1993, *A&A*, 278, 81
- Reipurth, B., Guimarães, M. M., Connelley, M. S., & Bally, J. 2007, *AJ*, 134, 2772
- Rucinski, S. 1999, in *ASP Conf. Ser. 185, Precise Stellar Radial Velocities*, IAU Colloquium 170, ed. J. B. Hearnshaw & C. D. Scarfe, (San Francisco, CA: ASP), 82

- Sherry, W. H., Walter, F. M., & Wolk, S. J. 2004, *AJ*, 128, 2316
- Simon, M., Ghez, A. M., Leinert, C., Cassar, L., Chen, W. P., Howell, R. R., Jameson, R. F., Matthews, K., Neugebauer, G., & Richichi, A. 1995, *ApJ*, 443, 625
- Steffen, A. T., Mathieu, R. D., Lattanzi, M. G., Latham, D. W., Mazeh, T., Prato, L., Simon, M., Zinnecker, H., & Loreggia, D. 2001, *AJ*, 122, 997
- Walter, F. M., Brown, A., Mathieu, R. D., Myers, P. C., & Vrba, F. J. 1988, *AJ*, 96, 297
- Whittet, D. C. B., Prusti, T., Franco, G. A. P., Gerakines, P. A., Kilkenny, D., Larson, K. A., Wesselius, P. R. 1997, *A&A*, 327, 1194
- Wilson, O. C. 1941, *ApJ*, 93, 29
- Woitas, J. 2003, *A&A*, 406, 685
- Zucker, S., & Mazeh, T. 1994, *ApJ*, 420, 806

Region: Cha
 Object: T55
 RA Dec (J2000.0): 11 13 33.57 $-76^{\circ} 35' 37.4''$
 Spectral Type: M4.5

S/N @ H α : 4.8 ± 0.7
 H α 10% width: 165 ± 59 km/s
 $v \sin i$: See caption
 EW CaII: Not available
 [3.6] – [8.0]: -0.02 ± 0.16

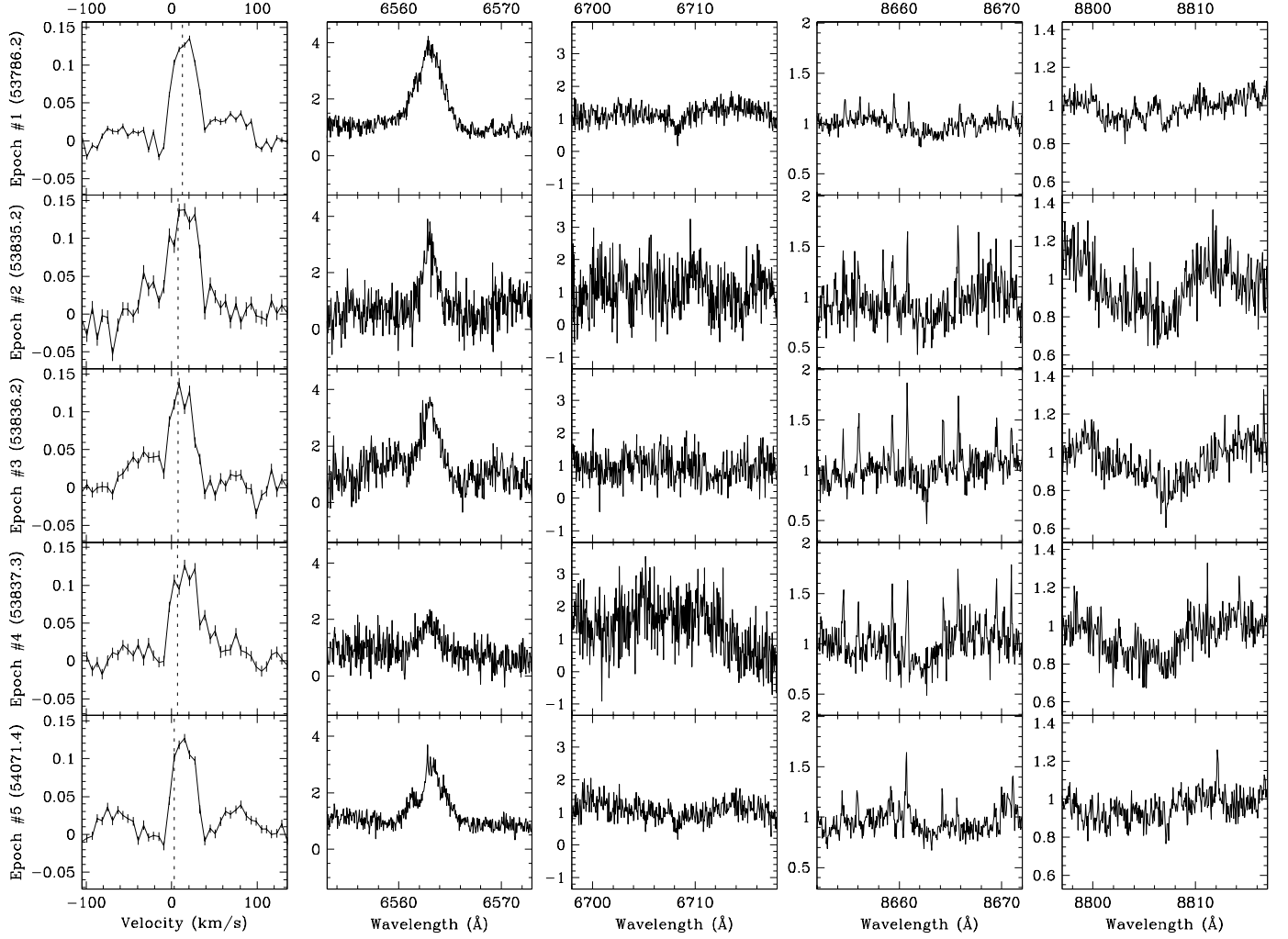
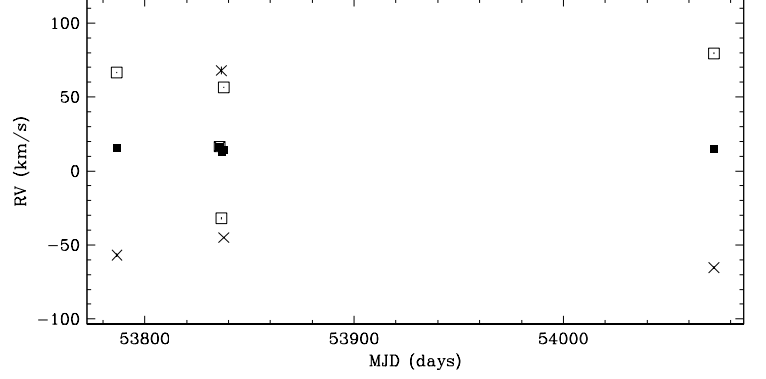


FIG. 10.— T55 is an SB3. The two fainter sources show large accelerations while the radial velocity of the brighter source is stable. This suggests a triple system comprised of a close binary in orbit with a farther away more massive star. By fitting the broadening function to three rotational broadening line profiles, we estimate the sources have an A–B flux ratio of 0.38 ± 0.08 , an A–C flux ratio of 0.19 ± 0.08 , and the A, B and C sources have $v \sin i$ of 23 ± 2 km s $^{-1}$, 34 ± 4 km s $^{-1}$ and 31.0 ± 1.6 km s $^{-1}$, respectively. The narrow emission lines in the spectra near 8662 Å are from the night sky. This target has been previously reported by Lafrenière et al. (2008) to have no resolved companions.

Region: Tau
 Object: RX J0412.8+2442
 RA Dec (J2000.0): 04 12 51.22 +24 41 44.3
 Spectral Type: G9

S/N @ H α : 24.0 ± 1.8
 H α 10% width: 0 km/s
 $v \sin i$: See caption
 EW CaII: $-0.11 \pm 0.00 \text{ \AA}$
 [3.6] - [8.0]: Not available

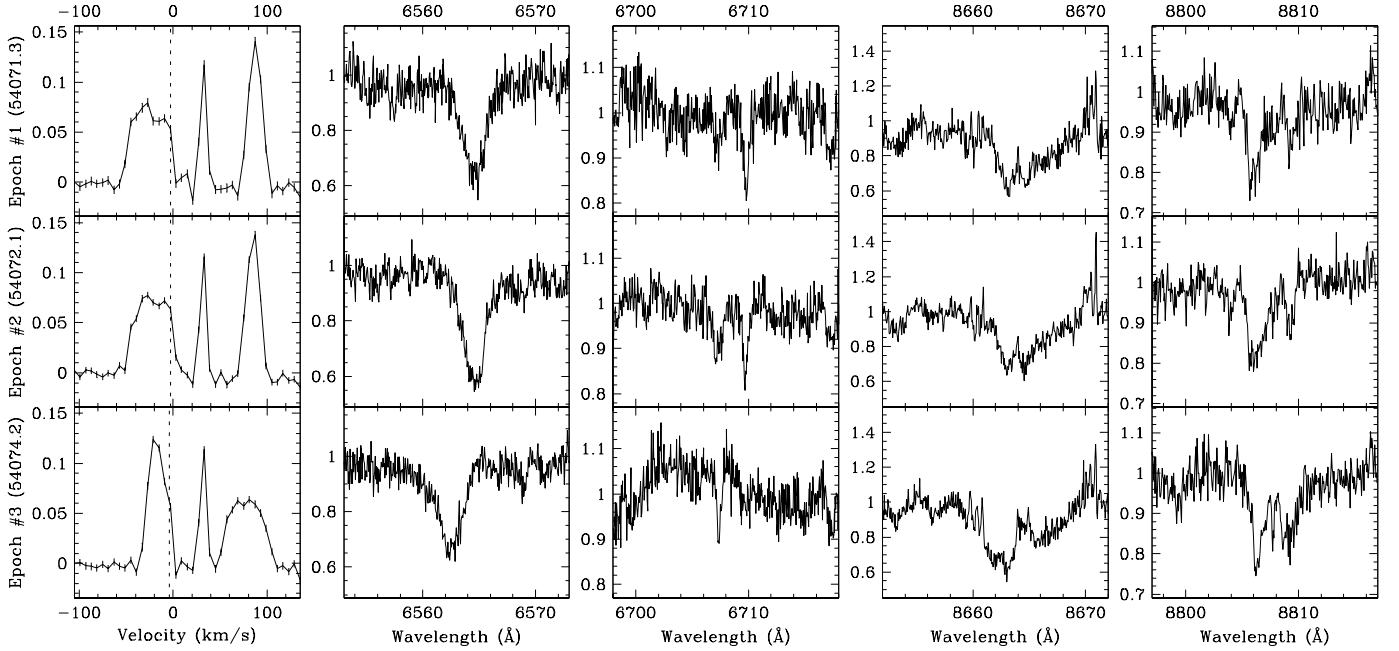
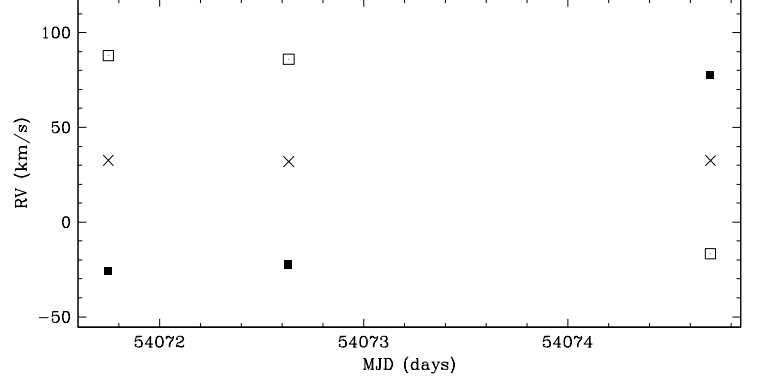


FIG. 11.— RX J0412.8+2442 is an SB3. The two of the sources show rapid radial acceleration. The radial velocity stable source has much less flux, and is likely a relatively farther away lower-mass companion. By fitting the broadening function to three rotational broadening line profiles, we estimate the sources have an A–B flux ratio of 0.88 ± 0.12 , an A–C flux ratio of 0.36 ± 0.04 , and the A, B and C sources have $v \sin i$ of $28.50 \pm 0.12 \text{ km s}^{-1}$, $15.1 \pm 1.5 \text{ km s}^{-1}$ and $7.4 \pm 0.3 \text{ km s}^{-1}$, respectively. This target has been previously reported by Kohler & Leinert (1998) to have no resolved companions.

Region: Tau
 Object: V773 Tau
 RA Dec (J2000.0): 04 14 12.92 +28 12 12.4
 Spectral Type: K3

S/N @ H α : 40.0 ± 2.5
 H α 10% width: 433 ± 51 km/s
 $v \sin i$: See caption
 EW CaII: -0.11 Å
 [3.6] - [8.0]: 1.61 ± 0.01

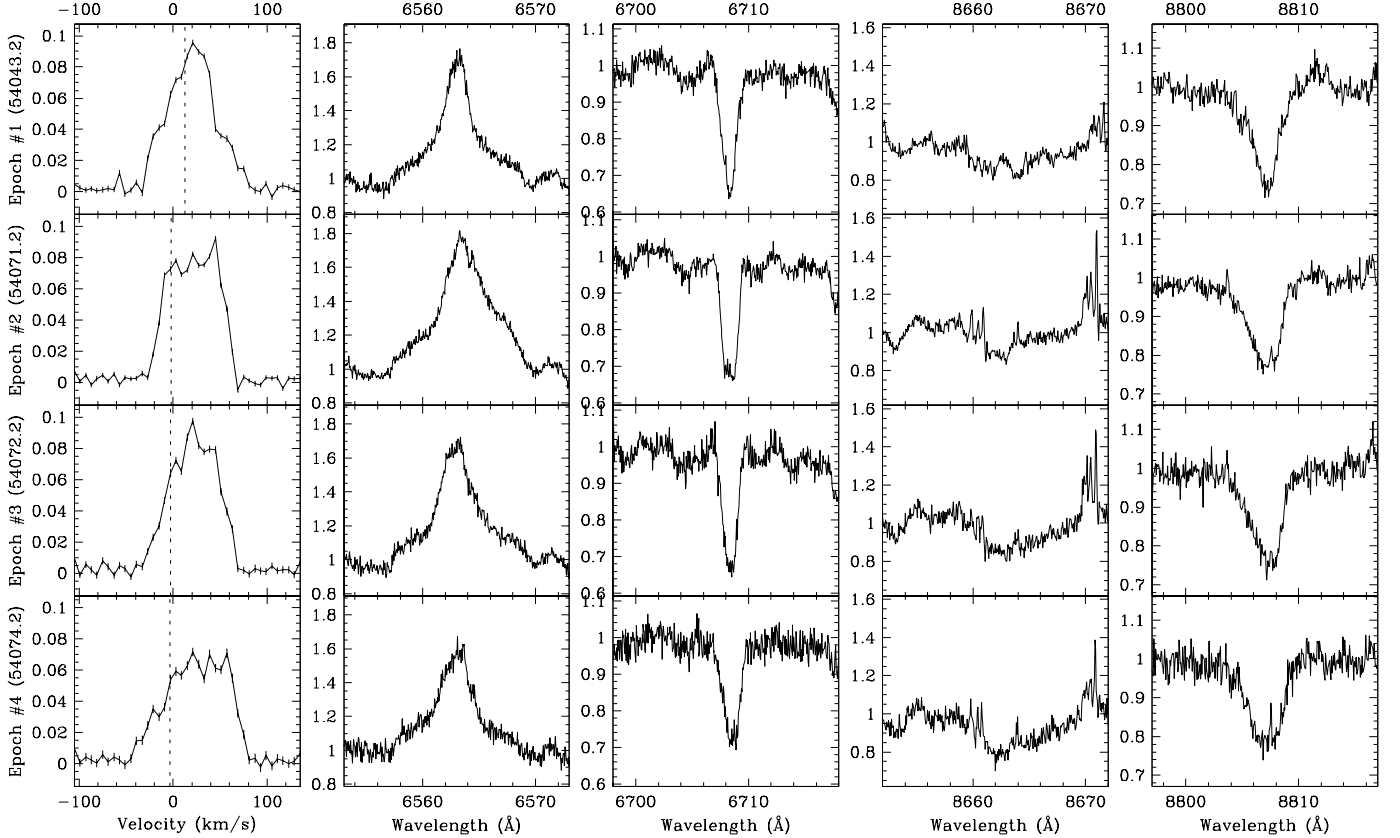
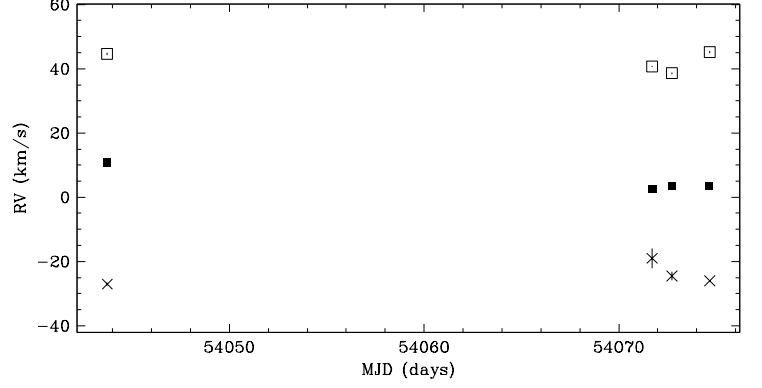


FIG. 12.— V773 Tau is an SB3. The broadening function appears to consist of three sources that fluctuate over time. By fitting the broadening function to three rotational broadening functions, we estimate the sources have an A–B flux ratio of 1.0 ± 0.3 , an A–C flux ratio of 0.09 ± 0.06 , and the A, B and C sources have $v \sin i$ of 27 ± 4 km s $^{-1}$, 28 ± 4 km s $^{-1}$ and 21 ± 7 km s $^{-1}$, respectively. However, these results and the derived radial velocities should be read with caution because of the broad and blended peaks in the broadening functions of this system which are difficult to decompose and fit reliably. This target has been previously reported by Duchêne et al. (2003), and Woitas (2003) as a quadruple system consisting of a spectroscopic binary (V773 Tau Aa,Ab) with a period of ~ 51 days and two wide companions (V773 Tau B,C) with an A–B and A–C separations of ~ 0.1 (~ 14 AU) and ~ 0.2 (~ 28 AU) with an A–B $\Delta K \sim 0.33 - -2.22$ and an A–C $\Delta K \sim 1.84 - -2.85$. The radial velocities of the A and B components computed by (Boden et al. 2007) do not match well with the radial velocities we estimate because of our poor broadening function fits.

Region: Tau
Object: LkCa 3
RA Dec (J2000.0): 04 14 47.97 +27 52 34.7
Spectral Type: M1

S/N @ H α : 22.5 ± 1.5
H α 10% width: 187 ± 25 km/s
 $v \sin i$: See caption
EW CaII: -0.12 Å
[3.6] – [8.0]: Not available

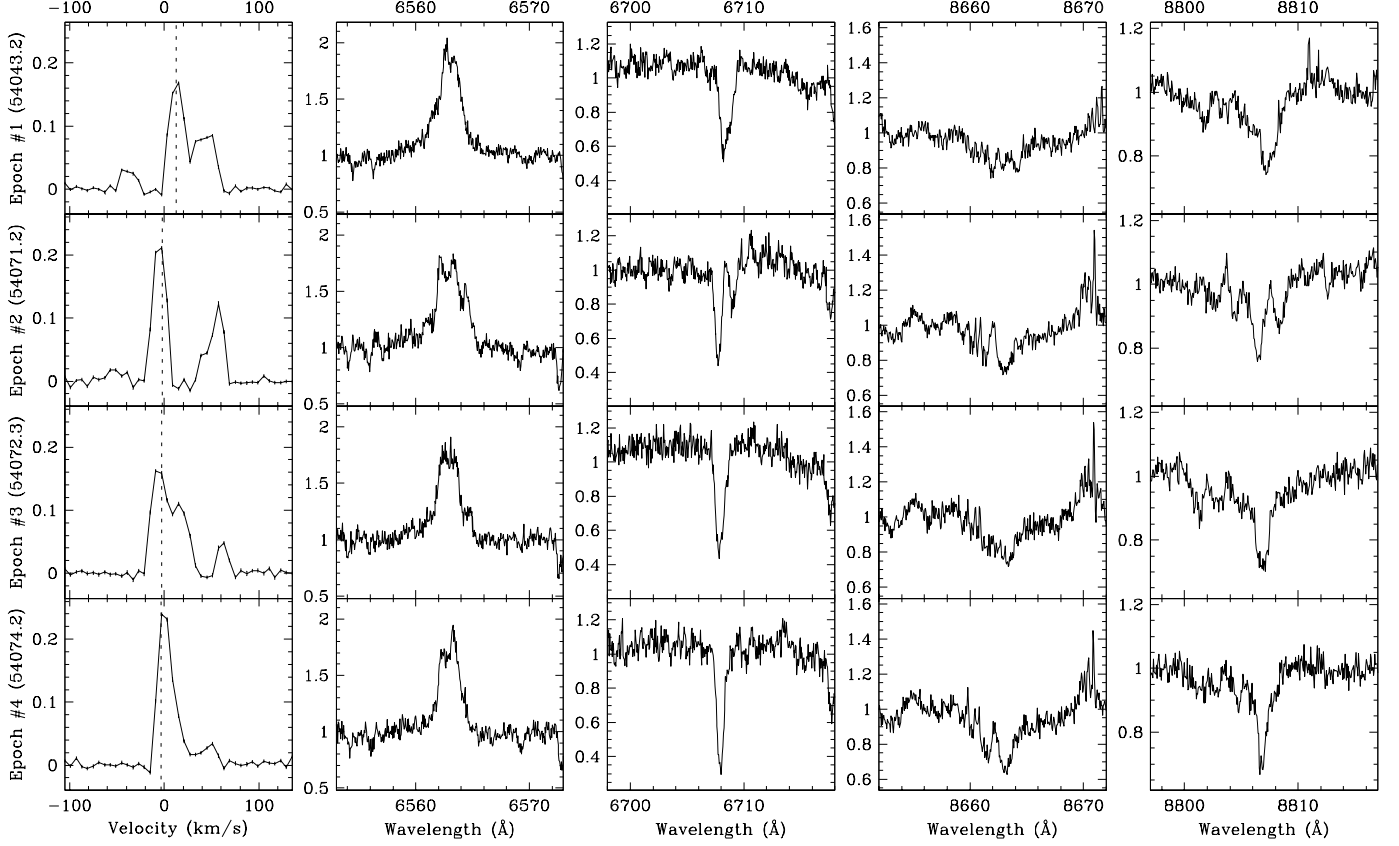
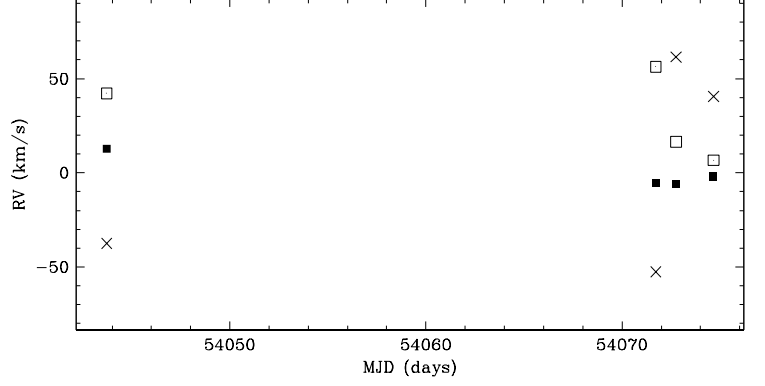


FIG. 13.— LkCa 3 is an SB3. The three sources also show radial acceleration and are very close companions. Therefore, the companions are not likely to be the previously resolved companion. By fitting the broadening function to three rotational broadening line profiles, we estimate the sources have an Aa–Ab1 flux ratio of 0.75 ± 0.13 , an Aa–Ab2 flux ratio of 0.21 ± 0.05 , and the Aa, Ab1 and Ab2 sources have $v \sin i$ of 12.0 ± 1.0 km s $^{-1}$, 16 ± 2 km s $^{-1}$ and 14 ± 4 km s $^{-1}$, respectively. This target has been previously reported by Leinert et al. (1993), and Ghez et al. (1993) to have a resolved companion with a separation of $0''.47$ – $0''.491$ (66–69 AU) at a position angle of 77° – 78° , and an R -band flux ratio of 0.47–0.92 (based on $\Delta K \sim 0.05$ – 0.42). However, there is no clear evidence in the broadening function of the resolved companion. Since the resolved companion has an expected circular orbital speed of ~ 3 km s $^{-1}$, another profile could be obscured if the central star and the resolved companion have similar projected rotational velocities. Therefore, the system is possibly a quadruple system consisting of a spectroscopic binary in orbit with another spectroscopic companion and a resolved companion.

Region: Cha
 Object: CHXR 12
 RA Dec (J2000.0): 11 03 56.83 -77 21 33.0
 Spectral Type: M3.5

S/N @ H α : 10.7 ± 0.8
 H α 10% width: 101 ± 8 km/s
 $v \sin i$: See caption
 EW CaII: -0.09 ± 0.04 Å
 [3.6] – [8.0]: 0.06 ± 0.08

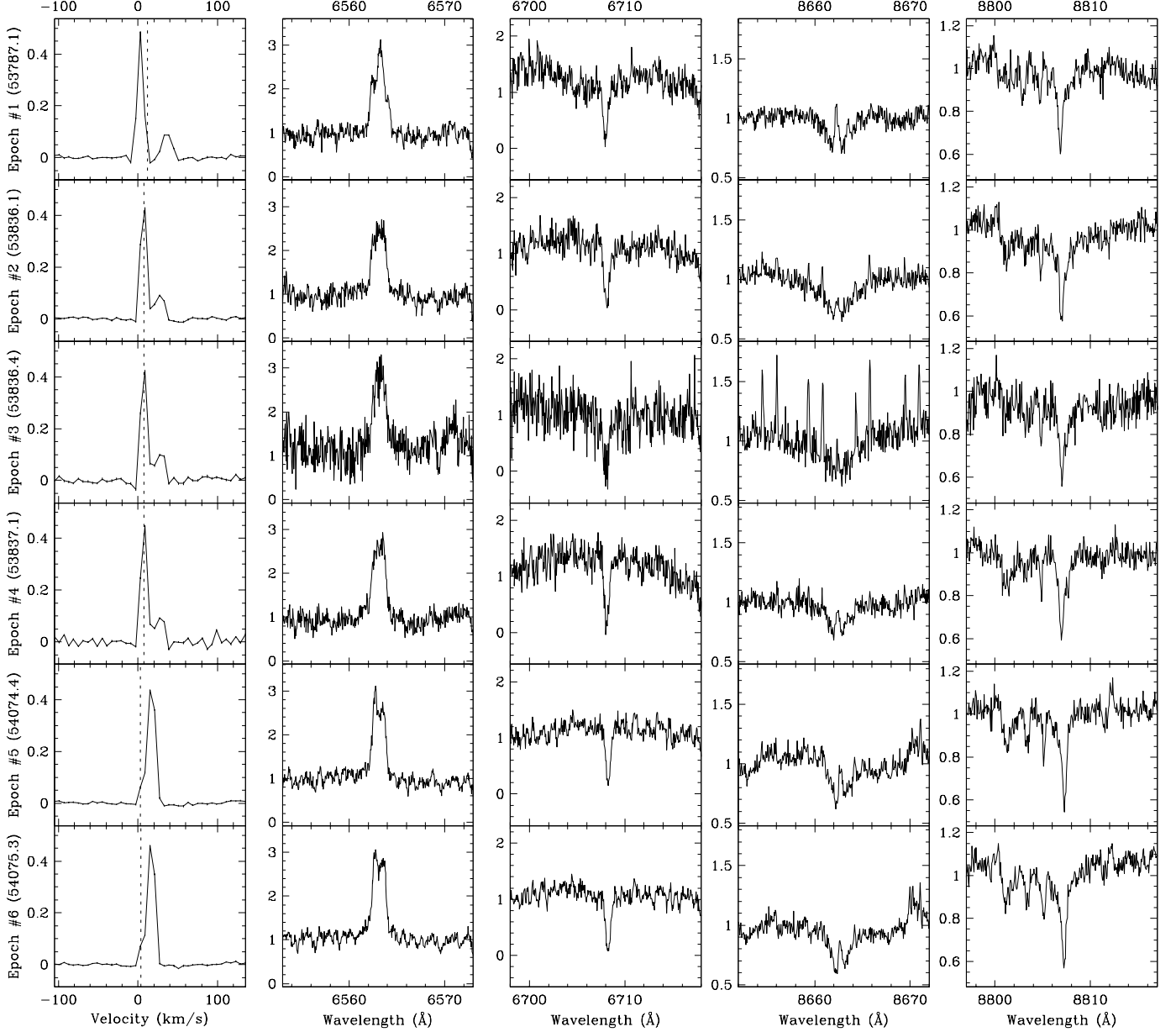
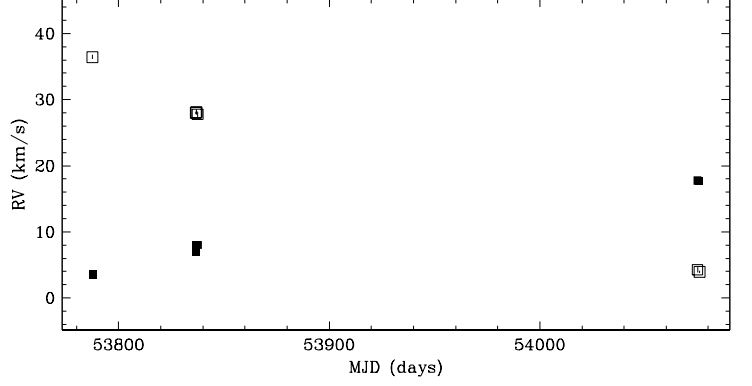


FIG. 14.— CHXR 12 is an SB2. Two sources can be seen in the broadening function, and both show acceleration. By fitting the broadening function to two rotational broadening line profiles, we estimate the two sources have a flux ratio of 0.20 ± 0.08 , and the A and B sources have $v \sin i$ of 8.99 ± 0.14 km s $^{-1}$ and 8 ± 2 km s $^{-1}$, respectively. For epoch #3, the narrow emission lines in the spectrum near 8662 Å are from the night sky. For epochs #5 & #6, the radial velocities from fitting the blended broadening functions were fairly robust because of the strong S/N ratio and the low $v \sin i$ of the components. This target has been previously reported by Lafrenière et al. (2008) to have no resolved companions.

Region: Cha
 Object: T42
 RA Dec (J2000.0): 11 09 53.41 -76 34 25.5
 Spectral Type: K5

S/N @ H α : 3.0 ± 0.7
 H α 10% width: 543 ± 83 km/s
 $v \sin i$: See caption
 EW CaII: -10.96 ± 9.24 Å
 [3.6] - [8.0]: Not available

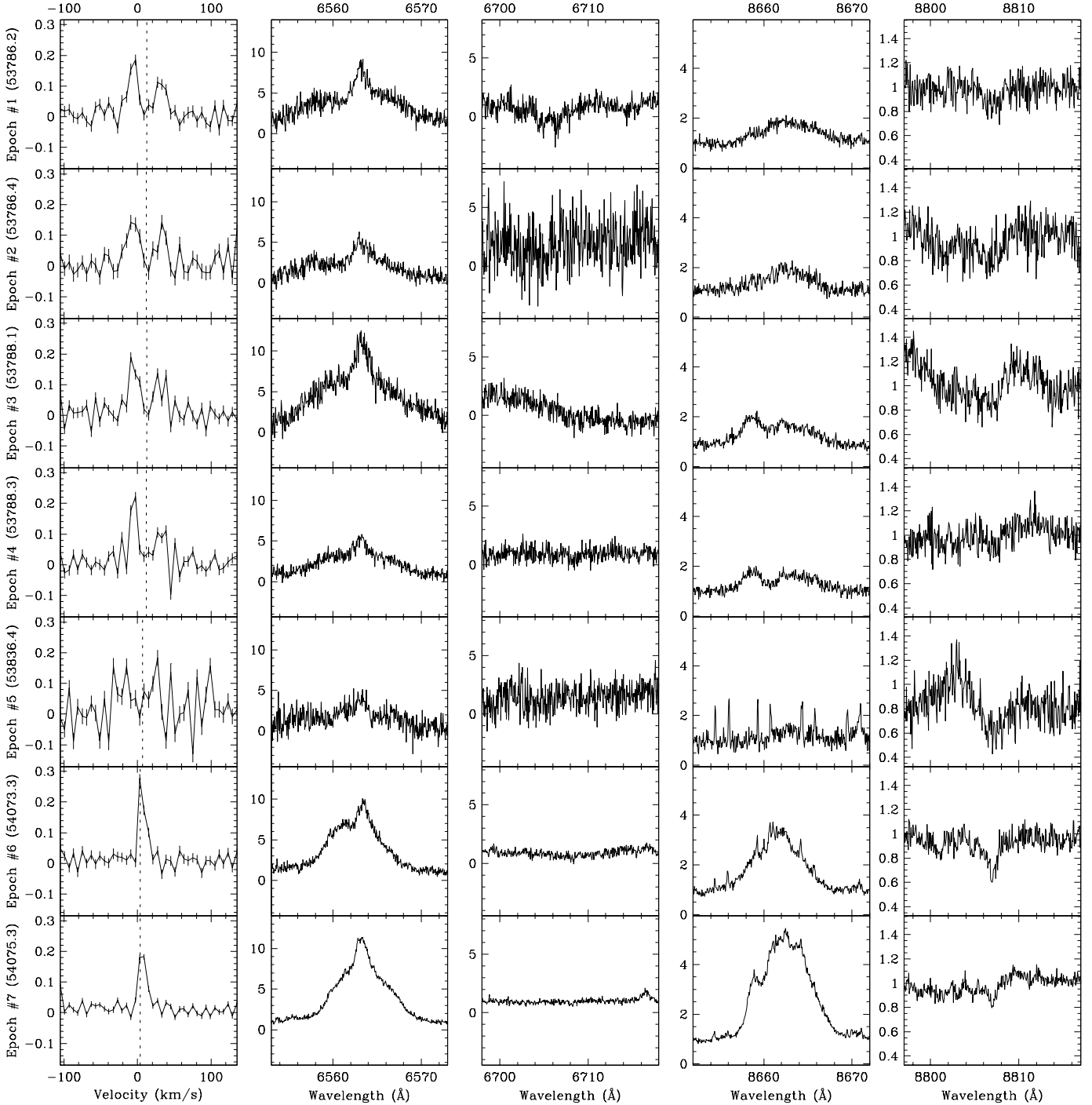
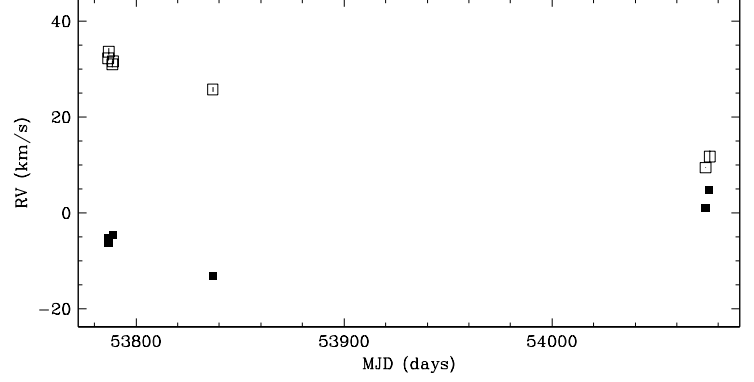


FIG. 15.— T42 is an SB2. The radial velocity estimate for epoch #5 is unreliable due to poor S/N. By fitting the broadening function to two rotational broadening line profiles, we estimate the two sources have a flux ratio of 0.8 ± 0.3 , and the A and B sources have $v \sin i$ of 11.4 ± 1.1 km s $^{-1}$ and 11.5 ± 1.5 km s $^{-1}$, respectively. For epoch #5, the narrow emission lines in the spectrum near 8662 Å are from the night sky. For epochs #6 & #7, the radial velocities from fitting the blended broadening functions were acceptable because of the decent S/N ratio. This target has been previously reported by Lafrenière et al. (2008) to have no resolved companions.

Region: Tau
 Object: V826 Tau
 RA Dec (J2000.0): 04 32 15.84 +18 01 38.7
 Spectral Type: K7

S/N @ H α : 21.6 ± 1.3
 H α 10% width: 139 ± 13 km/s
 $v \sin i$: See caption
 EW CaII: -0.22 ± 0.07 Å
 [3.6] - [8.0]: 0.09 ± 0.04

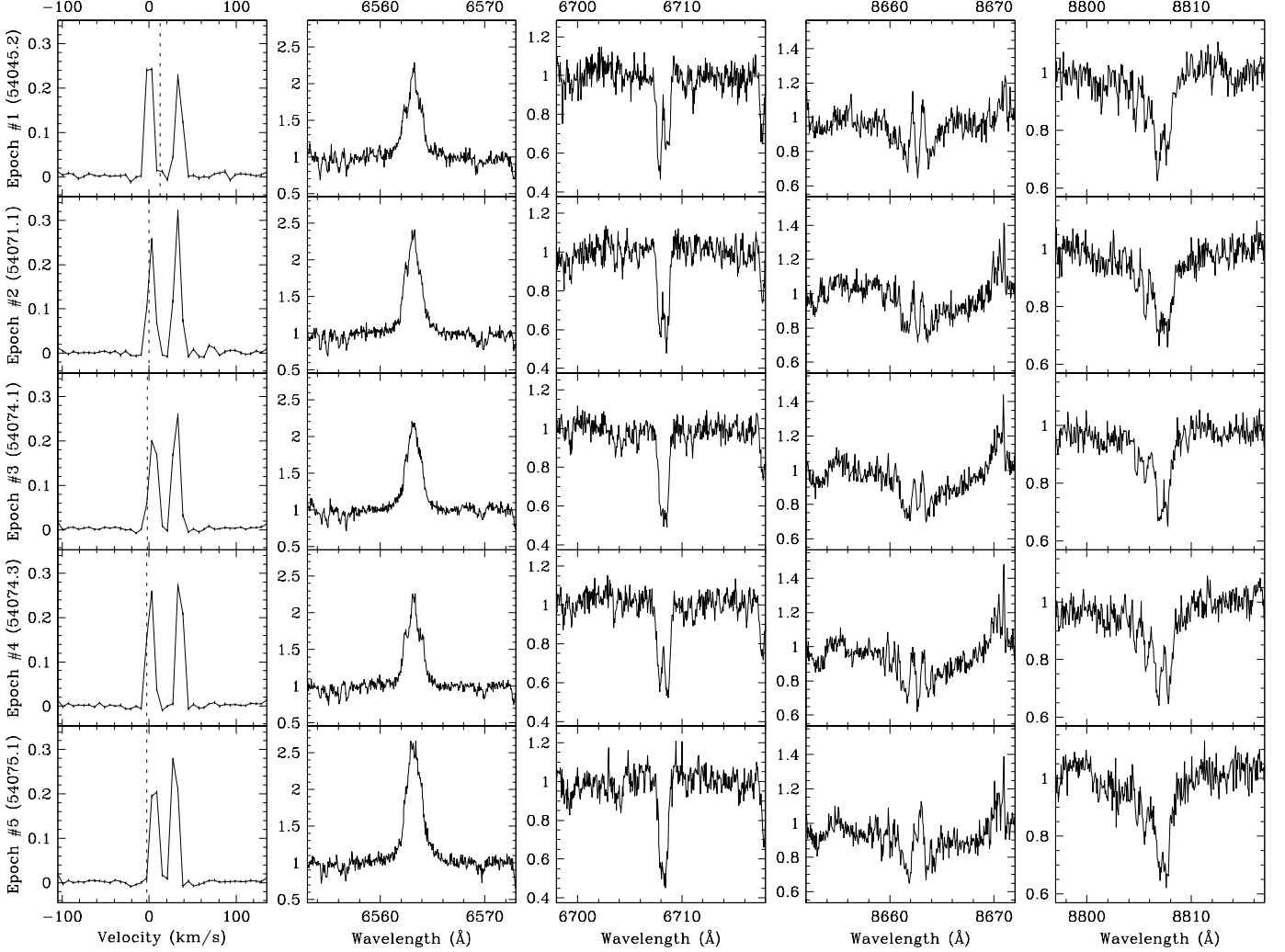
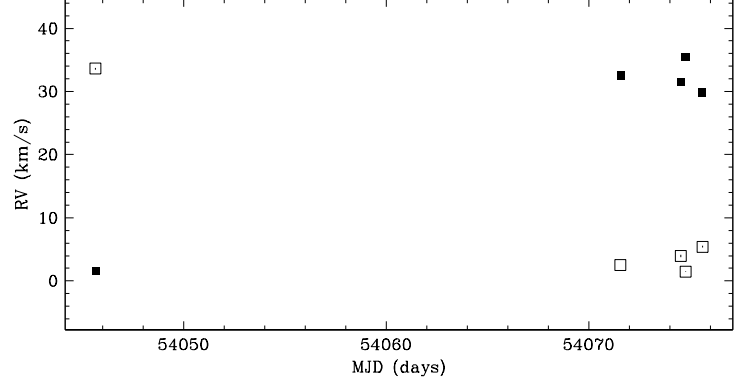


FIG. 16.— V826 Tau is an SB2. Two sources can be seen in the broadening function, and both show acceleration. By fitting the broadening function to two rotational broadening line profiles, we estimate the two sources have a flux ratio of 0.88 ± 0.06 , and the A and B sources have $v \sin i$ of 8.5 ± 0.5 km s $^{-1}$ and 9.3 ± 0.7 km s $^{-1}$, respectively. This target has been previously reported by Reipurth et al. (1990) as a spectroscopic binary (V826 Tau A+B) with a period of ~ 3.9 days. Furthermore, the extrapolated radial velocities from their orbital elements are consistent to within a few km s $^{-1}$ of our radial velocities estimates, which is well-matched given very short-period and the radial velocity semi-amplitudes of ~ 18 km s $^{-1}$.

Region: Tau
 Object: DQ Tau
 RA Dec (J2000.0): 04 46 53.05 +17 00 00.2
 Spectral Type: M0

S/N @ H α : 19.7 ± 1.3
 H α 10% width: 340 ± 22 km/s
 $v \sin i$: See caption
 EW CaII: -0.27 ± 0.12 Å
 [3.6] - [8.0]: 1.92 ± 0.03

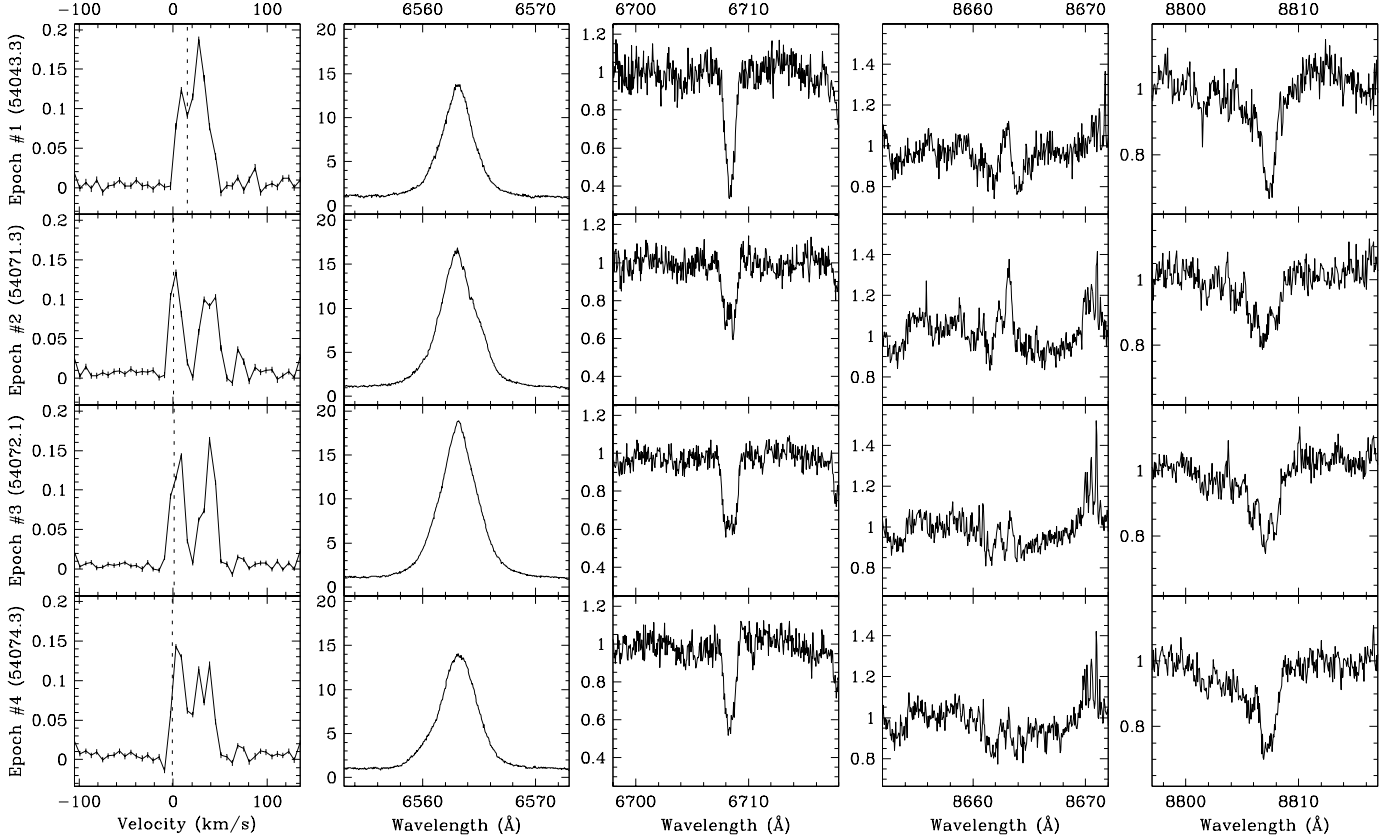
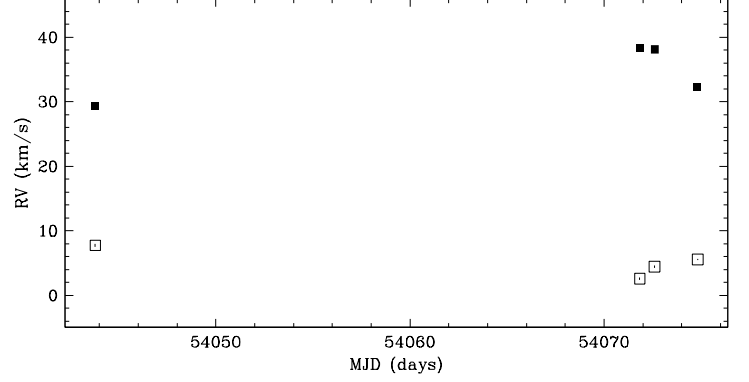


FIG. 17.— DQ Tau is an SB2. The two sources show radial acceleration. By fitting the broadening function to two rotational broadening line profiles, we estimate the two sources have a flux ratio of 0.78 ± 0.18 , and the A and B sources have $v \sin i$ of 14.7 ± 1.6 km s $^{-1}$ and 11.3 ± 0.7 km s $^{-1}$, respectively. This target has been previously reported by Mathieu et al. (1997) as a spectroscopic binary with a period of 15.8 days. Furthermore, the radial velocities extrapolated from the orbital elements given by Mathieu et al. (1997) are consistent to within a few km s $^{-1}$ of our measured radial velocities, which is not a bad match given the estimated radial velocity semi-amplitudes of ~ 20 km s $^{-1}$.

Region: Tau
 Object: HBC 427
 RA Dec (J2000.0): 04 56 02.02 +30 21 03.8
 Spectral Type: K5

S/N @ H α : 29.2 ± 2.0
 H α 10% width: 145 ± 13 km/s
 $v \sin i$: See caption
 EW CaII: -0.12 ± 0.02 Å
 [3.6] - [8.0]: 0.16 ± 0.04

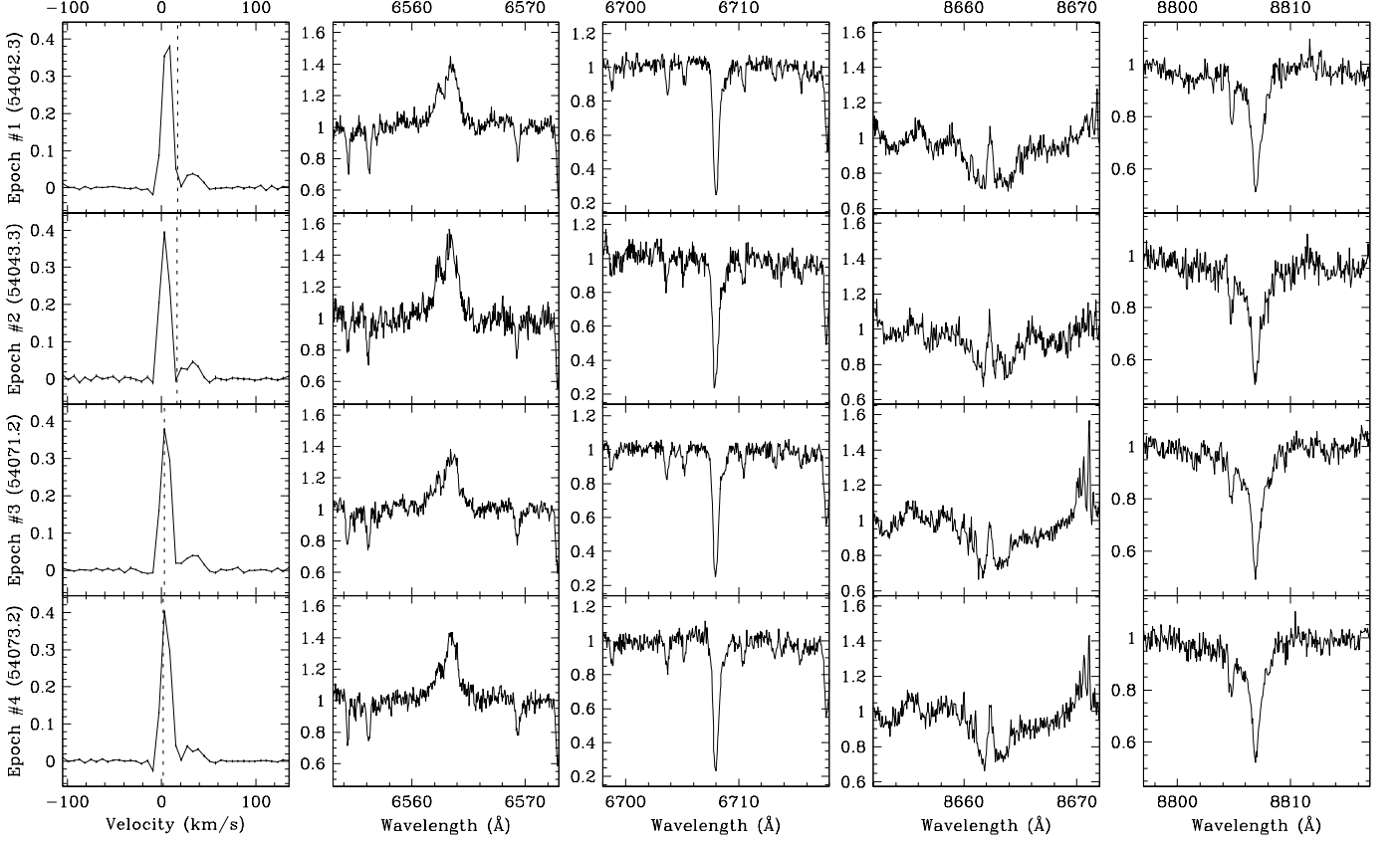
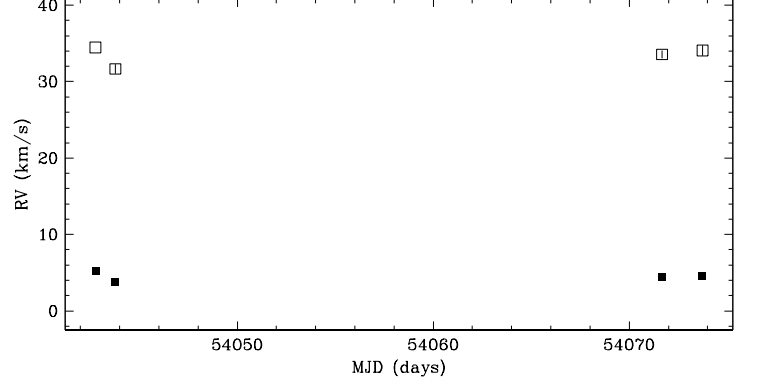


FIG. 18.— HBC 427 is an SB2. Two sources can be seen in the profile: a peak at $\sim 5 \text{ km s}^{-1}$ and another peak at $\sim 30 \text{ km s}^{-1}$. By fitting the broadening function to two rotational broadening line profiles, we estimate the two sources have a flux ratio of 0.157 ± 0.014 , and the A and B sources have $v \sin i$ of $9.9 \pm 0.3 \text{ km s}^{-1}$ and $14.5 \pm 0.5 \text{ km s}^{-1}$, respectively. This target has been previously reported by Steffen et al. (2001) as a spectroscopic binary with a period of ~ 2500 days.

Region: Cha
 Object: T31 A
 RA Dec (J2000.0): 11 08 01.49 $-77^{\circ} 42' 28.9''$
 Spectral Type: K3

S/N @ H α : 15.3 ± 1.5
 H α 10% width: 471 ± 55 km/s
 $v \sin i$: See caption
 EW CaII: -6.74 ± 2.26 Å
 [3.6] – [8.0]: Not available

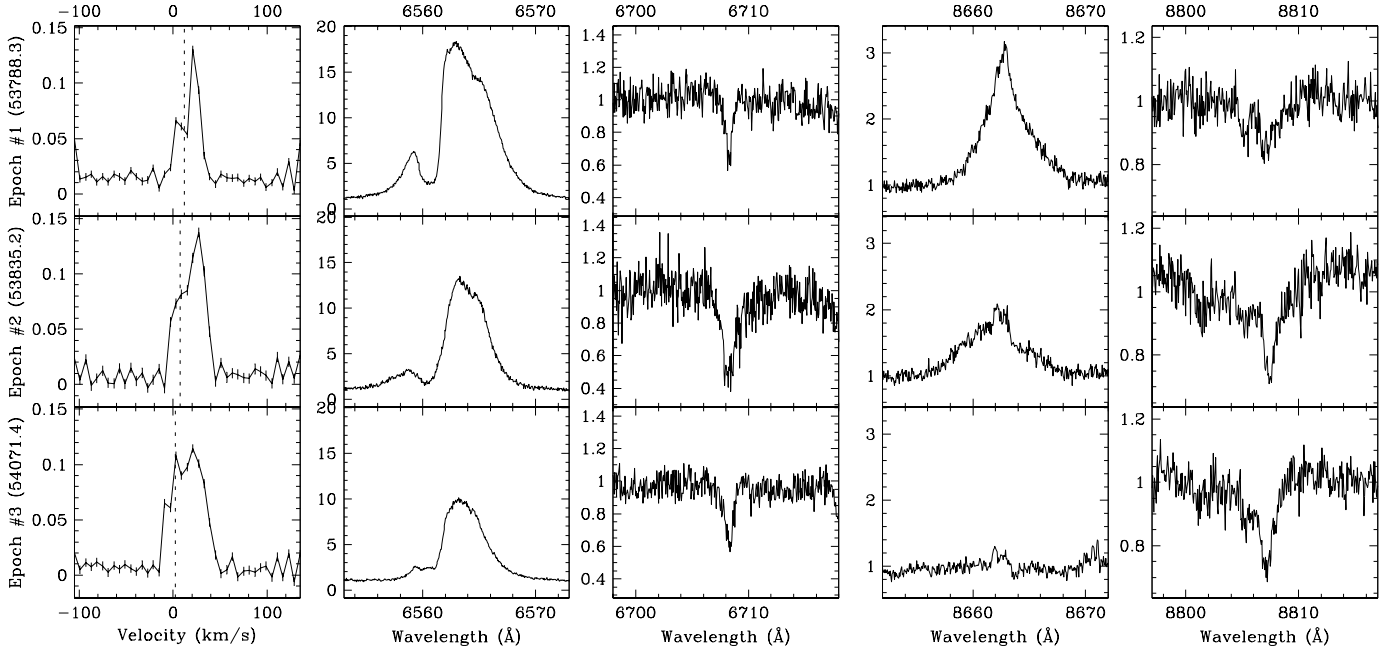
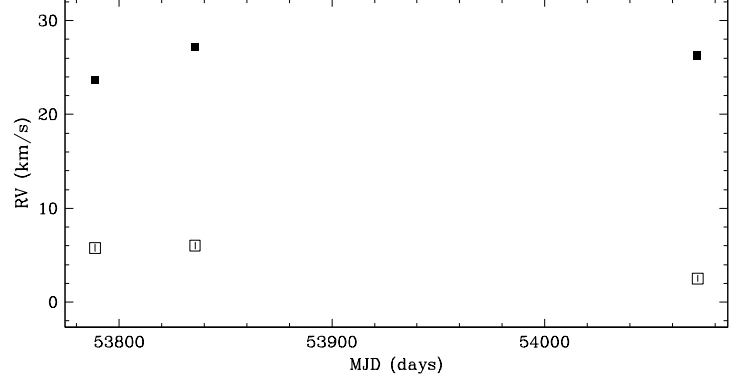


FIG. 19.— T31 A is a suspected SB2. Two sources can be seen in the profile: a peak at ~ 25 km s $^{-1}$ and another peak at ~ 5 km s $^{-1}$. By fitting the broadening function to two rotational broadening line profiles, we estimate the two sources have a flux ratio of 0.7 ± 0.3 , and the a and b sources have $v \sin i$ of 13 ± 2 km s $^{-1}$ and 13 ± 3 km s $^{-1}$, respectively. This target has been previously reported by Lafrenière et al. (2008) to have a resolved companion with a separation of $\sim 0''.652$ (~ 91 AU) at a position angle of $\sim 178^\circ$, and an R -band flux ratio of ~ 0.03 (based on $\Delta K \sim 1.74$). Given the flux ratio, the expected contribution to the broadening function from the resolved companion is negligible. The companion was resolved in the guide camera during good seeing conditions and was indeed faint, so it cannot have contributed to the profile.

Region: Cha
 Object: T39 B
 RA Dec (J2000.0): 11 09 11.72 -77 29 12.5
 Spectral Type: M1.5

S/N @ H α : 7.2 ± 0.8
 H α 10% width: 106 ± 13 km/s
 $v \sin i$: 13 ± 0.4 km/s
 EW CaII: -0.25 ± 0.03 Å
 [3.6] - [8.0]: Not available

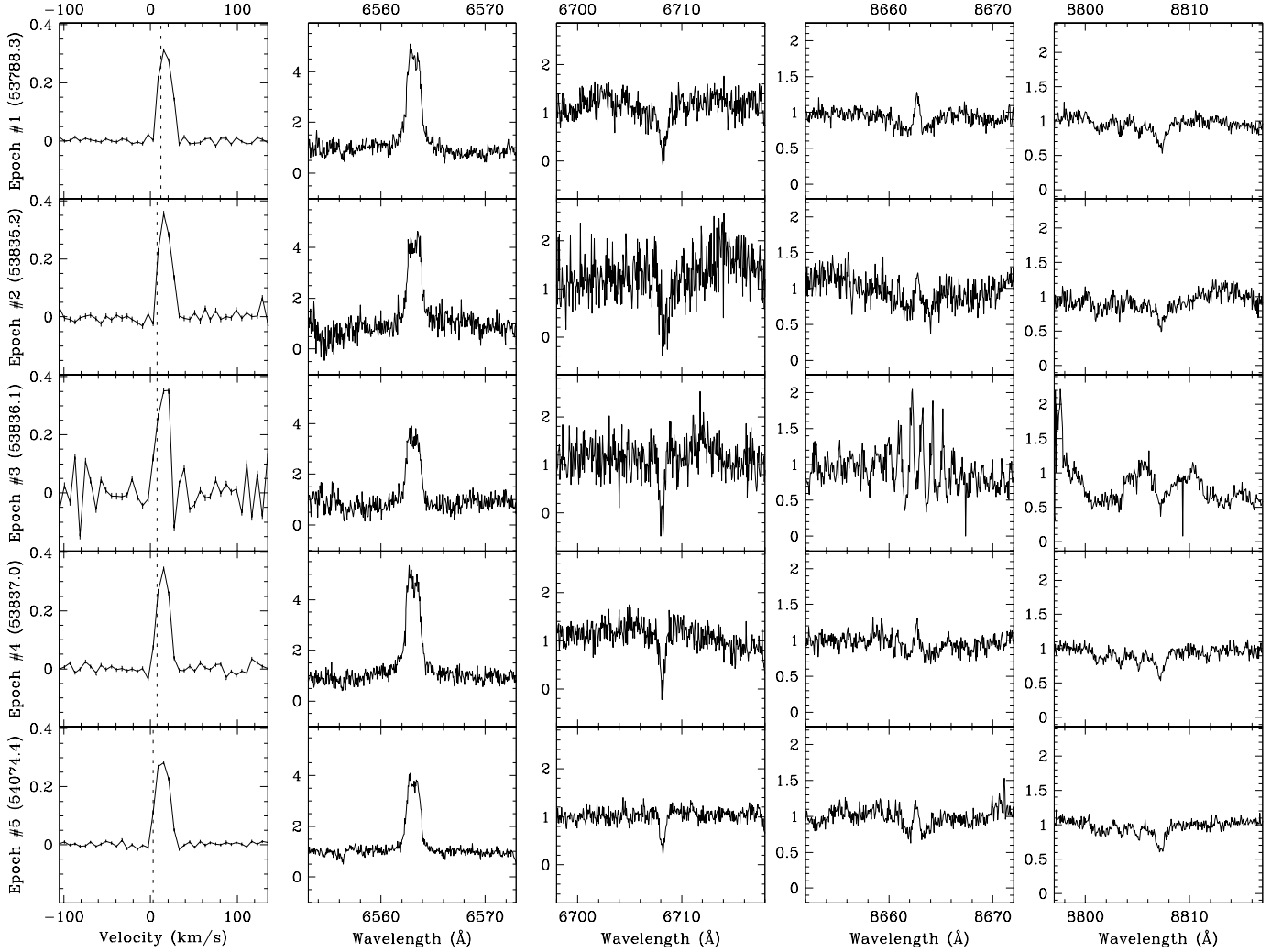
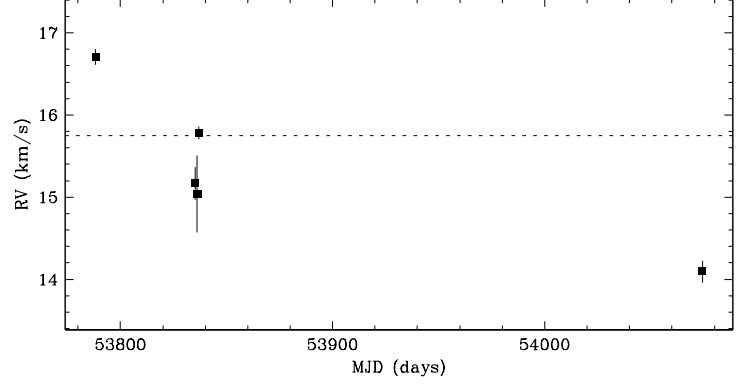


FIG. 20.— T39 B is an SB1. The overall radial velocity scatter is significant relative to the measurement uncertainties and to scatter observed within each observing run. The radial velocity scatter is larger than expected for a star with a $v \sin i$ of 13 km s^{-1} , and thus is unlikely to be due to star spots. The lack of radial velocity offset from the cluster velocity ($\sim 16 \text{ km s}^{-1}$) implies a long orbital period and a small velocity amplitude. If star spots are responsible for the changes in radial velocity, based on observed $v \sin i$ ($\sim 13 \text{ km s}^{-1}$) and model stellar radius ($\sim 1.3 R_{\odot}$), one would expect variations on a maximum timescale of ~ 5.1 days. From the stable results of the second observing run (epoch #2, #3 and #4) which spans 2.8 days compared to the overall range of radial velocities, it is unlikely that the radial velocity trends are the result of star spots. This target has been previously reported by Lafrenière et al. (2008) to be a component star of a resolved triple system (T39 Aa, Ab, B) with a separation of $\sim 4''.497$ (~ 630 AU) at a position angle of $\sim 70^{\circ}8$, and a B–Aa R -band flux ratio of ~ 0.13 (based on $\Delta K \sim 0.77$). Given the separation, the expected contribution to the broadening function from the resolved companion is negligible.

Region: Tau
 Object: RX J0415.8+3100
 RA Dec (J2000.0): 04 15 51.38 +31 00 35.6
 Spectral Type: G6

S/N @ H α : 20.2 ± 1.5
 H α 10% width: 0 km/s
 $v \sin i$: 32 ± 1.9 km/s
 EW CaI: Not available
 [3.6] – [8.0]: Not available

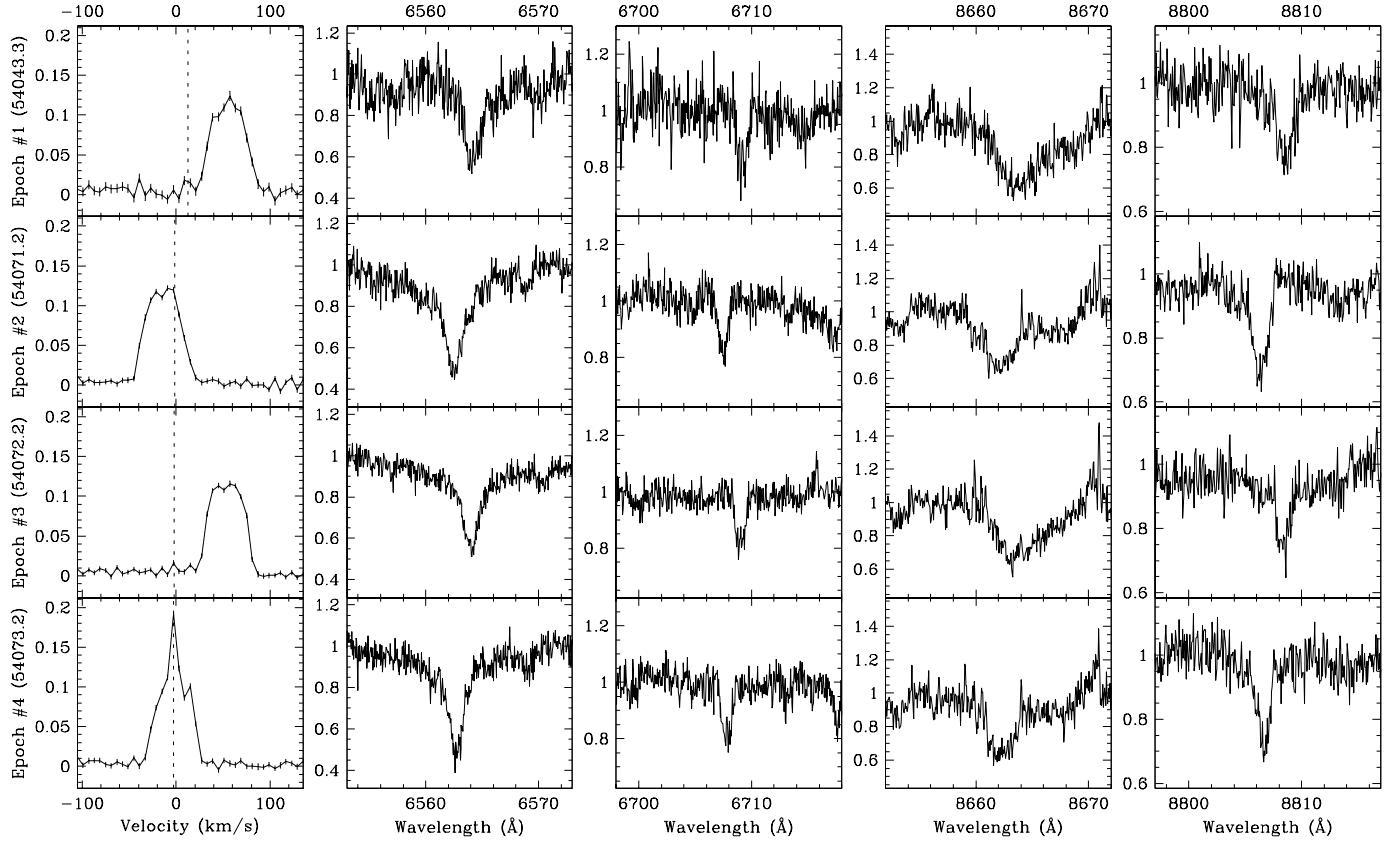
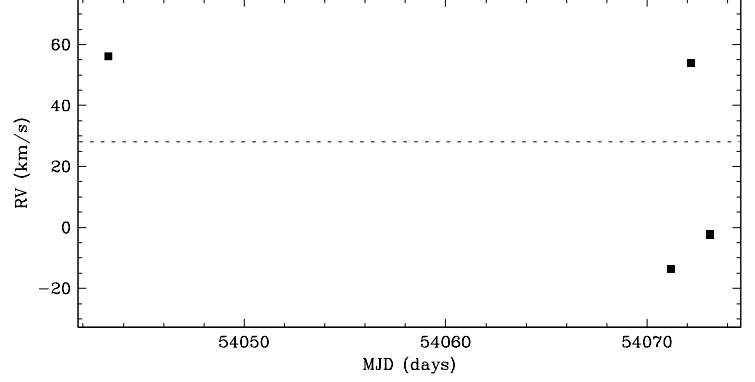


FIG. 21.— RX J0415.8+3100 is an SB1. The overall radial velocity scatter is significant relative to the measurement uncertainties. For epoch #4, the strong sharp peak in the broadening function at the observer's rest frame is due to moonlight, and may have biased the radial velocity estimate toward the observer's rest frame. This target has been previously reported by Kohler & Leinert (1998) to have a resolved companion with a separation of $\sim 0''.94$ (~ 130 AU) at a position angle of $\sim 147^\circ.2$, and an R -band flux ratio of ~ 0.19 (based on $\Delta K \sim 1.45$). Given the separation, the expected contribution to the broadening function from the resolved companion is small.

Region: Tau
 Object: RX J0457.5+2014
 RA Dec (J2000.0): 04 57 30.66 +20 14 29.7
 Spectral Type: K3

S/N @ H α : 30.8 ± 1.9
 H α 10% width: 0 km/s
 $v \sin i$: 33 ± 2.9 km/s
 EW CaI: Not available
 [3.6] – [8.0]: 0.05 ± 0.05

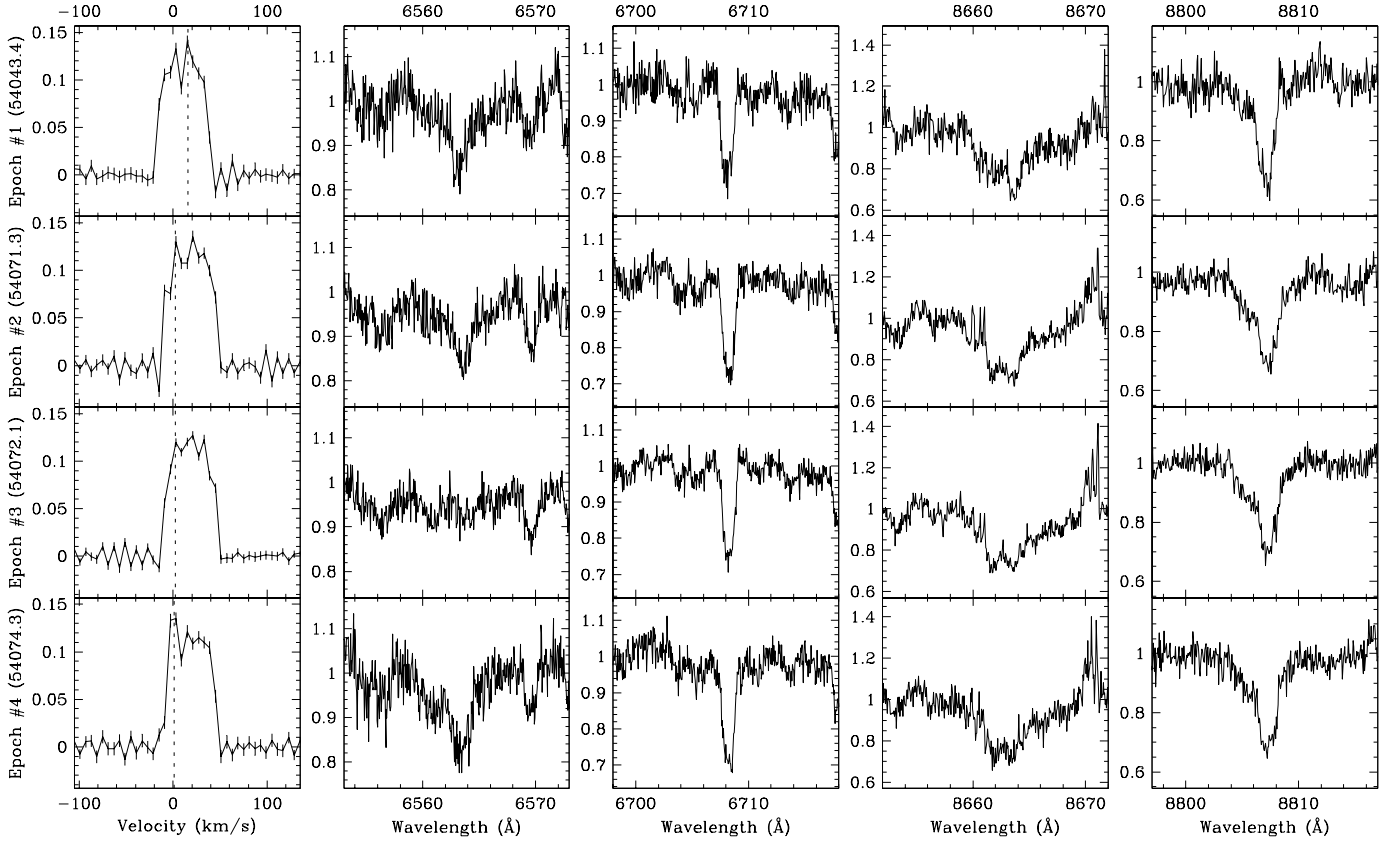
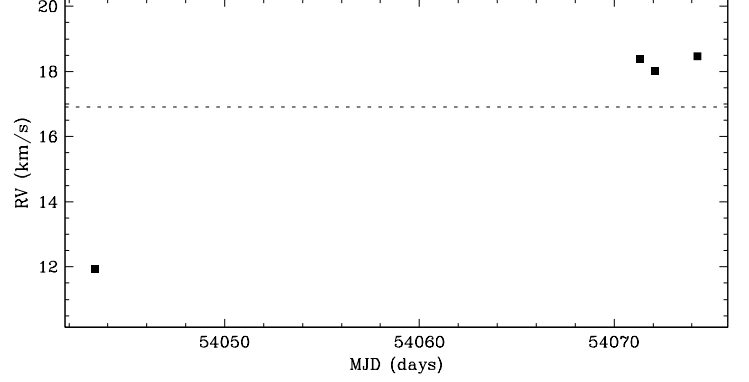


FIG. 22.— RX J0457.5+2014 is an SB1. The overall radial velocity scatter is significant relative to the measurement uncertainties and to scatter observed within each observing run. If star spots are responsible for the changes in radial velocity, based on observed $v \sin i$ ($\sim 33 \text{ km s}^{-1}$) and model stellar radius ($\sim 1.7 R_{\odot}$), one would expect variations on a maximum timescale of ~ 2.6 days. From the stable results of the second observing run (epochs #2, #3 and #4) which span 3.0 days, it is unlikely that the radial velocity trends are the result of star spots. For epoch #4, the sharp peak in the broadening function at the observer's rest frame is due to moonlight, and may have biased the radial velocity estimate toward the observer's rest frame. This target has been previously reported by Kohler & Leinert (1998) to have a resolved companion with a separation of $6''.865\text{--}6''.867$ (~ 960 AU) at a position angle of $204^{\circ}8\text{--}205^{\circ}5$, and an R -band flux ratio of $\lesssim 0.01$ (based on $\Delta K \sim 2.20\text{--}2.42$). Given the flux ratio and separation, the expected contribution to the broadening function from the resolved companion is negligible.

Region: Cha
 Object: CHXR 28 B
 RA Dec (J2000.0): 11 07 55.89 -77 27 25.8
 Spectral Type: G9

S/N @ H α : 8.4 ± 1.2
 H α 10% width: 175 km/s
 $v \sin i$: 61 ± 4.5 km/s
 EW CaII: Not available
 [3.6] – [8.0]: Not available

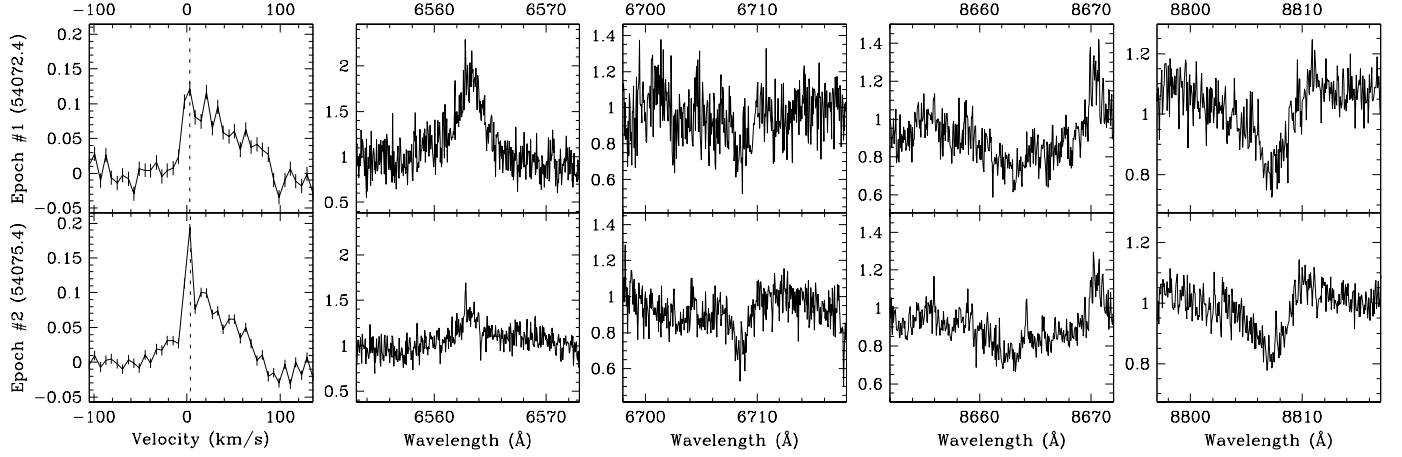
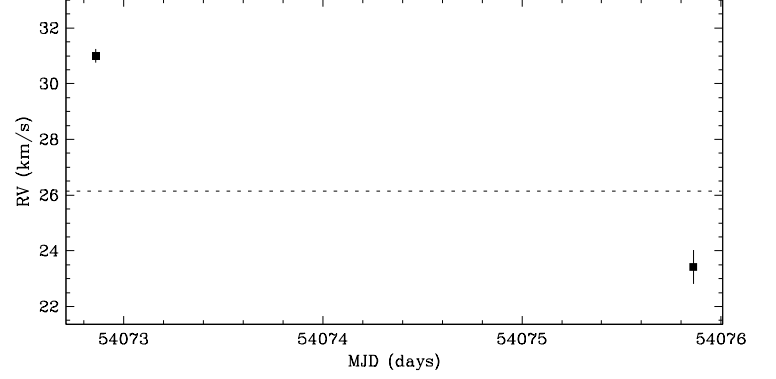


FIG. 23.— CHXR 28 B is a suspected SB1. The overall radial velocity scatter is larger than expected from non-companion influences, e.g., star spots. We derived the radial velocities from fits to the broadening function rather than from direct fits to the spectra (see §3.2). The strong sharp peaks in the broadening functions at the observer's rest frame are due to dawn twilight, and was included in the broadening function fits. This target has been previously reported by Lafrenière et al. (2008) to have a resolved companion with a separation of $\sim 1''.818$ (~ 250 AU) at a position angle of $\sim 115^\circ 9$, and an R -band flux ratio of ~ 0.68 (based on $\Delta K \sim 0.32$). Given the separation, the expected contribution to the broadening function from the resolved companion is negligible.

Region: Cha
 Object: T7
 RA Dec (J2000.0): 10 59 01.09 -77 22 40.7
 Spectral Type: K8

S/N @ H α : 13.0 ± 1.0
 H α 10% width: 365 ± 76 km/s
 $v \sin i$: 11 ± 0.8 km/s
 EW CaII: -1.60 ± 1.13 Å
 [3.6] – [8.0]: Not available

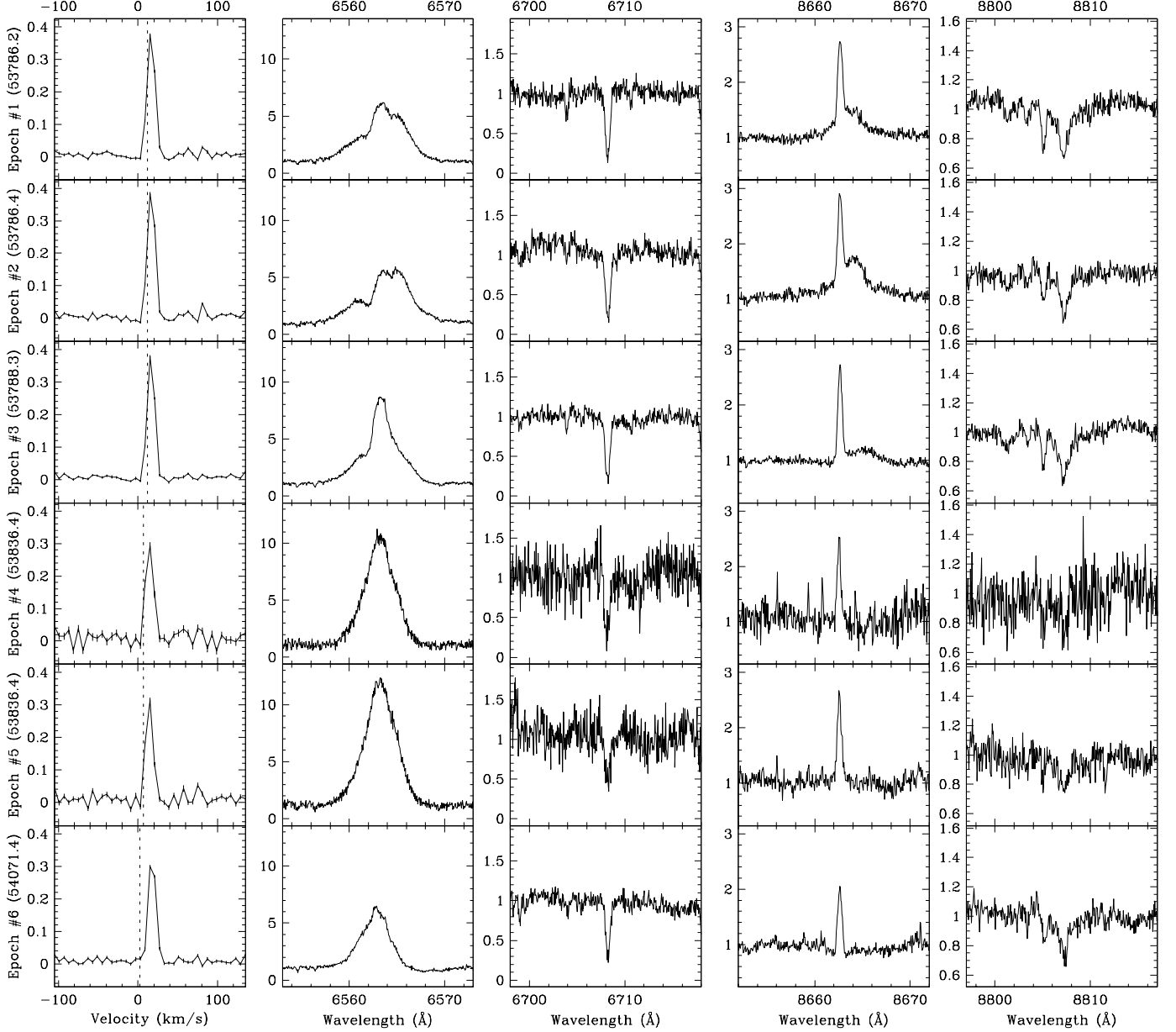
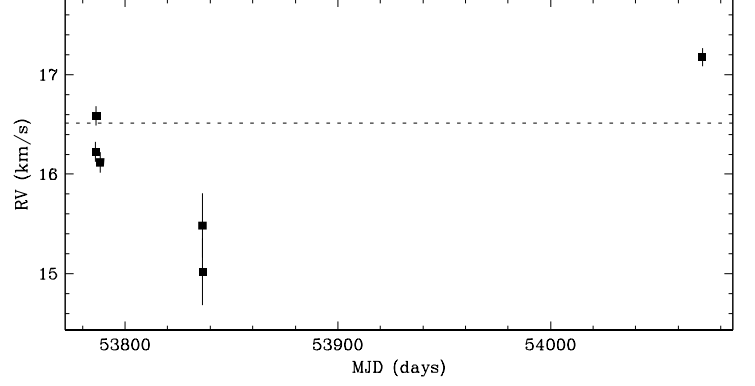


FIG. 24.— T7 is a suspected SB1. The overall radial velocity scatter is larger than expected from non-companion influences, e.g., star spots. If star spots are responsible for the changes in radial velocity, based on observed $v \sin i$ ($\sim 11 \text{ km s}^{-1}$) and model stellar radius ($\sim 1.4 R_{\odot}$), one would expect variations on a maximum timescale of ~ 6.1 days. From the stable results of the first observing run (epoch #1, #2 and #3) which spans 2.1 days, there is doubt that the radial velocity trends are the result of star spots. This target has been previously reported by Lafrenière et al. (2008) to have no resolved companions.

Region: Tau
 Object: CITau
 RA Dec (J2000.0): 04 33 52.00 +22 50 30.2
 Spectral Type: G

S/N @ H α : 23.1 ± 1.7
 H α 10% width: 572 ± 9 km/s
 $v \sin i$: 13 ± 2.5 km/s
 EW CaII: -23.42 ± 8.90 Å
 [3.6] – [8.0]: 1.63 ± 0.02

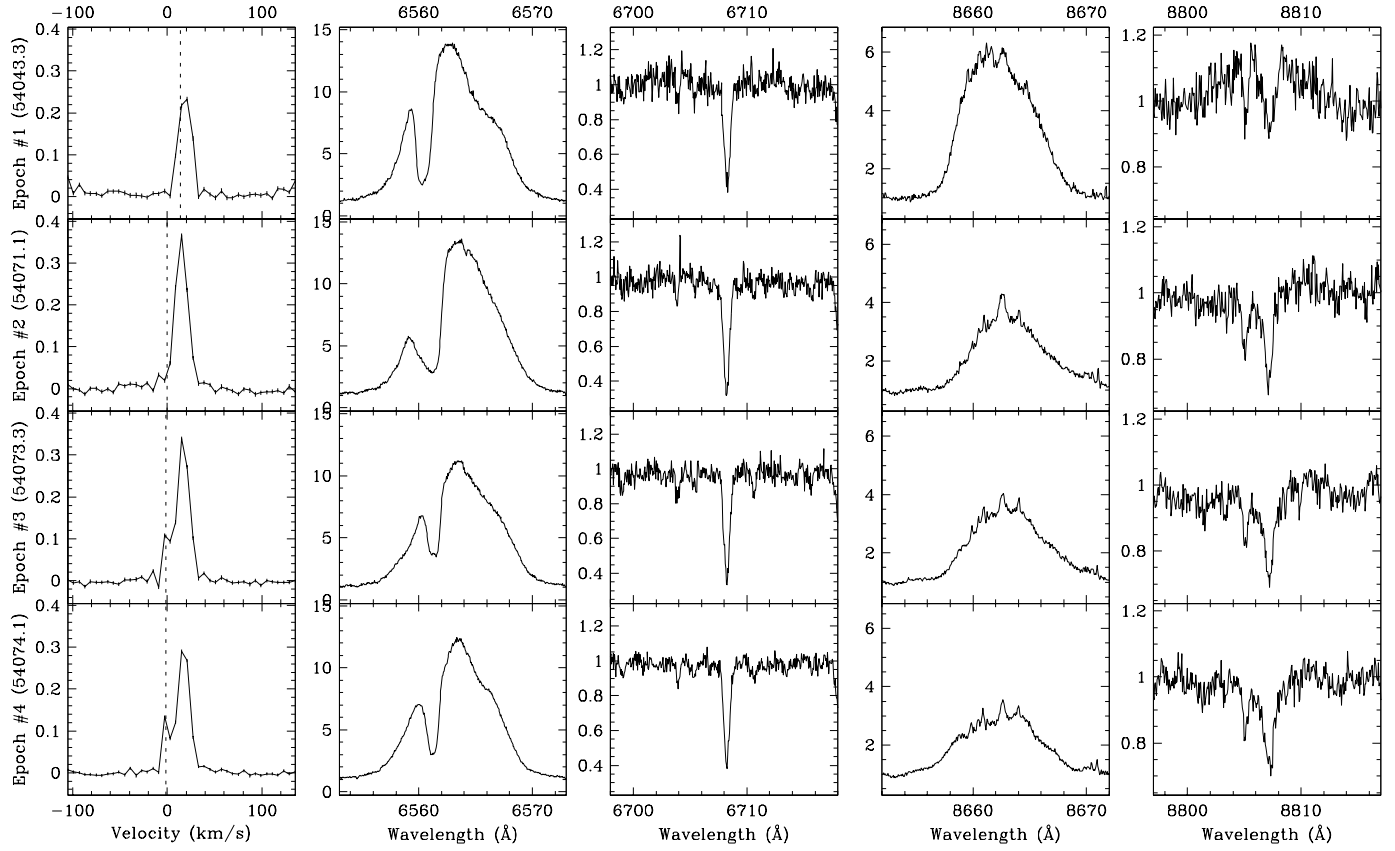
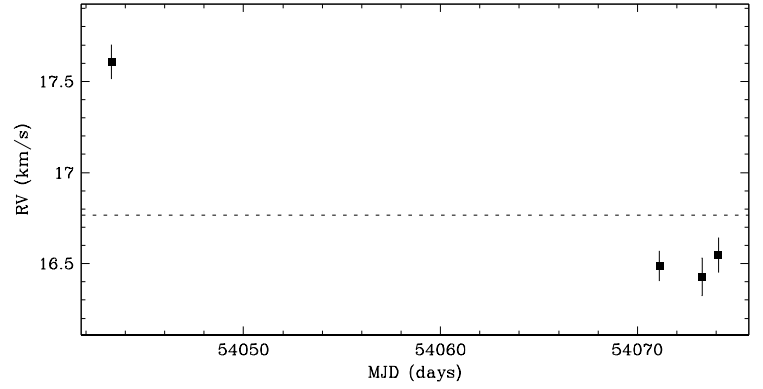


FIG. 25.— CITau is a suspected SB1. The overall radial velocity scatter is larger than expected from non-companion influences, e.g., star spots. If star spots were responsible for the changes in radial velocity, based on observed $v \sin i$ ($\sim 13 \text{ km s}^{-1}$) and model stellar radius ($\sim 4.0 R_{\odot}$), one would expect variations on a maximum timescale of ~ 15.5 days. From the stable results of the second observing run (epochs #2, #3 and #4) which span 3.0 days, it is unlikely that the radial velocity trends are the result of star spots. For epoch #3 and #4, the peaks in the broadening function at the observer's rest frame are due to moonlight, and may have biased the radial velocity estimates toward the observer's rest frame. This target has been previously reported by Leinert et al. (1993), Ghez et al. (1993), and Simon et al. (1995) to have no resolved companions.

Region: Tau
 Object: RY Tau
 RA Dec (J2000.0): 04 21 57.40 +28 26 35.5
 Spectral Type: F8

S/N @ H α : 58.5 ± 3.5
 H α 10% width: 600 ± 24 km/s
 $v \sin i$: 48 ± 2.6 km/s
 EW CaI: -0.80 ± 1.07 Å
 [3.6] - [8.0]: 2.47 ± 0.01

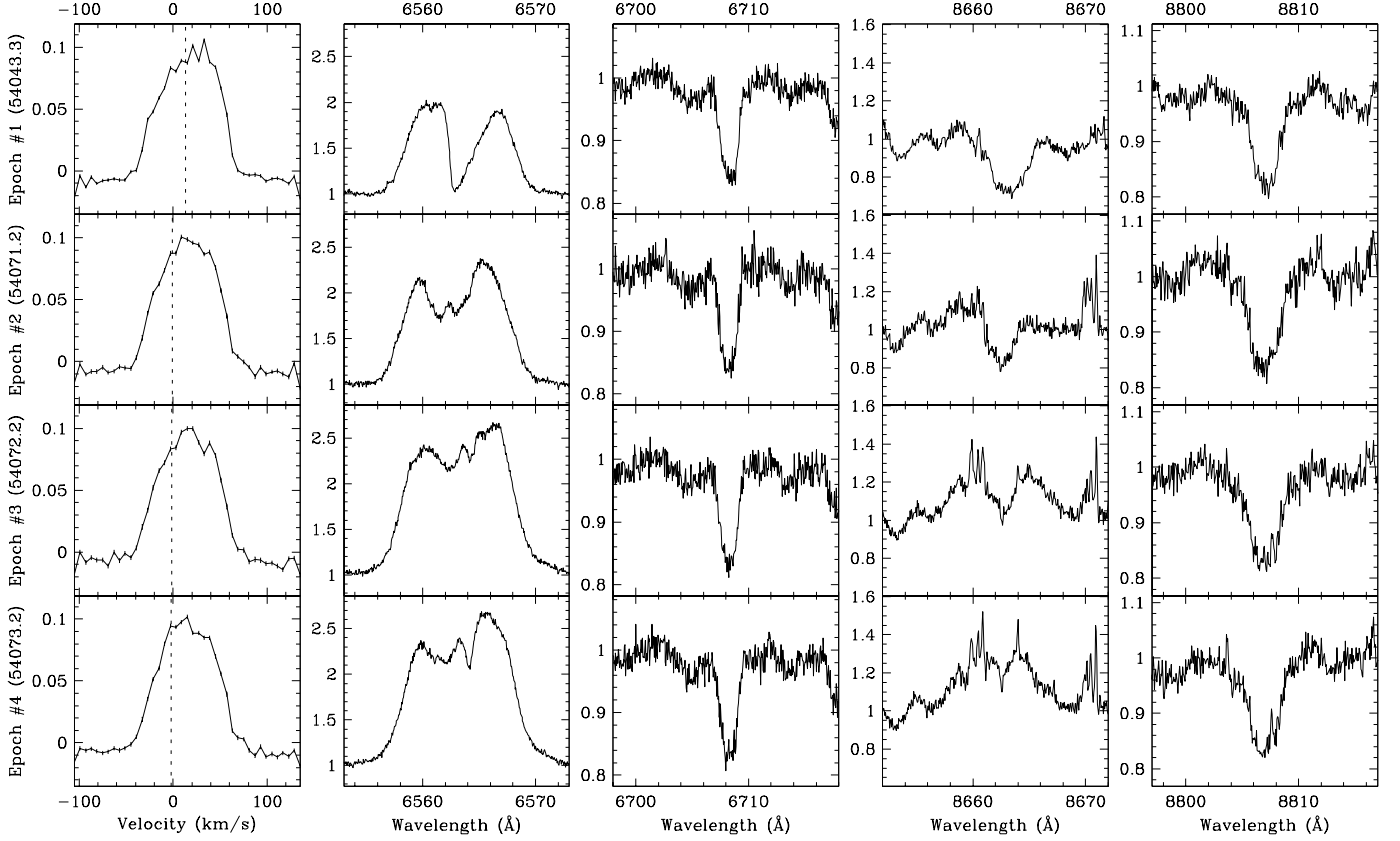
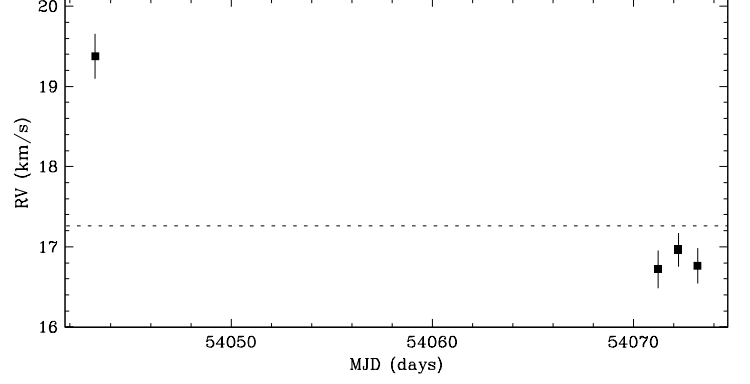


FIG. 26.— RY Tau is a suspected SB1. The overall radial velocity scatter is larger than expected from non-companion influences, e.g., star spots. If star spots are responsible for the changes in radial velocity, based on observed $v \sin i$ ($\sim 48 \text{ km s}^{-1}$) and model stellar radius ($\sim 4.6 R_{\odot}$), one would expect variations on a maximum timescale of ~ 4.9 days. From the stable results of the second observing run (epochs #2, #3 and #4) which span 2.0 days, it is unlikely that the radial velocity trends are the result of star spots. This target has been previously reported by Leinert et al. (1993), and Ghez et al. (1993) to have no resolved companions.

Region: Cha
 Object: CHXR 47
 RA Dec (J2000.0): 11 10 38.02 $-77^{\circ} 32' 39.9''$
 Spectral Type: K3

S/N @ H α : 25.9 ± 2.4
 H α 10% width: 0 km/s
 $v \sin i$: See caption
 EW CaII: Not available
 [3.6] – [8.0]: 1.40 ± 0.02

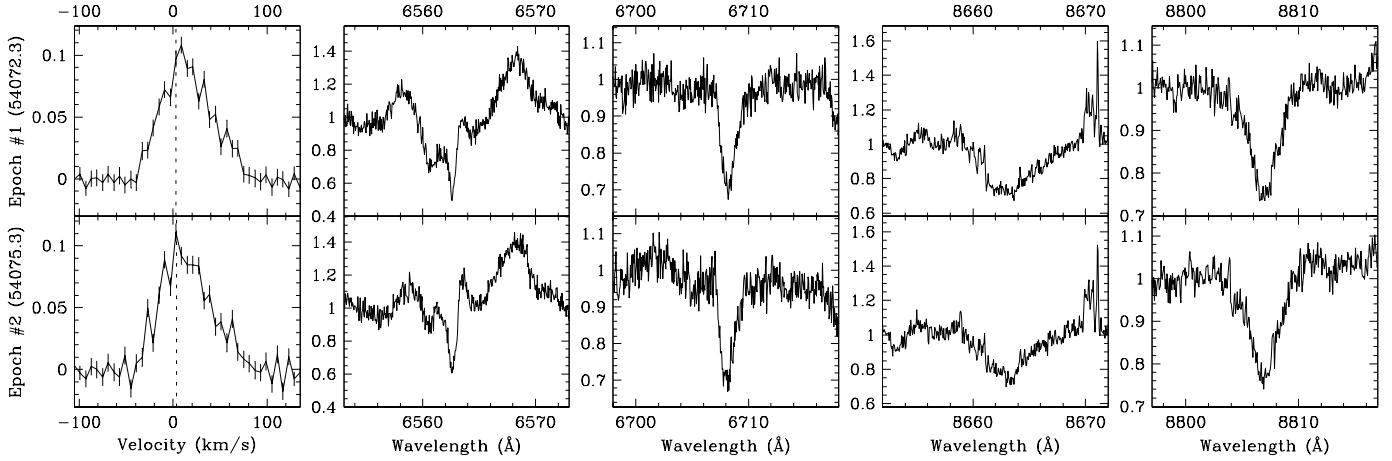
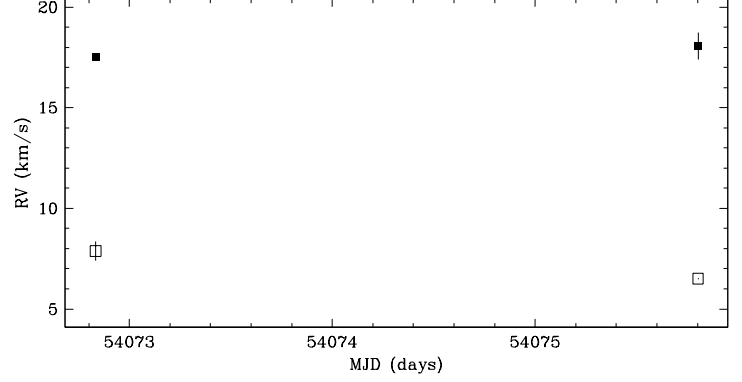


FIG. 27.— CHXR 47 is a long-period SB2. By fitting the broadening function to two rotational broadening line profiles, we estimate the two sources have a flux ratio of 0.24 ± 0.06 , and the A and B sources have $v \sin i$ of $59.5 \pm 0.4 \text{ km s}^{-1}$ and $24 \pm 3 \text{ km s}^{-1}$, respectively. However, these results and the derived radial velocities should be read with caution because of the broad and blended peaks in the broadening functions of this system which are difficult to decompose and fit reliably. This target has been previously reported by Lafrenière et al. (2008) to have a resolved companion with a separation of $\sim 0''.175$ ($\sim 25 \text{ AU}$) at a position angle of $\sim 334^\circ$, and an R -band flux ratio of ~ 0.49 (based on $\Delta K \sim 0.47$). This flux ratio is comparable to that estimated between the SB2 components. Furthermore, the resolved companion has an expected circular orbital speed of $\sim 7 \text{ km s}^{-1}$ which is compatible with the estimated radial velocity separations of the SB2 component stars. Therefore, the resolved companion is likely the SB2 secondary star.

Region: Cha
 Object: T21
 RA Dec (J2000.0): 11 06 15.41 $-77^{\circ} 21' 56.8''$
 Spectral Type: G5

S/N @ H α : 37.1 ± 4.4
 H α 10% width: 0 km/s
 $v \sin i$: See caption
 EW CaII: -0.01 \AA
 [3.6] – [8.0]: Not available

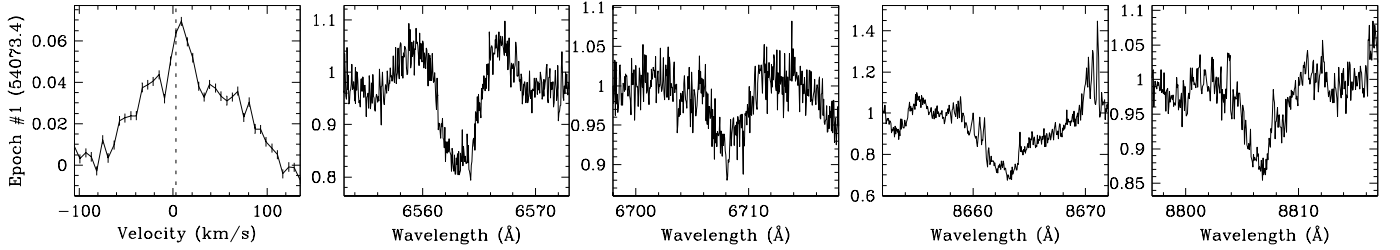
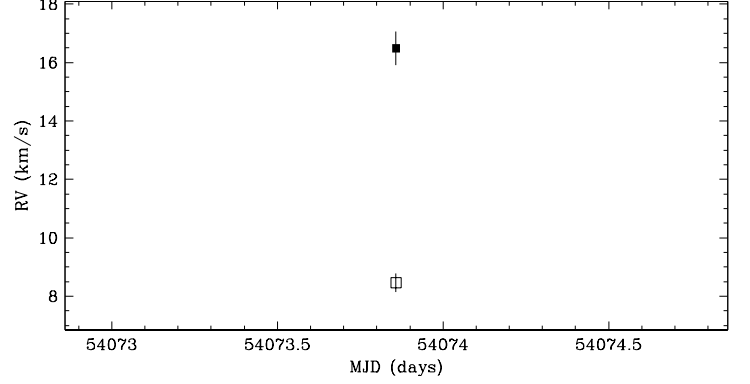


FIG. 28.— T21 is a long-period SB2. Two sources can be seen in the broadening function: a strong peak and a shallower broad feature. By fitting the broadening function to two rotational broadening line profiles, we estimate the two sources have a flux ratio of 0.101 ± 0.005 , and the A and B sources have $v \sin i$ of $94.1 \pm 0.7 \text{ km s}^{-1}$ and $14.5 \pm 0.3 \text{ km s}^{-1}$, respectively. This target has been previously reported by Lafrenière et al. (2008) to have a resolved companion with a separation of $\sim 0''.14$ ($\sim 20 \text{ AU}$) at a position angle of $\sim 126^\circ$, and an R -band flux ratio of ~ 0.08 (based on $\Delta K \sim 2.16$). This flux ratio is similar to that estimated between the SB2 components. Furthermore, the resolved companion has an expected circular orbital speed of $\sim 13 \text{ km s}^{-1}$ which is compatible with the radial velocity separations of the SB2 components star if we consider the large uncertainties due to rapid rotation. Therefore, the resolved companion is likely the SB2 secondary star.

Region: Tau
 Object: DF Tau
 RA Dec (J2000.0): 04 27 02.80 +25 42 22.3
 Spectral Type: M3

S/N @ H α : 28.9 ± 1.8
 H α 10% width: 369 ± 19 km/s
 $v \sin i$: See caption
 EW CaII: -1.51 ± 0.87 Å
 [3.6] - [8.0]: 1.37 ± 0.01

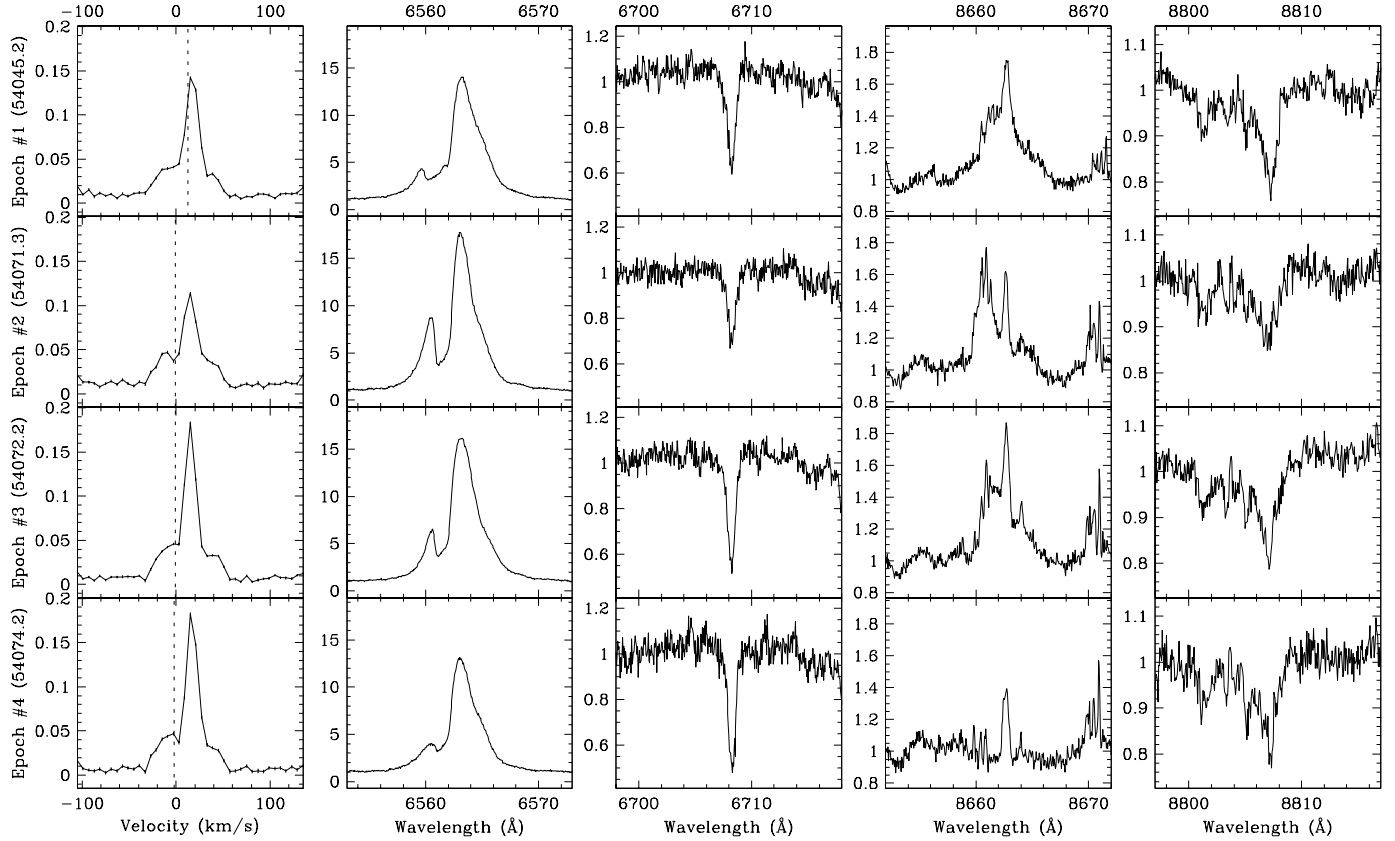
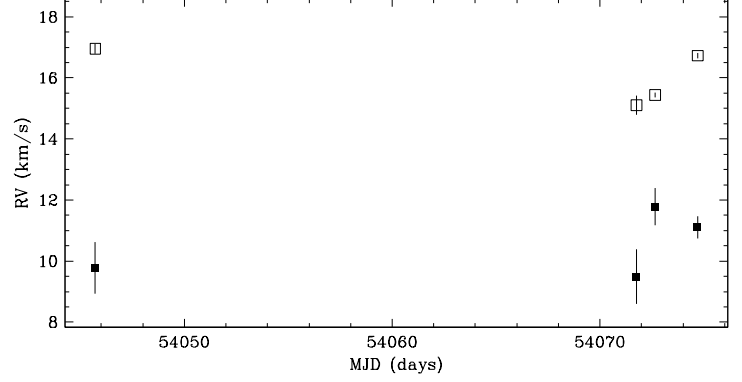


FIG. 29.— DF Tau is a long-period SB2. Two sources can be seen in the broadening function: a strong peak and a shallower broad feature. By fitting the broadening function to two rotational broadening line profiles, we estimate the two sources have a flux ratio of 0.49 ± 0.11 , and the A and B sources have $v \sin i$ of 46.6 ± 1.8 km s $^{-1}$ and 9.8 ± 0.6 km s $^{-1}$, respectively. This target has been previously reported by Ghez et al. (1993), Simon et al. (1995), and Ghez et al. (1997b) as a resolved binary (DF Tau A+B) with a separation of $0''.0871$ – $0''.088$ (~ 12 AU) at a position angle of 301° – 329° , and an R -band flux ratio of 0.05 – 0.24 (based on $\Delta K \sim 0.41$ – 0.90). This flux ratio is comparable to that estimated between the SB2 components with we consider the uncertainties in the models. Furthermore, the resolved secondary star has an expected circular orbital speed of ~ 5 km s $^{-1}$ which is consistent with the radial velocity separations of the SB2 component stars. Therefore, the resolved secondary star is likely the SB2 secondary star.

Region: Tau
 Object: HD285281
 RA Dec (J2000.0): 04 00 31.07 +19 35 20.7
 Spectral Type: K0

S/N @ H α : 48.4 ± 2.9
 H α 10% width: 0 km/s
 $v \sin i$: See caption
 EW CaI: Not available
 [3.6] – [8.0]: Not available

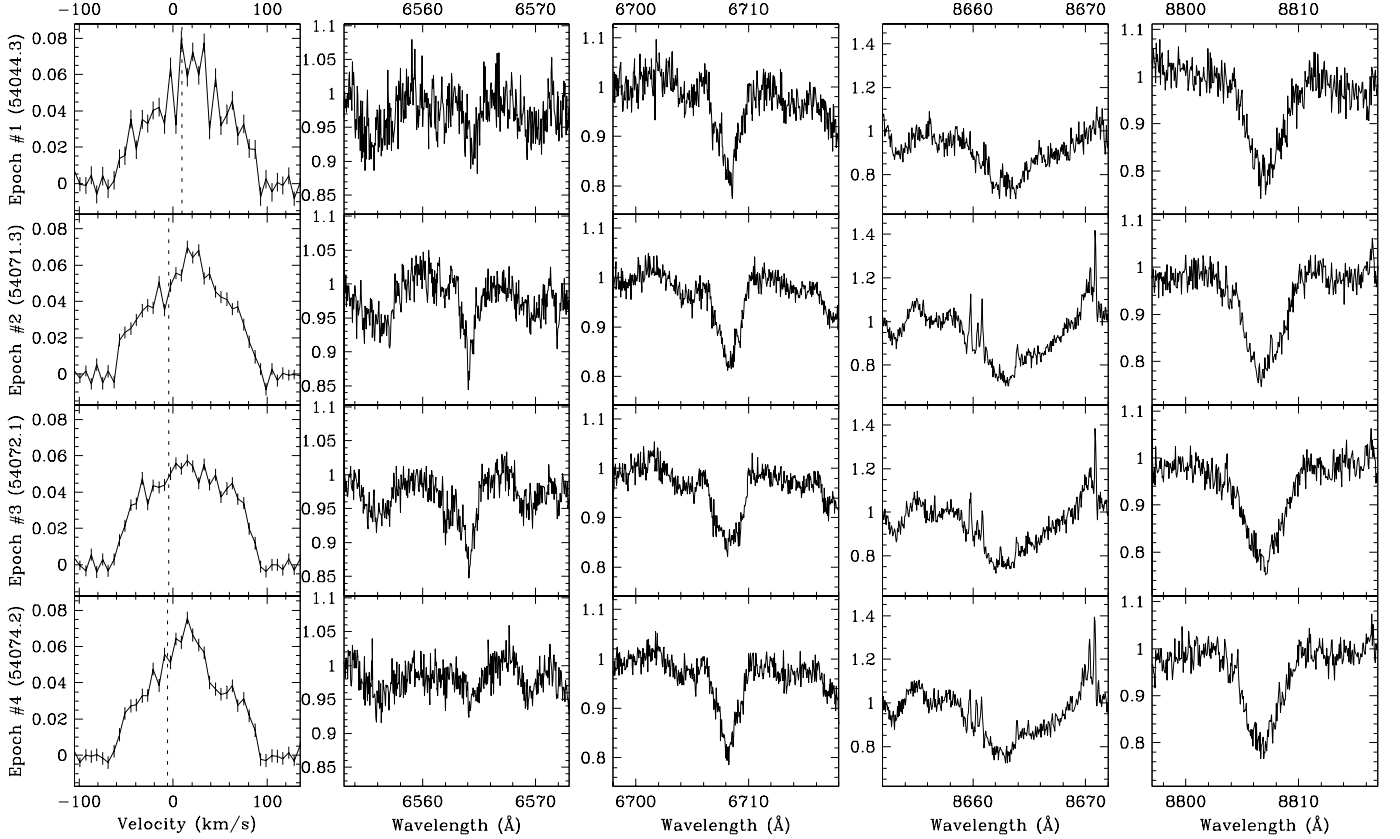
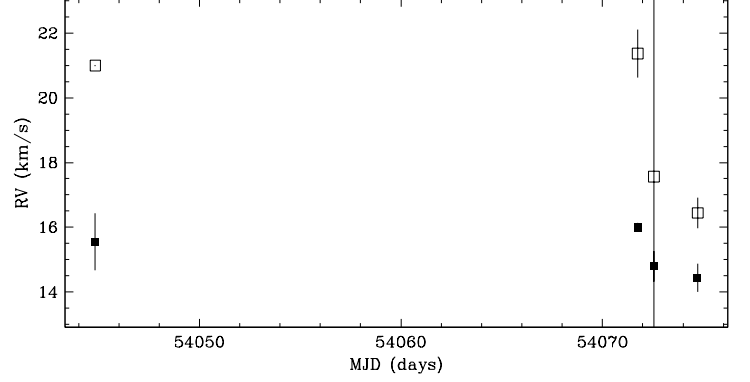


FIG. 30.— HD285281 is a long-period SB2. Two sources can be seen in the profile: a peak (at $\sim 20 \text{ km s}^{-1}$) on top of a broad feature. By fitting the broadening function to two rotational broadening line profiles, we estimate the two sources have a flux ratio of 0.07 ± 0.05 , and the A and B sources have $v \sin i$ of $78.0 \pm 0.3 \text{ km s}^{-1}$ and $17.0 \pm 1.9 \text{ km s}^{-1}$, respectively. The radial velocity estimates for epoch #3 are inaccurate because the fitting routine could not delineate the two individual profiles. This target has been previously reported by Kohler & Leinert (1998) to have a resolved companion with a separation of $\sim 0''.773$ ($\sim 110 \text{ AU}$) at a position angle of $\sim 190^\circ$, and an R -band flux ratio of ~ 0.21 (based on $\Delta K \sim 1.23$). This flux ratio is comparable to that estimated between the SB2 components. Furthermore, the resolved companion has an expected circular orbital speed of $\sim 5 \text{ km s}^{-1}$ which is consistent with the radial velocity separations of the SB2 component stars. Therefore, the resolved companion is likely the SB2 secondary star.

Region: Tau
 Object: RX J0406.8+2541 A
 RA Dec (J2000.0): 04 06 51.35 +25 41 28.3
 Spectral Type: K4.5

S/N @ H α : 23.4 ± 2.2
 H α 10% width: 277 ± 74 km/s
 $v \sin i$: See caption
 EW CaI: Not available
 [3.6] – [8.0]: Not available

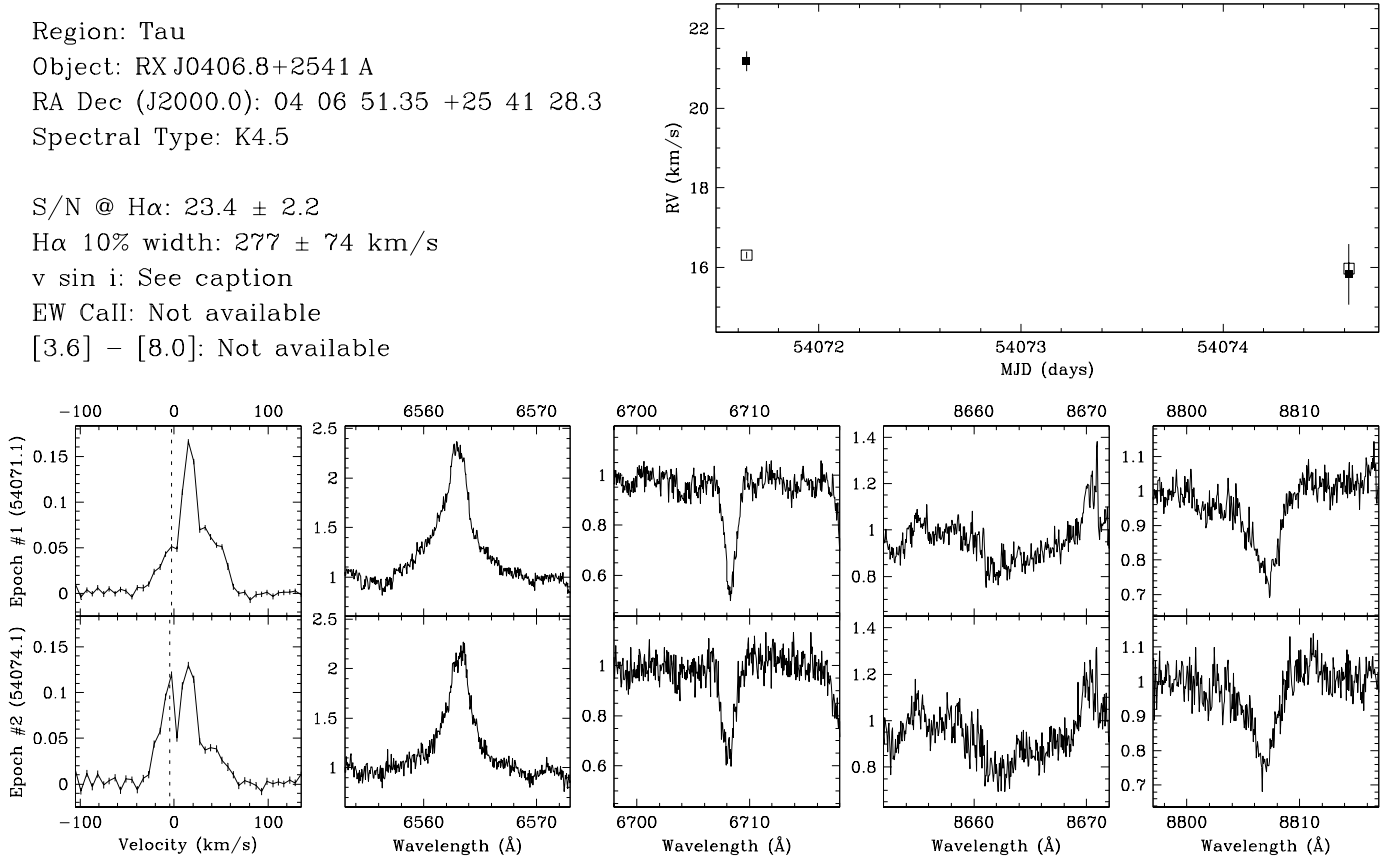


FIG. 31.— RX J0406.8+2541 A is a long-period SB2. Two sources can be seen in the broadening function: a strong peak and a shallower broad feature. By fitting the broadening function to two rotational broadening line profiles, we estimate the two sources have a flux ratio of 0.32 ± 0.07 , and the a and b sources have $v \sin i$ of 47 ± 4 km s $^{-1}$ and 9.8 ± 0.3 km s $^{-1}$, respectively. For epoch #2, the strong peak in the broadening function at the observer's rest frame is due to moonlight, and biased the radial velocity estimates in the fits. This target has been previously reported by Kohler & Leinert (1998) to have a resolved companion (RX J0406.8+2541 B) with a separation of $\sim 0''.977$ (~ 140 AU) at a position angle of $\sim 12^\circ 3$, and an R -band flux ratio of ~ 0.95 (based on $\Delta K \sim 0.04$). This flux ratio is comparable to that estimated between the SB2 components if one accounts for the diminished light from the companion at that distance from the slit. Furthermore, the resolved companion has an expected circular orbital speed of ~ 3 km s $^{-1}$ which is similar to the radial velocity separations of the SB2 component stars. Furthermore, the radial velocity estimates of the SB2 secondary star is consistent with that of RX J0406.8+2541 B. Therefore, the resolved companion is likely the SB2 secondary star.

Region: Tau
 Object: RX J0441.4+2715
 RA Dec (J2000.0): 04 41 24.00 +27 15 12.4
 Spectral Type: G8

S/N @ H α : 22.3 ± 1.5
 H α 10% width: 0 km/s
 $v \sin i$: See caption
 EW CaII: Not available
 [3.6] – [8.0]: Not available

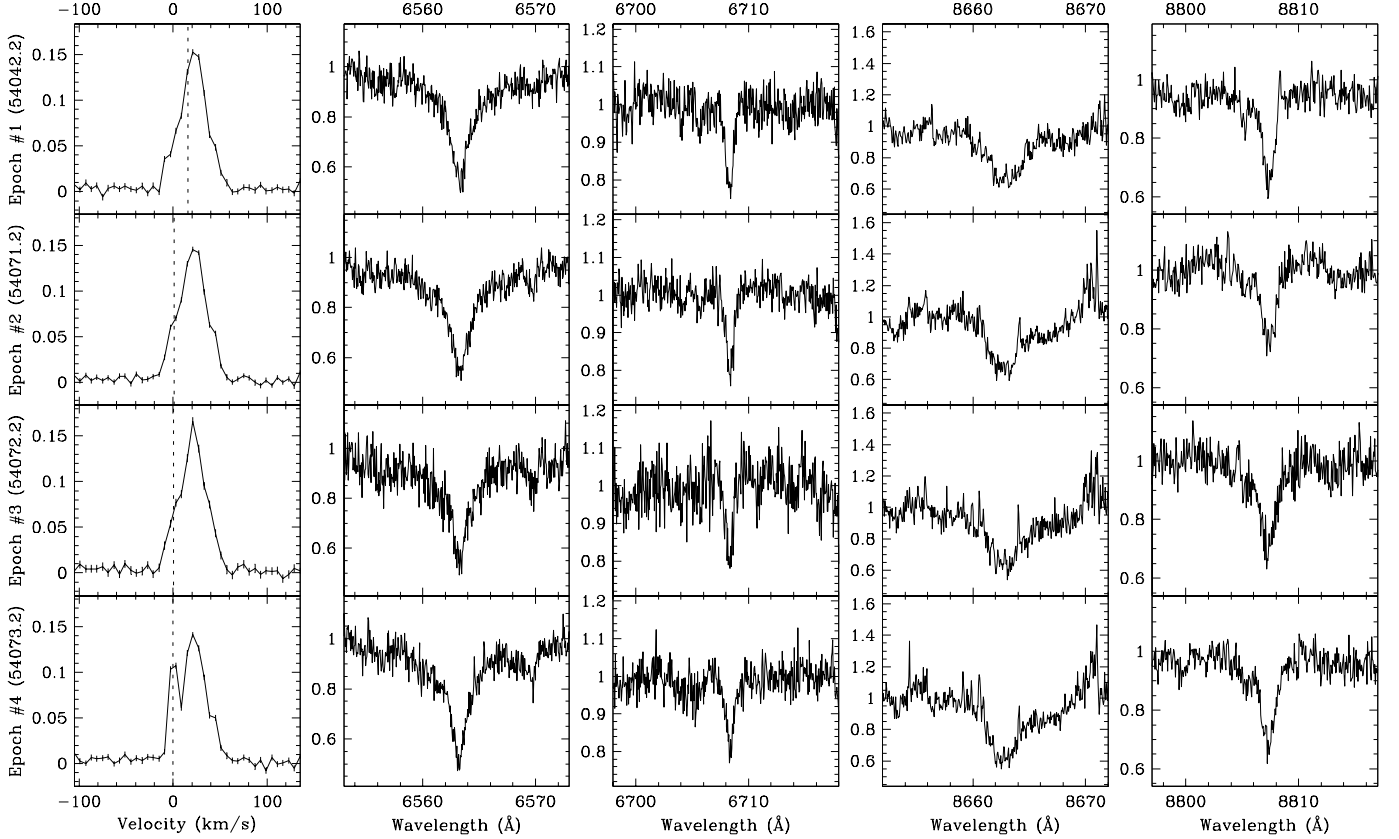
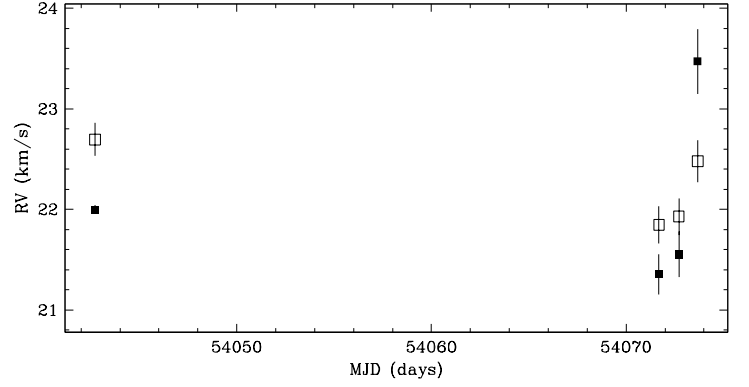


FIG. 32.— RX J0441.4+2715 is a long-period SB2. Two sources can be seen in the broadening function: a strong peak and a shallower broad feature. By fitting the broadening function to two rotational broadening line profiles, we estimate the two sources have a flux ratio of 0.32 ± 0.07 , and the A and B sources have $v \sin i$ of $37.0 \pm 0.6 \text{ km s}^{-1}$ and $12.6 \pm 1.5 \text{ km s}^{-1}$, respectively. The overall radial velocity deviates from that of the star-forming region. However, cluster membership is supported by Li- λ 6708 absorption. For epoch #4, the sharp peak in the broadening function at the observer's rest frame is due to moonlight, and biased the radial velocity estimates in the fits. This target has been previously reported by Kohler & Leinert (1998) to have a resolved companion with a separation of $\sim 0''.065$ ($\sim 9.1 \text{ AU}$) at a position angle of $\sim 216^\circ$, and an R -band flux ratio of ~ 0.49 (based on $\Delta K \sim 0.63$). This flux ratio is comparable to that estimated between the SB2 components. Furthermore, the resolved companion has an expected circular orbital speed of $\sim 21 \text{ km s}^{-1}$ which is consistent with the radial velocity separations of the SB2 component stars. Therefore, the resolved companion is likely the SB2 secondary star.

Region: Tau
 Object: RX J0443.4+1546
 RA Dec (J2000.0): 04 43 25.97 +15 46 03.9
 Spectral Type: G7

S/N @ H α : 21.4 ± 1.6
 H α 10% width: 0 km/s
 $v \sin i$: See caption
 EW CaI: Not available
 [3.6] – [8.0]: Not available

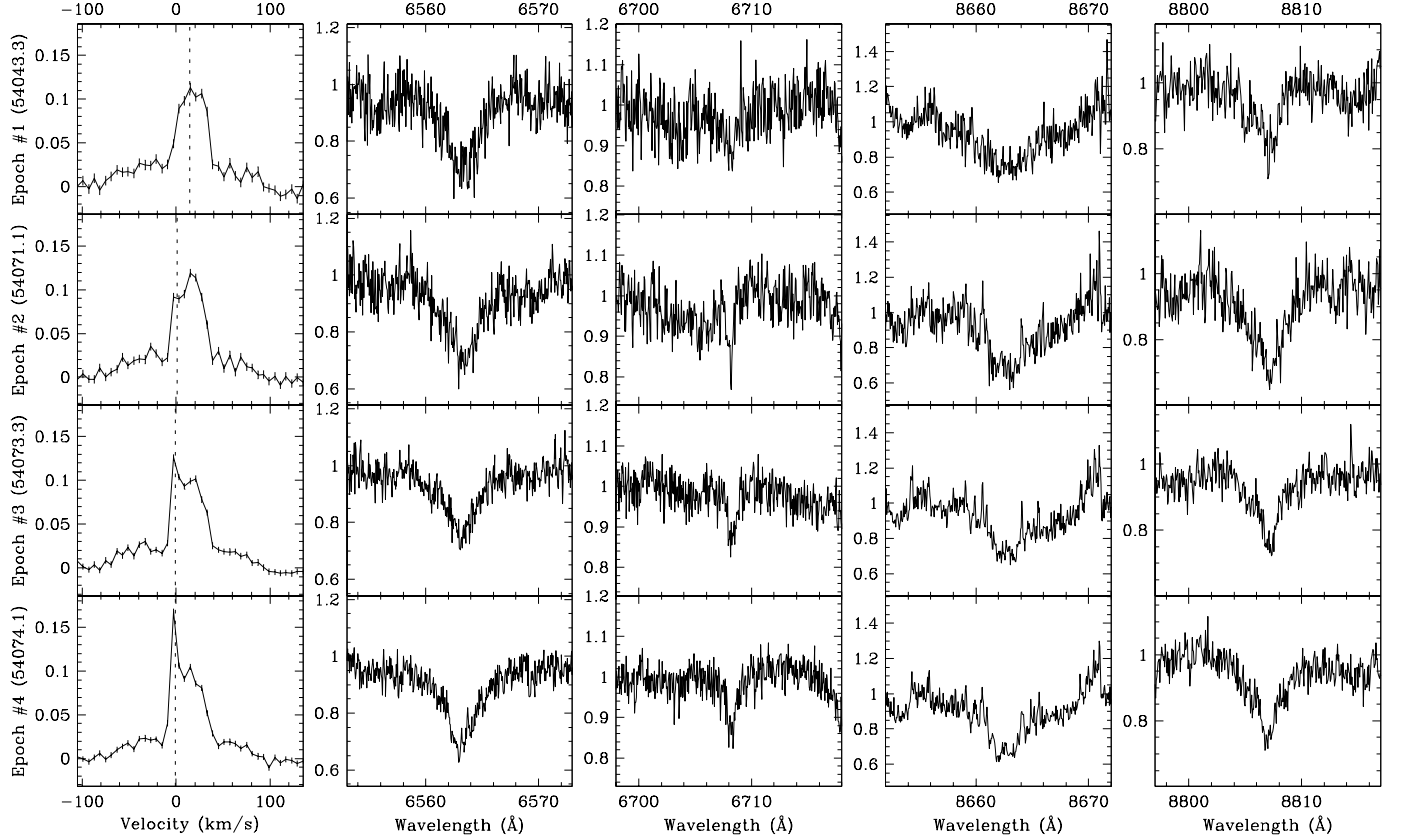
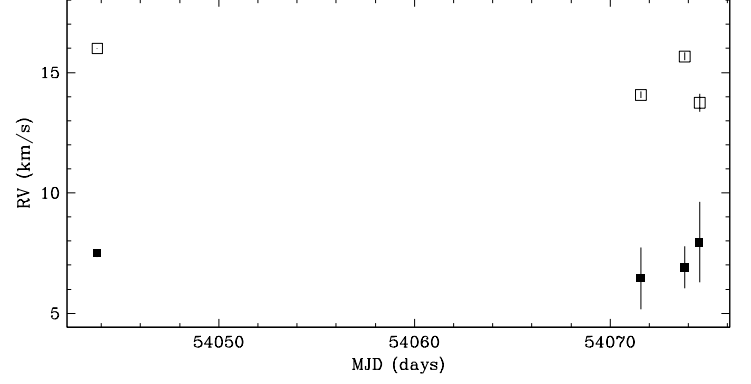


FIG. 33.— RX J0443.4+1546 is a long-period SB2. Two sources can be seen in the broadening function: a strong peak and a shallower broad feature. By fitting the broadening function to two rotational broadening line profiles, we estimate the two sources have a flux ratio of 0.83 ± 0.10 , and the A and B sources have $v \sin i$ of $86.5 \pm 1.6 \text{ km s}^{-1}$ and $24.0 \pm 0.8 \text{ km s}^{-1}$, respectively. For epochs #3 and #4, the peaks in the broadening function at the observer's rest frame are due to moonlight, and have been accounted for in the radial velocity estimates. This target has been previously reported by Kohler & Leinert (1998) to have no resolved companions.

Region: Tau
 Object: RX J0455.7+1742
 RA Dec (J2000.0): 04 55 47.67 +17 42 02.0
 Spectral Type: K3

S/N @ H α : 30.4 ± 2.0
 H α 10% width: 0 km/s
 $v \sin i$: See caption
 EW CaII: $-0.13 \pm 0.01 \text{ \AA}$
 [3.6] – [8.0]: Not available

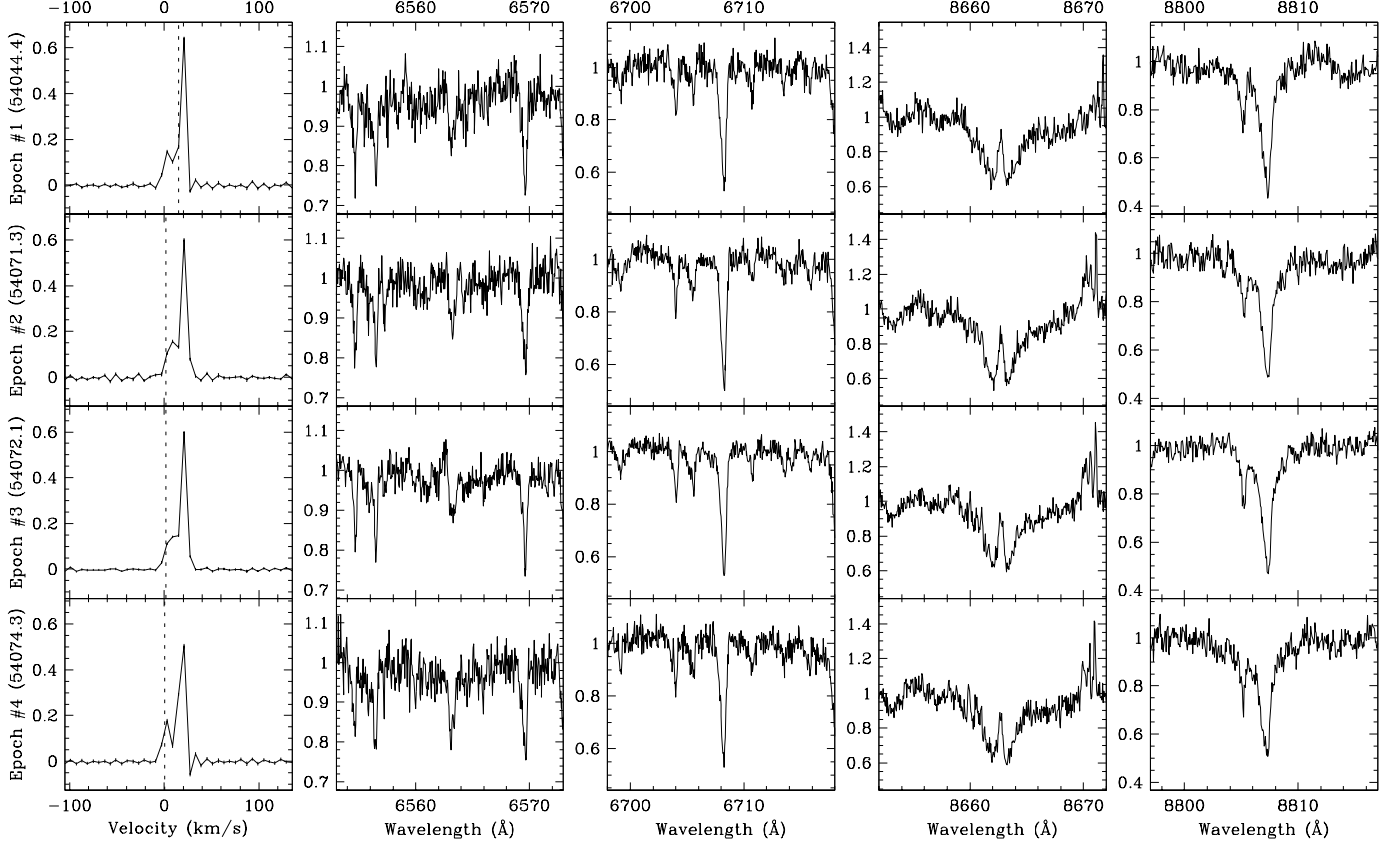
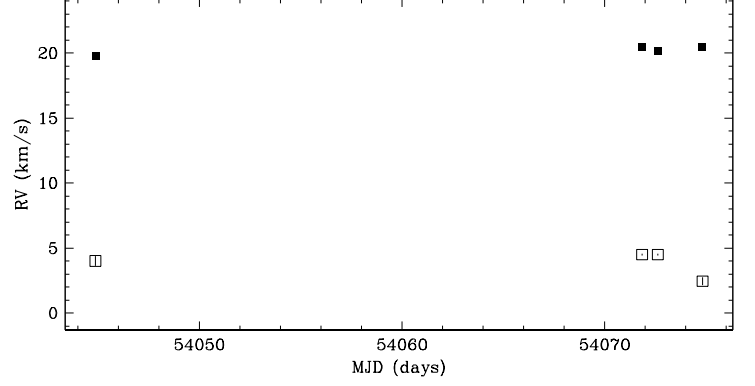


FIG. 34.— RX J0455.7+1742 is a long-period SB2. By fitting the broadening function to two rotational broadening line profiles, we estimate the two sources have a flux ratio of 0.337 ± 0.014 , and the A and B sources have $v \sin i$ of $8 \pm 2 \text{ km s}^{-1}$ and $9.5 \pm 0.4 \text{ km s}^{-1}$, respectively. For epoch #4, the small peak in the broadening function at the observer's rest frame has contribution from moonlight, and may have biased the radial velocity estimate toward the observer's rest frame. This target has been previously reported by Kohler & Leinert (1998) to have a resolved companion with a separation of $\sim 0''.093$ ($\sim 13 \text{ AU}$) at a position angle of $\sim 254^\circ$, and an R -band flux ratio of ~ 0.53 (based on $\Delta K \sim 0.41$). This flux ratio is similar to that estimated between the SB2 components. Furthermore, the resolved companion has an expected circular orbital speed of $\sim 11 \text{ km s}^{-1}$ which is comparable with the radial velocity separation of the SB2 component stars if we consider the large uncertainties due to rapid rotation. Therefore, the resolved companion is likely the SB2 secondary star.

Region: Cha
 Object: Hn 4
 RA Dec (J2000.0): 11 05 14.67 -77 11 29.1
 Spectral Type: M3.25

S/N @ H α : 4.5 ± 0.9
 H α 10% width: 176 ± 126 km/s
 $v \sin i$: See caption
 EW CaII: -0.28 ± 0.26 Å
 [3.6] – [8.0]: Not available

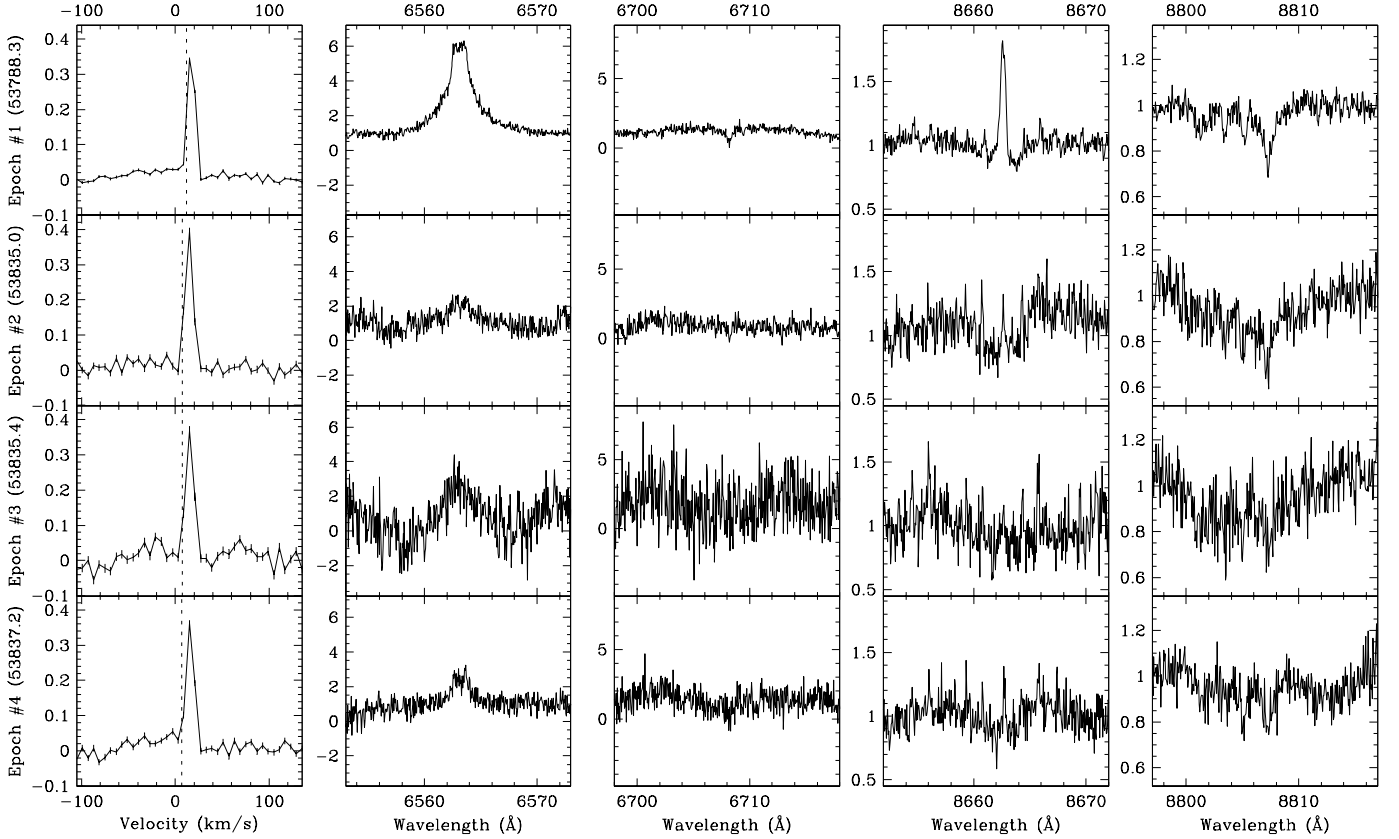
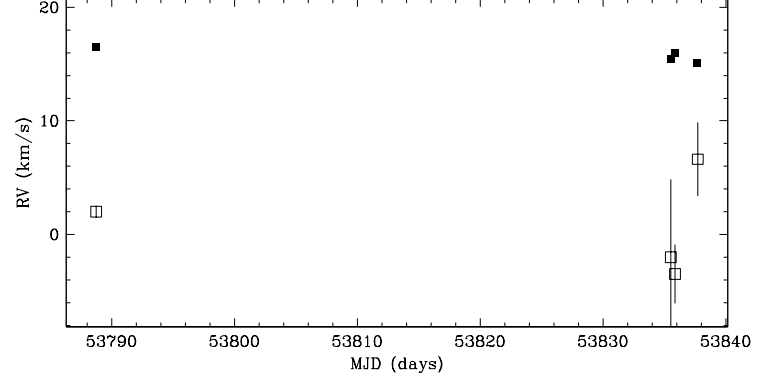


FIG. 35.— Hn 4 is a suspected SB2. Two sources are hinted at in the broadening function: a strong peak and a very shallow broad feature. By fitting the broadening function to two rotational broadening line profiles, we estimate the two sources have a flux ratio of 0.62 ± 0.09 , and the A and B sources have $v \sin i$ of 9.0 ± 0.5 km s $^{-1}$ and 90 ± 15 km s $^{-1}$, respectively. This target has been previously reported by Lafrenière et al. (2008) to have a resolved companion with a separation of $\sim 0''.211$ (~ 30 AU) at a position angle of $\sim 296^\circ$, and an R -band flux ratio of ~ 0.89 (based on $\Delta K \sim 0.04$). This flux ratio is similar to that estimated between the SB2 components. Furthermore, the resolved companion has an expected circular orbital speed of ~ 4 km s $^{-1}$ which is compatible with the radial velocity separations of the SB2 components star if we consider the large uncertainties due to rapid rotation. Therefore, the resolved companion is likely the SB2 secondary star.

Region: Cha
 Object: T11
 RA Dec (J2000.0): 11 02 24.91 -77 33 35.7
 Spectral Type: K6

S/N @ H α : 32.5 ± 2.4
 H α 10% width: 367 ± 38 km/s
 $v \sin i$: See caption
 EW CaII: -0.32 ± 0.01 Å
 [3.6] – [8.0]: Not available

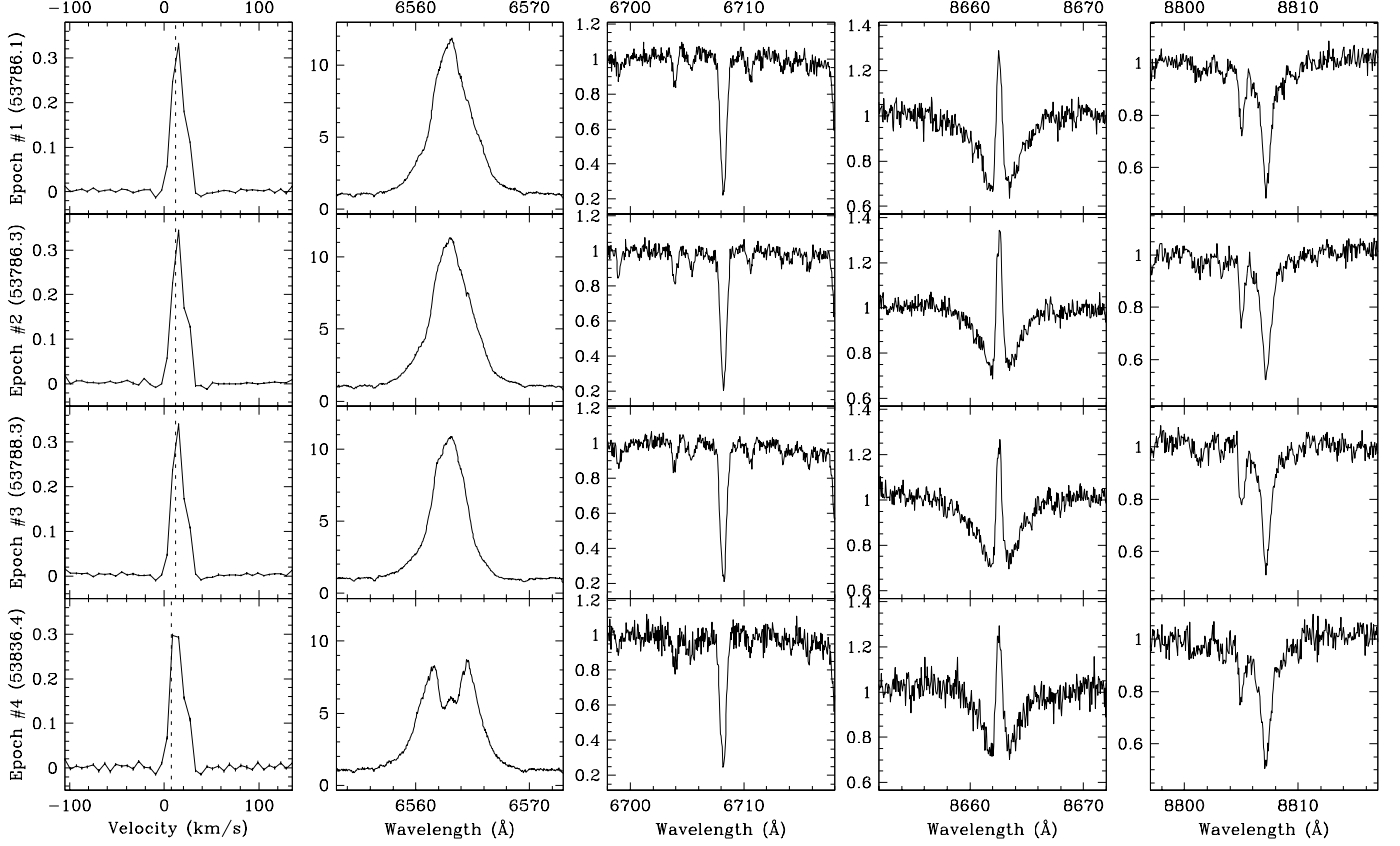
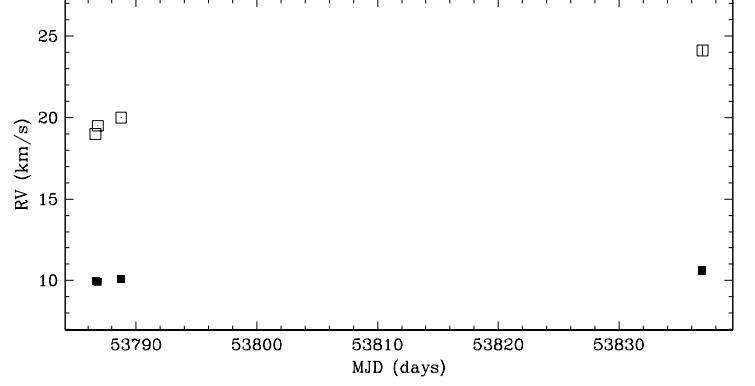


FIG. 36.— T11 is a suspected SB2. The broadening function is unusually asymmetrical, and has both a strong peak and a shallower slightly broader feature. If star spots are responsible for the asymmetries in the broadening function, based on observed $v \sin i$ (~ 14 km s $^{-1}$) and model stellar radius ($\sim 1.4 R_{\odot}$), one would expect variations on a maximum timescale of ~ 5.1 days. From the constant broadening functions of the first observing run (epochs #1, #2 and #3) which span 2.2 days, it is unlikely that the broadening function irregularities are the result of star spots. By fitting the broadening function to two rotational broadening line profiles, we estimate the two sources have a flux ratio of 1.0 ± 0.4 , and the A and B sources have $v \sin i$ of 11.2 ± 0.3 km s $^{-1}$ and 13.0 ± 0.3 km s $^{-1}$, respectively. This target has been previously reported by Lafrenière et al. (2008) to have no resolved companions.

Region: Tau
 Object: Hubble 4
 RA Dec (J2000.0): 04 18 47.04 +28 20 07.3
 Spectral Type: K7

S/N @ H α : 20.2 ± 1.4
 H α 10% width: 188 ± 16 km/s
 $v \sin i$: See caption
 EW CaII: -0.22 ± 0.02 Å
 [3.6] - [8.0]: 0.12 ± 0.03

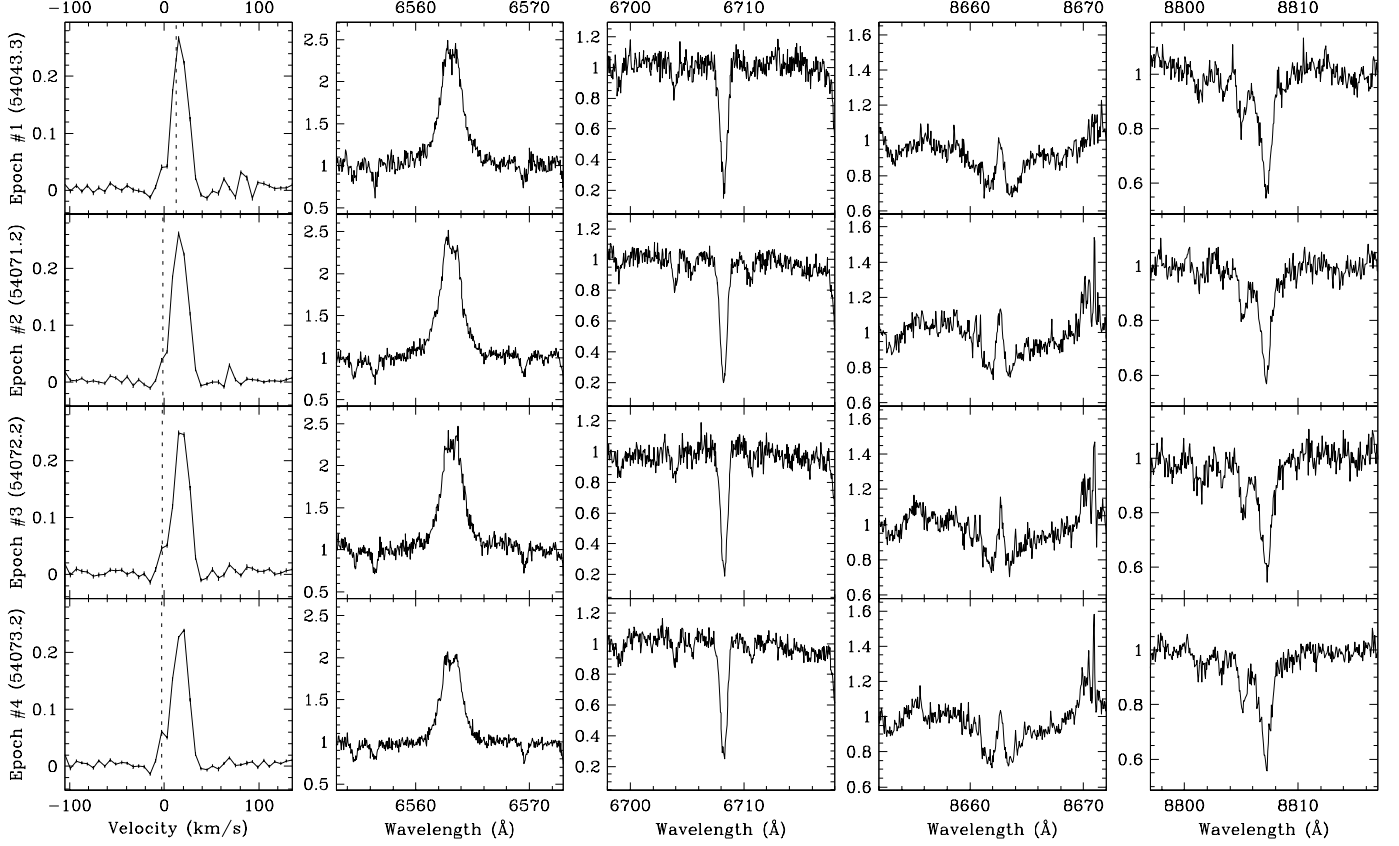
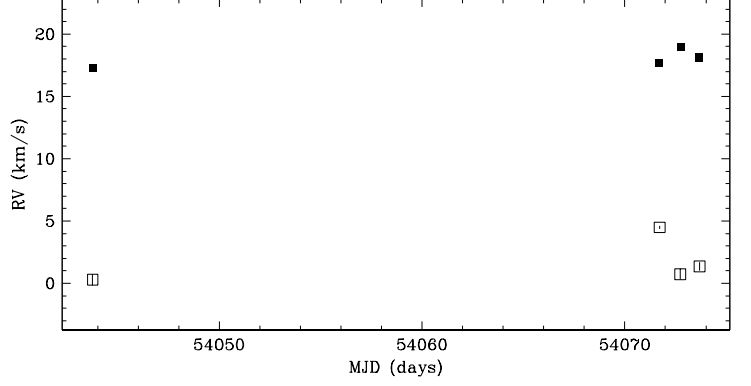


FIG. 37.— Hubble 4 is a suspected SB2. If star spots are responsible for the asymmetries in the broadening function, based on observed $v \sin i$ (~ 16 km s $^{-1}$) and model stellar radius ($\sim 1.4 R_{\odot}$), one would expect variations on a maximum timescale of ~ 4.3 days. From the constant broadening functions of the second observing run (epochs #2, #3 and #4) which span 2.0 days, it is unlikely that the broadening function irregularities are the result of star spots. By fitting the broadening function to two rotational broadening line profiles, we estimate the two sources have a flux ratio of 0.20 ± 0.05 , and the A and B sources have $v \sin i$ of 12.1 ± 0.3 km s $^{-1}$ and 13.1 ± 1.9 km s $^{-1}$, respectively. This target has been previously reported by Leinert et al. (1993), and Ghez et al. (1993) to have no resolved companions.

TABLE 2
MEASUREMENTS OF STARS WITHOUT CLOSE COMPANIONS IN CHA I &
TAU-AUR

Object	R.A. (J2000.0)	Dec. (J2000.0)	SpT	TTS ^a	10% width ^{bc} (km s ⁻¹)	$v \sin i^{\text{de}}$ (km s ⁻¹)	\overline{RV}^f (km s ⁻¹)	σ_{RV}^g (km s ⁻¹)	σ_N^h (km s ⁻¹)	# of obs.
Cha I										
T4	10 56 30.45	-77 11 39.3	M0.5	c	341 ± 28	12.4 ± 0.4	15.30 ± 0.03	0.58	0.77	5
T5	10 57 42.20	-76 59 35.7	M3.25	c	324 ± 30	13.8 ± 0.9	16.55 ± 0.08	0.23	0.38	4
T6	10 58 16.77	-77 17 17.1	K0	c	284	34 ± 2	14.99 ± 0.08	1
T8	10 59 06.99	-77 01 40.4	K2	c	347	35 ± 2	14.99 ± 0.06	1
T10	11 00 40.22	-76 19 28.1	M3.75	c	252 ± 24	5.4 ± 0.8	15.69 ± 0.03	0.25	0.48	5
CHXR 9C A	11 01 18.75	-76 27 02.5	M0.5	w	106 ± 13	12.8 ± 0.2	14.50 ± 0.04	0.32	0.34	5
CHXR 9C Ba+Bb	11 01 18.75	-76 27 02.5	M1.5	w	132 ± 12	19.6 ± 0.8	14.89 ± 0.09	0.09	0.09	5
CHXR 71	11 02 32.65	-77 29 13.0	M3	w	117 ± 46	17.1 ± 1.3	15.54 ± 0.08	0.40	0.44	4
T12	11 02 55.05	-77 21 50.8	M4.5	c	262 ± 35	10.7 ± 0.2	14.82 ± 0.05	0.53	0.45	4
T14	11 04 09.09	-76 27 19.4	K5	c	550 ± 13	7.8 ± 0.2	15.13 ± 0.09	0.25	0.25	4
ISO 52	11 04 42.58	-77 41 57.1	M4	w	126 ± 15	9.9 ± 0.6	15.52 ± 0.06	0.18	0.27	4
CHXR 14N	11 04 51.00	-76 25 24.1	K8	w	114 ± 20	13.7 ± 0.6	14.90 ± 0.04	0.58	0.66	5
CHXR 14S	11 04 52.85	-76 25 51.5	M1.75	w	98 ± 14	5.7 ± 0.3	14.176 ± 0.015	0.089	0.091	4
T16	11 04 57.01	-77 15 56.9	M3	w	101	11.3 ± 0.9	14.9 ± 0.3	0.4	0.4	4
T20	11 05 52.61	-76 18 25.6	M1.5	w	192 ± 21	48.3 ± 1.4	14.0 ± 0.4	0.9	0.9	4
Hn 5	11 06 41.81	-76 35 49.0	M4.5	c	340 ± 20	7.8 ± 0.4	15.76 ± 0.07	0.51	0.88	4
T22	11 06 43.47	-77 26 34.4	M3	w	228	60 ± 10	16 ± 3	1	2	4
CHXR 20	11 06 45.10	-77 27 02.3	K6	w	Absorp.	14.6 ± 0.9	15.46 ± 0.06	1.18	0.10	3
CHXR 74	11 06 57.33	-77 42 10.7	M4.25	w	97 ± 7	5.8 ± 1.0	17.85 ± 0.03‡	0.25	0.33	4
CHXR 21	11 07 11.49	-77 46 39.4	M3	w	135 ± 61	48 ± 5	11 ± 2‡	3	3	4
T24	11 07 12.07	-76 32 23.2	M0.5	c	454 ± 53	10.5 ± 0.4	16.88 ± 0.03	0.09	0.13	4
T25	11 07 19.15	-76 03 04.8	M2.5	c	341 ± 62	12.6 ± 0.3	15.84 ± 0.06	0.11	0.08	4
T26	11 07 20.74	-77 38 07.3	G2	c	390	32.7 ± 1.6	12.04 ± 0.14‡	1
CHXR 76	11 07 35.19	-77 34 49.3	M4.25	w	89 ± 12	9.8 ± 0.6	14.19 ± 0.13	0.64	0.75	4
CHXR 28 Aa+Ab	11 07 55.89	-77 27 25.8	K3.5	?	...	8.7 ± 0.7	16.76 ± 0.05	0.02	0.02	2
ISO 126	11 08 02.98	-77 38 42.6	M1.25	c	381 ± 19	40 ± 7	14.0 ± 1.3	0.8	0.3	4
T33 A	11 08 15.10	-77 33 53.2	K3.5	w	95 ± 15	12.9 ± 0.5	13.00 ± 0.05	0.23	0.10	4
T33 B	11 08 15.10	-77 33 53.2	G7	c	318 ± 21	50 ± 4	7 ± 2‡	3	3	4
T34	11 08 16.49	-77 44 37.2	M3.75	w	84 ± 8	5.8 ± 0.8	15.58 ± 0.03	0.21	0.35	5
T35	11 08 39.05	-77 16 04.2	K8	c	466 ± 46	21.0 ± 1.8	16.90 ± 0.19	1.07	0.93	6
CHXR 33	11 08 40.69	-76 36 07.8	M0	w	153 ± 3	16.5 ± 1.5	18.71 ± 0.08‡	0.30	0.30	2
T38	11 08 54.64	-77 02 13.0	M0.5	c	389 ± 23	18.7 ± 1.5	16.0 ± 0.5	4.2	9.9	4
T39 Aa	11 09 11.72	-77 29 12.5	K7	w	131 ± 27	7.7 ± 1.6	14.97 ± 0.04	0.67	0.59	6
T39 Ab	11 09 11.72	-77 29 12.5	M1.5	w	100 ± 16	4.1 ± 0.3	14.258 ± 0.012	0.191	0.261	5
CHXR 37	11 09 17.70	-76 27 57.8	K7	w	178 ± 11	15.8 ± 0.6	14.82 ± 0.06	0.23	0.23	2
CHXR 79	11 09 18.13	-76 30 29.2	M1.25	w	103 ± 50	12.4 ± 1.5	12.3 ± 1.0‡	1.4	1.4	4
T40	11 09 23.79	-76 23 20.8	K6	c	498 ± 78	15.02 ± 0.14	11.0 ± 1.0‡	2.7	2.7	2
CHXR 40	11 09 40.07	-76 28 39.2	M1.25	w	104 ± 18	11.6 ± 0.5	14.46 ± 0.02	0.05	0.01	4
Hn 10E	11 09 46.21	-76 34 46.4	M3.25	c	377 ± 17	8.2 ± 0.5	14.03 ± 0.10	0.68	0.94	4
T43	11 09 54.08	-76 29 25.3	M2	c	225 ± 98	18.2 ± 1.0	16.5 ± 2.0	1.4	1.5	4
T45	11 09 58.74	-77 37 08.9	K8	c	472 ± 6	6.6 ± 0.3	15.28 ± 0.06	0.97	0.97	2
T44	11 10 00.11	-76 34 57.9	K5	c	614 ± 53	71 ± 3	15 ± 3	6	4	4
T45A	11 10 04.69	-76 35 45.3	M0	c	340 ± 77	12.4 ± 0.5	16.94 ± 0.06	0.20	0.20	2
T46	11 10 07.04	-76 29 37.7	K8	c	437 ± 27	5.7 ± 0.9	14.79 ± 0.04	<0.01	<0.01	2
ISO 237	11 10 11.42	-76 35 29.3	K5.5	?	...	19.8 ± 1.3	14.9 ± 0.3	0.8	0.8	4
T47	11 10 49.60	-77 17 51.8	M2	c	395 ± 18	16.2 ± 0.9	14.2 ± 0.7	0.7	1.4	4
CHXR 48	11 11 34.75	-76 36 21.1	M2.5	w	110 ± 12	13.8 ± 0.5	15.29 ± 0.05	0.24	0.33	4
T49	11 11 39.66	-76 20 15.2	M2	c	280 ± 25	8.2 ± 0.8	16.26 ± 0.05	0.39	0.40	5
CHX 18N	11 11 46.32	-76 20 09.2	K6	w	188 ± 39	26.5 ± 1.3	15.29 ± 0.07	0.91	0.96	5
T50	11 12 09.85	-76 34 36.6	M5	c	262 ± 52	12.0 ± 0.4	14.62 ± 0.06	0.74	0.61	4
T51	11 12 24.41	-76 37 06.4	K3.5	c	381 ± 32	32.7 ± 1.1	13.32 ± 0.08	0.81	0.81	2

TABLE 2 — *Continued*

Object	R.A. (J2000.0)	Dec. (J2000.0)	SpT	TTS ^a	10% width ^{bc} (km s ⁻¹)	$v \sin i^{\text{de}}$ (km s ⁻¹)	\overline{RV}^i (km s ⁻¹)	σ_{RV}^g (km s ⁻¹)	σ_N^h (km s ⁻¹)	# of obs.
T52	11 12 27.72	-76 44 22.3	G9	c	562	28 ± 3	14.52 ± 0.08	1
T53	11 12 30.93	-76 44 24.1	M1	c	468 ± 22	22.2 ± 0.6	14.8 ± 0.2	1.5	1.5	5
CHXR 54	11 12 42.10	-76 58 40.0	M1	w	120 ± 22	10.9 ± 0.2	15.58 ± 0.03	0.20	0.21	5
T54	11 12 42.69	-77 22 23.1	G8	w	Absorp.	11.3 ± 2.0	13.27 ± 0.03	0.74	0.74	2
CHXR 55	11 12 43.00	-76 37 04.9	K4.5	?	...	14.8 ± 0.8	13.35 ± 0.08	0.91	0.91	2
Hn 17	11 12 48.61	-76 47 06.7	M4	w	72 ± 10	8.7 ± 0.5	14.53 ± 0.05	0.14	0.16	4
CHXR 57	11 13 20.13	-77 01 04.5	M2.75	w	100 ± 15	11.8 ± 1.2	16.30 ± 0.03	0.16	0.20	4
Hn 18	11 13 24.46	-76 29 22.7	M3.5	w	121 ± 24	7.6 ± 0.8	15.01 ± 0.04	0.39	0.04	5
CHXR 59	11 13 27.37	-76 34 16.6	M2.75	w	107 ± 20	11.0 ± 1.1	15.59 ± 0.03	0.41	0.41	4
CHXR 60	11 13 29.71	-76 29 01.2	M4.25	w	95 ± 12	0.8 ± 0.7	19.09 ± 0.04‡	0.12	0.14	4
CHXR 62	11 14 15.65	-76 27 36.4	M3.75	w	158 ± 33	35 ± 3	16.2 ± 0.4	0.7	1.6	5
Hn 21W	11 14 24.54	-77 33 06.2	M4	c	375 ± 31	19.1 ± 1.1	15.5 ± 0.3	0.4	0.1	4
B53	11 14 50.32	-77 33 39.0	M2.75	w	107 ± 18	8.3 ± 1.3	14.741 ± 0.017	0.070	0.039	4
T56	11 17 37.01	-77 04 38.1	M0.5	c	346 ± 41	7.2 ± 0.5	14.923 ± 0.013	0.189	0.165	6
CHXR 68 Aa+Ab	11 18 20.24	-76 21 57.6	K6	w	106 ± 22	8.8 ± 1.0	15.38 ± 0.04	0.23	0.26	4
CHXR 68 B	11 18 20.24	-76 21 57.6	M1	w	90 ± 17	8.3 ± 0.3	15.31 ± 0.05	0.11	0.09	4
Tau-Aur										
NTTS 034903+2431 ...	03 52 02.24	+24 39 47.9	K5	w	229 ± 31	36 ± 2	3.66 ± 0.10‡	0.23	0.22	4
NTTS 035120+3154SW	03 54 29.51	+32 03 01.4	G0	w	Absorp.	62 ± 3	10.7 ± 0.4	1.0	0.8	4
RX J0403.3+1725	04 03 24.95	+17 24 26.2	K3	?	...	111 ± 7	15.2 ± 0.7	2.8	2.8	4
RX J0405.1+2632	04 05 12.34	+26 32 43.9	K2	w	Absorp.	17.5 ± 1.3	7.091 ± 0.015‡	0.181	0.207	4
RX J0405.3+2009	04 05 19.59	+20 09 25.6	K1	w	Absorp.	24.1 ± 1.4	14.427 ± 0.012	0.187	0.190	4
HD284135	04 05 40.58	+22 48 12.2	G0	w	Absorp.	72 ± 4	14.23 ± 0.10	0.37	0.34	4
HD284149	04 06 38.79	+20 18 11.1	F8	w	Absorp.	27.0 ± 1.9	12.46 ± 0.03	0.30	0.15	5
RX J0406.8+2541 B ...	04 06 51.35	+25 41 28.3	K6.5	c	295	18 ± 2	16.01 ± 0.20	1
RX J0407.8+1750	04 07 53.99	+17 50 25.8	K4	w	115 ± 17	28.7 ± 1.0	12.47 ± 0.05	0.34	0.27	4
RX J0409.1+2901	04 09 09.74	+29 01 30.6	G8	w	Absorp.	24 ± 2	9.52 ± 0.03‡	0.13	0.14	4
RX J0409.2+1716	04 09 17.00	+17 16 08.2	M1	w	223 ± 23	70.5 ± 1.1	16.1 ± 0.5	1.3	1.5	5
RX J0409.8+2446	04 09 51.13	+24 46 21.1	M1	w	83 ± 8	5.9 ± 0.4	12.330 ± 0.012	0.170	0.208	4
RX J0412.8+1937	04 12 50.64	+19 36 58.2	K6	w	96 ± 16	11.2 ± 0.8	16.37 ± 0.02	0.38	0.47	5
HD285579	04 12 59.88	+16 11 48.2	G0	w	Absorp.	9.6 ± 1.1	7.805 ± 0.006‡	0.142	0.142	6
LkCa 1	04 13 14.14	+28 19 10.8	M4	w	173	30.9 ± 1.1	9.57 ± 0.12‡	1
RX J0413.4+3352	04 13 27.29	+33 52 41.7	K0	?	...	16.0 ± 1.7	18.13 ± 0.09	1
CW Tau	04 14 17.00	+28 10 57.8	K3	c	647 ± 7	33 ± 5	13.60 ± 0.10	3.01	2.55	5
FP Tau	04 14 47.31	+26 46 26.4	M4	c	378 ± 12	32 ± 2	16.26 ± 0.15	0.97	1.08	4
CX Tau	04 14 47.86	+26 48 11.0	M2	c	319	19.8 ± 0.6	16.63 ± 0.12	1
RX J0415.3+2044	04 15 22.92	+20 44 17.0	K0	w	Absorp.	35 ± 3	13.84 ± 0.03	0.37	0.25	5
LkCa 4	04 16 28.11	+28 07 35.8	K7	w	198 ± 30	30 ± 2	15.77 ± 0.11	3.34	4.00	4
CY Tau	04 17 33.73	+28 20 46.9	M1.5	c	415 ± 28	10.6 ± 0.4	16.68 ± 0.02	1.06	1.21	4
LkCa 5	04 17 38.94	+28 33 00.5	M2	w	163	38.3 ± 1.1	15.83 ± 0.16	1
NTTS 041529+1652 ...	04 18 21.47	+16 58 47.0	K5	w	Absorp.	5.1 ± 1.3	15.818 ± 0.020	0.180	0.202	5
V410 Tau	04 18 31.10	+28 27 16.2	K7	c	450 ± 106	83 ± 4	19.9 ± 0.3	1.3	1.5	4
DD Tau A	04 18 31.13	+28 16 29.0	M2	c	363	11.5 ± 1.4	13.9 ± 0.6	1
NTTS 041559+1716 ...	04 18 51.70	+17 23 16.6	K7	w	210 ± 29	74 ± 4	15.5 ± 0.3	3.0	2.9	5
BP Tau	04 19 15.84	+29 06 26.9	K5	c	458 ± 28	13.1 ± 1.6	15.24 ± 0.04	0.09	0.10	4
V819 Tau	04 19 26.26	+28 26 14.3	K7	w	166 ± 41	9.1 ± 0.6	16.64 ± 0.02	0.77	0.94	5
LkCa 7	04 19 41.27	+27 49 48.5	K7	w	154 ± 7	14.7 ± 1.2	17.98 ± 0.04	0.21	0.21	2
RX J0420.3+3123	04 20 24.12	+31 23 23.7	K4	?	...	9.6 ± 0.6	13.99 ± 0.03	1
DE Tau	04 21 55.64	+27 55 06.1	M1	c	453 ± 6	9.7 ± 0.3	15.402 ± 0.018	0.105	0.126	4
HD283572	04 21 58.84	+28 18 06.6	G2	w	Absorp.	79 ± 3	14.22 ± 0.08	0.94	1.30	4
T Tau A	04 21 59.43	+19 32 06.4	K1.5	c	430 ± 23	23.0 ± 1.2	19.23 ± 0.02	0.30	0.06	3
LkCa 21	04 22 03.14	+28 25 39.0	M3	c	277	46 ± 3	14.3 ± 0.3	1
HD285751	04 23 41.33	+15 37 54.9	G5	w	125	26.6 ± 1.4	15.22 ± 0.03	0.27	0.27	5
BD +26 718B	04 24 49.04	+26 43 10.4	K0	w	Absorp.	32.4 ± 1.8	16.23 ± 0.04	1.12	1.17	4

TABLE 2 — *Continued*

Object	R.A. (J2000.0)	Dec. (J2000.0)	SpT	TTS ^a	10% width ^{bc} (km s ⁻¹)	$v \sin i^{\text{de}}$ (km s ⁻¹)	\overline{RV}^i (km s ⁻¹)	σ_{RV}^g (km s ⁻¹)	σ_N^h (km s ⁻¹)	# of obs.
IP Tau	04 24 57.08	+27 11 56.5	M0	c	333 \pm 54	12.3 \pm 0.8	16.24 \pm 0.03	0.62	0.73	5
DG Tau	04 27 04.70	+26 06 16.3	K6	c	484	24.7 \pm 0.7	15.4 \pm 0.6	1
BD +17 724B	04 27 05.97	+18 12 37.2	G5	w	Absorp.	49 \pm 3	16.97 \pm 0.06	0.14	0.18	4
NTTS 042417+1744 ...	04 27 10.56	+17 50 42.6	K1	w	Absorp.	17.6 \pm 1.5	15.324 \pm 0.015	0.241	0.214	4
DH Tau	04 29 41.56	+26 32 58.3	M1	c	348	10.9 \pm 0.6	16.52 \pm 0.04	1
DI Tau	04 29 42.48	+26 32 49.3	M0	w	120 \pm 19	12.5 \pm 0.6	15.103 \pm 0.020	0.266	0.192	4
IQ Tau	04 29 51.56	+26 06 44.9	M0.5	c	411 \pm 48	14.4 \pm 0.3	15.83 \pm 0.03	0.25	0.27	5
UX Tau	04 30 04.00	+18 13 49.4	K2	c	513 \pm 44	23.6 \pm 1.8	15.45 \pm 0.02	2.28	2.90	4
FX Tau A	04 30 29.61	+24 26 45.0	M2	c	281 \pm 67	9.61 \pm 0.19	16.363 \pm 0.013	0.179	0.223	4
FX Tau B	04 30 29.61	+24 26 45.0	M1	c	413 \pm 53	7.9 \pm 0.3	17.332 \pm 0.015	0.236	0.185	4
DK Tau A	04 30 44.25	+26 01 24.5	K7	c	461 \pm 54	17.5 \pm 1.2	16.29 \pm 0.05	0.42	0.29	4
DK Tau B	04 30 44.25	+26 01 24.5	M1	c	397 \pm 35	14.0 \pm 0.8	14.70 \pm 0.10	0.85	1.78	5
RX J0430.8+2113	04 30 49.18	+21 14 10.6	G8	w	Absorp.	41 \pm 4	15.09 \pm 0.03	0.55	0.30	4
HD284496	04 31 16.86	+21 50 25.3	G0	w	Absorp.	20.0 \pm 1.0	14.414 \pm 0.019	0.329	0.307	4
NTTS 042835+1700 ...	04 31 27.17	+17 06 24.9	K5	w	84 \pm 7	14.8 \pm 1.3	16.63 \pm 0.04	0.38	0.43	4
XZ Tau	04 31 40.07	+18 13 57.2	M3	c	341 \pm 13	15.0 \pm 1.2	18.30 \pm 0.04	0.18	0.20	4
V710 Tau A	04 31 57.79	+18 21 38.1	M0.5	w	192	21.5 \pm 0.4	15.75 \pm 0.15	1
V710 Tau B	04 31 57.79	+18 21 38.1	M2	c	371	18.31 \pm 0.19	17.72 \pm 0.09	1
L1551-51	04 32 09.27	+17 57 22.8	K7	w	146 \pm 26	32.1 \pm 1.4	18.39 \pm 0.10	0.63	0.59	4
V827 Tau	04 32 14.57	+18 20 14.7	K7	w	168 \pm 15	20.9 \pm 1.3	17.77 \pm 0.05	1.67	1.91	4
V928 Tau	04 32 18.86	+24 22 27.1	M0.5	w	178 \pm 60	31.6 \pm 0.7	15.38 \pm 0.16	1.67	2.02	4
GG Tau A	04 32 30.35	+17 31 40.6	K7	c	512 \pm 10	11.5 \pm 0.7	18.08 \pm 0.03	0.16	0.19	4
RX J0432.7+1853	04 32 42.43	+18 55 10.2	K1	w	Absorp.	25.2 \pm 1.6	21.834 \pm 0.013	0.128	0.106	4
UZ Tau A	04 32 43.04	+25 52 31.1	M1	c	438 \pm 41	19.3 \pm 0.5	18.03 \pm 0.08	0.57	0.58	6
L1551-55	04 32 43.73	+18 02 56.3	K7	w	94 \pm 9	7.7 \pm 0.7	18.264 \pm 0.013	0.158	0.120	4
RX J0432.8+1735	04 32 53.24	+17 35 33.8	M2	w	105 \pm 4	11.18 \pm 0.11	18.039 \pm 0.015	0.243	0.344	5
GH Tau	04 33 06.22	+24 09 34.0	M1.5	c	472 \pm 38	30.3 \pm 0.7	16.70 \pm 0.10	1.01	1.12	4
V807 Tau	04 33 06.64	+24 09 55.0	K7	c	408 \pm 18	13.6 \pm 0.7	16.85 \pm 0.03	0.32	0.30	4
V830 Tau	04 33 10.03	+24 33 43.4	K7	w	121	32.0 \pm 1.5	18.2 \pm 0.2	1
GI Tau	04 33 34.06	+24 21 17.0	K7	c	302 \pm 45	12.7 \pm 1.9	17.29 \pm 0.04	1.08	1.00	4
RX J0433.5+1916	04 33 34.67	+19 16 48.9	G6	w	Absorp.	58 \pm 3	21.9 \pm 0.4	4.1	4.1	5
DL Tau	04 33 39.06	+25 20 38.2	G	c	581 \pm 6	19 \pm 4	13.94 \pm 0.14	0.86	1.03	5
HN Tau A	04 33 39.35	+17 51 52.4	K5	c	595 \pm 48	39 \pm 10	4.6 \pm 0.6 \ddagger	11.6	12.6	4
DM Tau	04 33 48.72	+18 10 10.0	M1	c	376 \pm 27	4.0 \pm 0.7	18.607 \pm 0.011	0.100	0.109	4
HBC 407	04 34 18.04	+18 30 06.7	G8	w	Absorp.	8.8 \pm 1.8	17.75 \pm 0.03	1
AA Tau	04 34 55.42	+24 28 53.2	K7	c	402 \pm 89	12.8 \pm 1.1	16.98 \pm 0.04	0.62	0.26	4
FF Tau	04 35 20.90	+22 54 24.2	K7	w	160 \pm 86	5.6 \pm 0.8	14.165 \pm 0.015	0.141	0.139	5
HBC 412 A	04 35 24.51	+17 51 43.0	M1.5	w	105 \pm 4	4.9 \pm 0.3	18.587 \pm 0.012	0.024	0.024	2
HBC 412 B	04 35 24.51	+17 51 43.0	M1.5	w	104 \pm 6	4.1 \pm 0.2	18.295 \pm 0.012	0.168	0.168	2
DN Tau	04 35 27.37	+24 14 58.9	M0	c	336 \pm 16	12.3 \pm 0.6	16.30 \pm 0.02	0.24	0.32	5
HQ Tau	04 35 47.34	+22 50 21.7	K0	c	442 \pm 93	48 \pm 2	16.65 \pm 0.11	0.85	0.81	4
HP Tau/G2	04 35 54.15	+22 54 13.5	G0	w	Absorp.	127 \pm 4	16.6 \pm 1.0	1.4	1.3	4
RX J0435.9+2352	04 35 56.83	+23 52 05.0	M1	w	125 \pm 21	4.2 \pm 0.5	16.605 \pm 0.011	0.129	0.139	4
LkCa 14	04 36 19.09	+25 42 59.0	M0	w	122 \pm 20	22.7 \pm 1.0	16.65 \pm 0.04	0.32	0.36	5
HD283759	04 36 49.12	+24 12 58.8	F2	w	Absorp.	57 \pm 6	32.1 \pm 0.2 \ddagger	1.2	1.5	4
RX J0437.2+3108	04 37 16.86	+31 08 19.5	K4	w	82 \pm 9	11.3 \pm 0.8	15.718 \pm 0.016	0.441	0.417	4
RX J0438.2+2023	04 38 13.04	+20 22 47.1	K2	w	Absorp.	16.1 \pm 1.7	14.954 \pm 0.016	0.519	0.579	4
RX J0438.2+2302	04 38 15.62	+23 02 27.6	M1	w	111 \pm 29	4.5 \pm 0.4	16.493 \pm 0.009	0.201	0.318	4
RX J0438.4+1543	04 38 27.66	+15 43 38.0	K3	?	...	6 \pm 2	15.211 \pm 0.009	0.126	0.126	5
DO Tau	04 38 28.58	+26 10 49.4	M0	c	480 \pm 56	10.5 \pm 1.0	16.04 \pm 0.17	1.86	2.00	5
HD285957	04 38 39.07	+15 46 13.7	K2	w	Absorp.	22.5 \pm 1.2	17.991 \pm 0.015	0.370	0.385	4
VY Tau	04 39 17.41	+22 47 53.4	M0	w	124 \pm 16	5.8 \pm 1.0	17.716 \pm 0.016	0.320	0.357	5
LkCa 15	04 39 17.80	+22 21 03.5	K5	c	451 \pm 51	13.9 \pm 1.2	17.65 \pm 0.03	0.65	0.69	5
IW Tau	04 41 04.71	+24 51 06.2	K7	w	170 \pm 32	8.7 \pm 0.8	15.880 \pm 0.010	0.259	0.264	5
CoKu Tau/4	04 41 16.81	+28 40 00.1	M1	w	185 \pm 33	25.8 \pm 0.4	15.98 \pm 0.04	0.42	0.40	7
HD283798	04 41 55.16	+26 58 49.5	G2	w	Absorp.	25.2 \pm 1.2	13.774 \pm 0.014	0.140	0.082	4

TABLE 2 — *Continued*

Object	R.A. (J2000.0)	Dec. (J2000.0)	SpT	TTS ^a	10% width ^{bc} (km s ⁻¹)	$v \sin i^{\text{de}}$ (km s ⁻¹)	\overline{RV}^i (km s ⁻¹)	σ_{RV}^g (km s ⁻¹)	σ_N^h (km s ⁻¹)	# of obs.
RX J0444.3+2017	04 44 23.55	+20 17 17.5	K1	?	...	60 ± 3	15.09 ± 0.16	0.90	0.94	5
HD30171	04 45 51.29	+15 55 49.7	G5	w	Absorp.	108 ± 4	21.13 ± 0.17	1.37	1.24	4
V1001 Tau A	04 46 58.98	+17 02 38.2	K6	c	525 ± 48	12.1 ± 1.2	22.45 ± 0.05‡	0.72	...	2
V1001 Tau B	04 46 58.98	+17 02 38.2	K6	c	405 ± 24	7.0 ± 0.3	21.74 ± 0.08	0.50	1.41	3
DR Tau	04 47 06.21	+16 58 42.8	K4	c	370 ± 7	6.26 ± 0.12	21.10 ± 0.04	0.19	0.16	5
RX J0447.9+2755 A ...	04 48 00.44	+27 56 19.6	G2.5	w	Absorp.	30.5 ± 1.8	16.29 ± 0.10	1.03	1.03	2
RX J0447.9+2755 B ...	04 48 00.44	+27 56 19.6	G2	w	Absorp.	27.9 ± 1.4	15.67 ± 0.04	0.97	0.97	3
RX J0450.0+2230	04 50 00.20	+22 29 57.5	K1	?	...	57 ± 3	15.04 ± 0.08	0.13	0.12	4
UY Aur A	04 51 47.38	+30 47 13.5	K7	c	324 ± 19	23.8 ± 1.3	13.92 ± 0.07	0.87	0.97	5
RX J0452.5+1730	04 52 30.75	+17 30 25.8	K4	w	89	8.8 ± 0.6	16.820 ± 0.010	0.196	0.222	4
RX J0452.8+1621	04 52 50.15	+16 22 09.2	K6	w	123 ± 12	24.9 ± 1.2	19.28 ± 0.06	0.40	0.40	4
RX J0452.9+1920	04 52 57.08	+19 19 50.4	K5	w	89 ± 8	4.8 ± 1.3	14.699 ± 0.010	0.117	0.107	4
HD31281	04 55 09.62	+18 26 30.9	G0	w	Absorp.	79 ± 4	14.57 ± 0.12	0.26	0.20	4
GM Aur	04 55 10.98	+30 21 59.5	K7	c	505 ± 11	14.8 ± 0.9	15.15 ± 0.04	0.50	0.41	4
LkCa 19	04 55 36.96	+30 17 55.3	K0	w	154 ± 40	20.1 ± 1.1	13.578 ± 0.013	1.120	0.674	4
SU Aur	04 55 59.38	+30 34 01.6	G2	c	561 ± 58	59 ± 2	14.26 ± 0.05	0.40	0.25	4
RX J0456.2+1554	04 56 13.57	+15 54 22.0	K7	w	106 ± 20	9.7 ± 0.6	18.966 ± 0.016	0.092	0.106	4
HD286179	04 57 00.65	+15 17 53.1	G0	w	Absorp.	17.1 ± 1.2	10.069 ± 0.009‡	0.211	0.090	4
RX J0457.2+1524	04 57 17.67	+15 25 09.4	K1	w	Absorp.	42 ± 2	19.77 ± 0.03	0.70	0.75	4
RX J0458.7+2046	04 58 39.74	+20 46 44.1	K7	w	Absorp.	7.8 ± 0.5	19.043 ± 0.013	0.108	0.124	5
RX J0459.7+1430	04 59 46.17	+14 30 55.4	K4	w	53	14.5 ± 0.6	19.875 ± 0.012	0.150	0.092	4
V836 Tau	05 03 06.60	+25 23 19.7	K7	c	403 ± 58	13.4 ± 1.1	18.15 ± 0.03	0.53	0.44	4
RX J0507.2+2437	05 07 12.07	+24 37 16.4	K6	w	126 ± 14	19.7 ± 1.0	18.74 ± 0.04	1.24	1.45	5
RW Aur B	05 07 49.54	+30 24 05.1	K1	c	618 ± 78	14.5 ± 1.8	15.00 ± 0.03	0.66	0.54	4

^a c: Classical T Tauri star, w: Weak-lined T Tauri star, ?: Unknown.

^b The H α 10% widths were adopted from Nguyen et al. (2009a) where available, or measured using the same method otherwise.

^c The H α 10% width uncertainty does not correspond to the measurement uncertainty, but to the scatter in our multi-epoch data.

^d The $v \sin i$ were adopted from Nguyen et al. (2009a) where available, or measured using the same method, otherwise.

^e The $v \sin i$ uncertainty represents the combined measurement scatter between results using different template spectra, and over different epochs.

^f The symbol ‡ indicates that the overall radial velocity deviates from that of the associated star-forming region.

^g This is the weighted standard deviation of the radial velocity as described in §4.2.

^h This is the systematic noise of the radial velocity as described in §4.2.

TABLE 3
MEASUREMENTS OF STARS WITH CLOSE COMPANIONS IN CHA I & TAU-AUR

SB ^a type	Region	Object	R.A. (J2000.0)	Dec. (J2000.0)	SpT	TTS ^b	10% width ^{cd} (km s ⁻¹)	# of obs.	Comp.	$v \sin i^{\text{ef}}$ (km s ⁻¹)	Flux ^g ratio
SB1	Cha	T39 B	11 09 11.72	-77 29 12.5	M1.5	w	106 ± 13	5		12.8 ± 0.4	...
SB1	Tau	RX J0415.8+3100..	04 15 51.38	+31 00 35.6	G6	w	Absorp.	4		31.7 ± 1.9	...
SB1	Tau	RX J0457.5+2014..	04 57 30.66	+20 14 29.7	K3	w	Absorp.	4		33 ± 3	...
SB1?	Cha	T7	10 59 01.09	-77 22 40.7	K8	c	365 ± 76	6		11.3 ± 0.8	...
SB1?	Cha	CHXR 28 B	11 07 55.89	-77 27 25.8	G9	w	175	2		61 ± 4	...
SB1?	Tau	RY Tau	04 21 57.40	+28 26 35.5	F8	c	600 ± 24	4		48 ± 3	...
SB1?	Tau	CI Tau	04 33 52.00	+22 50 30.2	G	c	572 ± 9	4		13 ± 2	...
SB2	Cha	CHXR 12	11 03 56.83	-77 21 33.0	M3.5	w	101 ± 8	6	A	8.99 ± 0.14	...
									B	8 ± 2	0.20 ± 0.08
SB2	Cha	T42	11 09 53.41	-76 34 25.5	K5	c	543 ± 83	7	A	11.4 ± 1.1	...
									B	11.5 ± 1.5	0.8 ± 0.3
SB2	Tau	V826 Tau	04 32 15.84	+18 01 38.7	K7	w	139 ± 13	5	A	8.5 ± 0.5	...
									B	9.3 ± 0.7	0.88 ± 0.06
SB2	Tau	DQ Tau	04 46 53.05	+17 00 00.2	M0	c	340 ± 22	4	A	14.7 ± 1.6	...
									B	11.3 ± 0.7	0.78 ± 0.18
SB2	Tau	HBC 427	04 56 02.02	+30 21 03.8	K5	w	145 ± 13	4	A	9.9 ± 0.3	...
									B	14.5 ± 0.5	0.157 ± 0.014
SB2 [†]	Cha	T21	11 06 15.41	-77 21 56.8	G5	w	Absorp.	1	A	94.1 ± 0.7	...
									B	14.5 ± 0.3	0.101 ± 0.005
SB2 [†]	Cha	CHXR 47	11 10 38.02	-77 32 39.9	K3	w	Absorp.	2	A	59.5 ± 0.4	...
									B	24 ± 3	0.24 ± 0.06
SB2 [†]	Tau	HD285281	04 00 31.07	+19 35 20.7	K0	w	Absorp.	4	A	78.0 ± 0.3	...
									B	17.0 ± 1.9	0.07 ± 0.05
SB2 [†]	Tau	RX J0406.8+2541 A	04 06 51.35	+25 41 28.3	K4.5	c	277 ± 74	2	a	47 ± 4	...
									b	9.8 ± 0.3	0.32 ± 0.07
SB2 [†]	Tau	DF Tau	04 27 02.80	+25 42 22.3	M3	c	369 ± 19	4	A	46.6 ± 1.8	...
									B	9.8 ± 0.6	0.49 ± 0.11
SB2 [†]	Tau	RX J0441.4+2715..	04 41 24.00	+27 15 12.4	G8	w	Absorp.	4	A	37.0 ± 0.6	...
									B	12.6 ± 1.5	0.32 ± 0.07
SB2 [†]	Tau	RX J0443.4+1546..	04 43 25.97	+15 46 03.9	G7	w	Absorp.	4	A	86.5 ± 1.6	...
									B	24.0 ± 0.8	0.83 ± 0.10
SB2 [†]	Tau	RX J0455.7+1742..	04 55 47.67	+17 42 02.0	K3	w	Absorp.	4	A	8 ± 2	...
									B	9.5 ± 0.4	0.337 ± 0.014
SB2?	Cha	T11	11 02 24.91	-77 33 35.7	K6	c	367 ± 38	4	A	11.2 ± 0.3	...
									B	13.0 ± 0.3	1.0 ± 0.4
SB2?	Cha	Hn 4	11 05 14.67	-77 11 29.1	M3.25	w	176 ± 126	4	A	9.0 ± 0.5	...
									B	90 ± 15	0.62 ± 0.09
SB2?	Cha	T31 A	11 08 01.49	-77 42 28.9	K3	c	471 ± 55	3	a	13 ± 2	...
									b	13 ± 3	0.7 ± 0.3
SB2?	Tau	Hubble 4	04 18 47.04	+28 20 07.3	K7	w	188 ± 16	4	A	12.1 ± 0.3	...
									B	13.1 ± 1.9	0.20 ± 0.05
SB3	Cha	T55	11 13 33.57	-76 35 37.4	M4.5	w	165 ± 59	5	A	23 ± 2	...
									B	34 ± 4	0.38 ± 0.08
									C	31.0 ± 1.6	0.19 ± 0.08
SB3	Tau	RX J0412.8+2442..	04 12 51.22	+24 41 44.3	G9	w	Absorp.	3	A	28.50 ± 0.12	...
									B	15.1 ± 1.5	0.88 ± 0.12
									C	7.4 ± 0.3	0.36 ± 0.04
SB3	Tau	V773 Tau	04 14 12.92	+28 12 12.4	K3	c	433 ± 51	4	A	27 ± 4	...
									B	28 ± 4	1.0 ± 0.3
									C	21 ± 7	0.09 ± 0.06
SB3	Tau	LkCa 3	04 14 47.97	+27 52 34.7	M1	w	187 ± 25	4	Aa	12.0 ± 1.0	...
									Ab1	16 ± 2	0.75 ± 0.13
									Ab2	14 ± 4	0.21 ± 0.05

TABLE 3 — *Continued*

SB ^a type	Region	Object	R.A. (J2000.0)	Dec. (J2000.0)	SpT	TTS ^b	10% width ^{cd} (km s ⁻¹)	# of obs.	Comp.	$v \sin i$ ^{ef} (km s ⁻¹)	Flux ^g ratio
-------------------------	--------	--------	-------------------	-------------------	-----	------------------	--	--------------	-------	---	----------------------------

^a SB1: Single-lined spectroscopic binary, SB2: Double-lined spectroscopic binary, SB3: Triple-lined spectroscopic binary; ?: suspected, †: long-period.

^b c: Classical T Tauri star, w: Weak-lined T Tauri star, ?: Unknown.

^c The H α 10% widths were adopted from Nguyen et al. (2009a) where available, or measured using the same method otherwise.

^d The H α 10% width uncertainty does not correspond to the measurement uncertainty, but to the scatter in our multi-epoch data.

^e The $v \sin i$ were adopted from Nguyen et al. (2009a) where available, or measured using the same method for SB1s and the broadening function method described in §3.2 for SB2s and SB3s, otherwise.

^f The $v \sin i$ uncertainty represents the combined measurement scatter between results using different template spectra, and over different epochs.

^g The flux ratio is between the companion and the primary star, see §3.2.

TABLE 4
RADIAL VELOCITY MEASUREMENTS FOR CANDIDATE AND SUSPECTED SB2s IN
CHA I & TAU-AUR

Region	Object	MJD	RV_1 (km s $^{-1}$)	RV_2 (km s $^{-1}$)
Candidate Short-Period SB2s				
Cha	CHXR 12	53787.13005	3.49 ± 0.03	36.45 ± 0.30
		53836.09473	7.00 ± 0.01	27.98 ± 0.18
		53836.35925	8.00 ± 0.02	28.09 ± 0.36
		53837.05400	8.00 ± 0.02	27.78 ± 0.45
		54074.35810	17.76 ± 0.07	4.27 ± 0.42
Cha	T42	54075.28527	17.64 ± 0.07	3.98 ± 0.17
		53786.16759	-5.30 ± 0.28	32.30 ± 0.45
		53786.38541	-6.10 ± 0.69	33.74 ± 0.65
		53788.13175	-4.51 ± 0.31	31.11 ± 0.69
		53788.33456	-4.50 ± 0.05	31.67 ± 0.46
Tau	V826 Tau	53836.37795	-13.00 ± 0.25	25.82 ± 0.53
		54073.33792	0.99 ± 0.18	9.50 ± 0.07
		54075.27381	4.76 ± 0.39	11.83 ± 1.26
		54045.15674	1.49 ± 0.05	33.63 ± 0.15
		54071.07067	32.50 ± 0.02	2.50 ± 0.02
Tau	DQ Tau	54074.06213	31.48 ± 0.05	3.95 ± 0.17
		54074.29539	35.50 ± 0.01	1.50 ± 0.03
		54075.12450	29.82 ± 0.08	5.43 ± 0.14
		54043.29394	29.30 ± 0.19	7.76 ± 0.24
		54071.32764	38.23 ± 0.28	2.62 ± 0.20
Tau	HBC 427	54072.10274	38.13 ± 0.22	4.48 ± 0.21
		54074.31433	32.34 ± 0.28	5.58 ± 0.13
		54042.27028	5.25 ± 0.06	34.50 ± 0.02
		54043.26942	3.80 ± 0.05	31.67 ± 0.58
		54071.17361	4.42 ± 0.04	33.58 ± 0.49
		54073.23627	4.58 ± 0.04	34.10 ± 0.64
Candidate Long-Period SB2s				
Cha	T21	54073.36536	16.49 ± 0.58	8.46 ± 0.32
Cha	CHXR 47	54072.32956	17.50 ± 0.06	7.87 ± 0.49
Tau	HD285281	54075.30733	18.05 ± 0.67	6.50 ± 0.03
		54044.33142	15.55 ± 0.88	21.00 ± 0.01
		54071.26329	16.00 ± 0.13	21.37 ± 0.75
		54072.05828	14.79 ± 0.47	17.56 ± 15.16
		54074.21922	14.44 ± 0.43	16.44 ± 0.47
Tau	RX J0406.8+2541 A	54071.13966	21.18 ± 0.25	16.31 ± 0.08
Tau	DF Tau	54074.12534	15.82 ± 0.76	15.98 ± 0.16
		54045.21462	9.78 ± 0.84	16.96 ± 0.16
		54071.24608	9.49 ± 0.89	15.11 ± 0.31
		54072.16221	11.78 ± 0.61	15.44 ± 0.08
		54074.20299	11.10 ± 0.37	16.73 ± 0.09
Tau	RX J0441.4+2715 . .	54042.23259	22.00 ± 0.04	22.70 ± 0.16
		54071.19589	21.35 ± 0.20	21.85 ± 0.19
		54072.21185	21.56 ± 0.23	21.93 ± 0.18
		54073.16892	23.47 ± 0.32	22.48 ± 0.21
		54043.29064	7.50 ± 0.16	16.00 ± 0.01
Tau	RX J0443.4+1546 . .	54071.07395	6.45 ± 1.28	14.07 ± 0.14
		54073.31655	6.91 ± 0.87	15.67 ± 0.16
		54074.06749	7.96 ± 1.67	13.74 ± 0.37
		54044.37308	19.81 ± 0.08	4.01 ± 0.39
		54071.33319	20.50 ± 0.02	4.50 ± 0.05
Tau	RX J0455.7+1742 . .	54072.11740	20.17 ± 0.05	4.50 ± 0.07
		54074.31905	20.50 ± 0.03	2.46 ± 0.29
Suspected SB2s				
Cha	T11	53786.14279	9.95 ± 0.17	19.00 ± 0.01
		53786.32551	9.92 ± 0.17	19.50 ± 0.03
		53788.26188	10.12 ± 0.12	20.00 ± 0.01
		53836.41081	10.65 ± 0.14	24.13 ± 0.30
Cha	Hn 4	53788.27834	16.55 ± 0.05	2.00 ± 0.51
		53835.04491	15.48 ± 0.06	-2.00 ± 6.85
		53835.36297	15.98 ± 0.08	-3.48 ± 2.59
		53837.21652	15.05 ± 0.08	6.63 ± 3.23
Cha	T31 A	53788.26999	23.72 ± 0.29	5.79 ± 0.41
		53835.16847	27.16 ± 0.21	6.02 ± 0.37
		54071.37156	26.31 ± 0.26	2.51 ± 0.35
Tau	Hubble 4	54043.25711	17.27 ± 0.10	0.28 ± 0.45
		54071.21366	17.68 ± 0.10	4.49 ± 0.10
		54072.23986	18.95 ± 0.11	0.74 ± 0.41
		54073.18295	18.10 ± 0.10	1.36 ± 0.35

TABLE 4 — *Continued*

Region	Object	MJD	RV_1 (km s ⁻¹)	RV_2 (km s ⁻¹)
--------	--------	-----	------------------------------	------------------------------

TABLE 5
RADIAL VELOCITY MEASUREMENTS FOR CANDIDATE SB3s IN CHA I &
TAU-AUR

Region	Object	MJD	RV_1 (km s $^{-1}$)	RV_2 (km s $^{-1}$)	RV_3 (km s $^{-1}$)
Cha	T55	53786.19360	15.30 ± 0.16	66.46 ± 0.45	-56.74 ± 1.11
		53835.24146	16.52 ± 0.26	16.52?	16.52?
		53836.16456	13.50 ± 0.05	-31.93 ± 0.87	67.93 ± 2.64
		53837.32253	14.04 ± 0.28	56.51 ± 0.40	-45.00 ± 0.07
		54071.34865	14.84 ± 0.12	79.51 ± 0.60	-65.27 ± 0.67
Tau	RX J0412.8+2442	54071.24851	-25.50 ± 0.03	87.92 ± 0.11	32.50 ± 0.02
		54072.12813	-22.57 ± 0.20	86.02 ± 0.18	32.00 ± 0.03
		54074.20523	77.43 ± 0.32	-16.65 ± 0.12	32.48 ± 0.05
Tau	V773 Tau	54043.22853	10.80 ± 0.27	44.63 ± 0.35	-27.03 ± 0.41
		54071.20801	2.51 ± 0.10	40.71 ± 0.15	-19.00 ± 3.13
		54072.23483	3.39 ± 0.32	38.63 ± 0.26	-24.49 ± 1.29
Tau	LkCa 3	54074.15653	3.42 ± 0.46	45.25 ± 0.39	-26.00 ± 0.26
		54043.21590	12.77 ± 0.07	42.26 ± 0.12	-37.50 ± 0.02
		54071.22094	-5.13 ± 0.11	56.40 ± 0.19	-52.50 ± 0.37
		54072.24682	-6.12 ± 0.07	16.46 ± 0.13	61.53 ± 0.10
		54074.16123	-2.14 ± 0.09	6.67 ± 0.11	40.50 ± 0.10

TABLE 6
RADIAL VELOCITY MEASUREMENTS FOR CANDIDATE AND SUSPECTED SB1s IN
CHA I & TAU-AUR

Region	Object	MJD	RV (km s $^{-1}$)
Candidate SB1s			
Cha	T39 B	53788.30821	16.71 ± 0.10
		53835.18985	15.17 ± 0.20
		53836.07753	15.04 ± 0.47
		53837.02627	15.78 ± 0.08
Tau	RX J0415.8+3100	54074.36553	14.10 ± 0.13
		54043.24631	56.12 ± 0.35
		54071.18164	-13.81 ± 0.13
		54072.20036	53.74 ± 0.09
Tau	RX J0457.5+2014	54073.14788	-2.22 ± 0.15
		54043.34779	11.92 ± 0.06
		54071.31745	18.39 ± 0.07
		54072.13301	18.00 ± 0.05
		54074.28725	18.46 ± 0.05
Suspected SB1s			
Cha	T7	53786.16446	16.23 ± 0.10
		53786.34625	16.59 ± 0.10
		53788.31133	16.12 ± 0.11
		53836.38144	15.48 ± 0.32
		53836.41500	15.02 ± 0.34
Cha	CHXR 28 B	54071.36880	17.18 ± 0.09
		54072.36538	30.96 ± 2.83
Tau	RY Tau	54075.36595	23.36 ± 2.15
		54043.25397	19.37 ± 0.28
		54071.21608	16.72 ± 0.23
		54072.24213	16.96 ± 0.21
Tau	CI Tau	54073.18576	16.76 ± 0.22
		54043.29708	17.61 ± 0.09
		54071.12631	16.49 ± 0.08
		54073.28333	16.43 ± 0.10
		54074.11409	16.55 ± 0.10

TABLE 7
WIDE COMPANIONS IN CHA I & TAU-AUR

Object	Pairing	Separation (")	ΔK	<i>R</i> -band flux ratio ^a	References ^b
Cha I					
T5	A-B	0.159	0.05	0.87	6
T6	A-B	5.122	3.79	$\lesssim 0.01$	6
CHXR 9C A	A-Ba	0.852	0.36	0.56	6
CHXR 9C Ba+Bb	Ba-Bb	0.13	0.7	0.18	6
CHXR 71	A-B	0.572	1.63	0.02	6
T26	Ba-Bb	0.066	0.06	0.86	6
CHXR 28	Aa-Ab	0.143	0.4	0.55	6
ISO 126	A-B	0.292	0.66	0.23	6
T33	A-B	2.434	1.93	0.01	6
T39 A	Aa-Ab	1.242	0.31	0.44	6
CHXR 37	A-B	0.079	1.07	0.08	6
CHXR 79	A-B	0.885	2.45	0.01	6
CHXR 40	A-B	0.151	0.12	0.83	6
T43	A-B	0.796	1.41	0.02	6
T45	A-B	0.752	2.67	$\lesssim 0.01$	6
T46	A-B	0.123	1.57	0.01	6
T51	A-B	1.977	2.35	$\lesssim 0.01$	6
T54	A-B	0.247	1.45	0.19	6
CHXR 59	A-B	0.148	0.02	0.95	6
CHXR 62	A-B	0.12	0.06	0.86	6
Hn 21W	A-B	5.495	0.95	0.07	6
B53	A-B	0.295	1.52	0.02	6
CHXR 68 A	Aa-Ab	0.101	0.22	0.6	6
CHXR 68 B	Aa-B	4.367	0.95	0.08	6
Tau-Aur					
NTTS 034903+2431 ...	A-B	0.61	1.64	0.01	1
NTTS 035120+3154SW	A-B	8.6	0.28	0.67	1
HD284135	A-B	0.378	0.21	0.8	5
RX J0406.8+2541 B ...	A-B	0.977	0.04	0.94	5
RX J0409.1+2901	A-B	6.764-6.786	1.53-1.59	0.16-0.17	5
RX J0412.8+1937	A-B	2.568	1.05	0.1	5
RX J0413.4+3352	A-B	1.008	3.13	$\lesssim 0.01$	5
RX J0415.3+2044	A-B	0.589	1.92	0.06	5
V410 Tau	A-B	0.123	1.94-2.5	0-0.01	2,4
	AB-C	0.2871	2,4
DD Tau A	A-B	0.56-0.57	0.48-0.84	0.05-0.28	1,2
V819 Tau	A-B	10.5	3.64	$\lesssim 0.01$	1
LkCa 7	A-B	1.05	0.63	0.26	1
T Tau A	A-B	0.71-0.73	1.99-2.6	0-0.04	1,2
BD +26 718B	B-b	0.155-0.166	0.53-0.73	0.43-0.54	5
BD +17 724B	A-B	0.083-0.1	1.55-2.28	0.07-0.16	5
DI Tau	A-B	0.12	2.26-2.3	0.01	2,3
UX Tau	A-B	5.9	1.42	0.09	1
	A-C	2.7	2.9	0.09	1
FX Tau A	A-B	0.9-0.91	0.4-0.73	0.06-0.35	1,2,3
DK Tau	A-B	2.53-2.8	1.3-1.51	0.01-0.03	1,2,3
RX J0430.8+2113	A-B	0.389	3.58	$\lesssim 0.01$	5
HD284496	A-B	4.598	4.25	$\lesssim 0.01$	5
XZ Tau	A-B	0.3-0.311	0.73-1.14	0.04-0.07	1,2
V710 Tau	A-B	3.24	0.2	0.71	1
V827 Tau	A-B	0.0909	0.51	0.31	Priv.Comm.
V928 Tau	A-B	0.165-0.18	0.14-0.6	0.31-0.79	1,2,3
GG Tau A	A-a	0.2502-0.288	0.48-1.51	0.01-0.33	1,2,3,4
UZ Tau A	A-B	0.34-0.3678	0.5-1.11	0.03-0.37	1,2,3
GH Tau	A-B	0.314-0.35	0.1-0.64	0.22-0.86	1,2
V807 Tau	A-B	0.375-0.41	0.84-1.07	0.08-0.15	1,2
GI Tau	GK-GI	12.2	0.23	0.5	1
HN Tau A	A-B	3.1	3.44	$\lesssim 0.01$	1
FF Tau	A-B	0.026	1	0.1	3
HBC 412	A-B	0.7	0	1	1
HP Tau/G2	G2-G3	9.9-10	1.55	0.15	1,3
RX J0435.9+2352	A-B	0.069	1.28	0.02	5
	AB-C	11.315	1.92	0.02	5
RX J0437.2+3108	A-B	0.109	1.03	0.15	5
RX J0438.2+2023	A-B	0.464	0.1	0.87	5
RX J0438.2+2302	A-B	9.19	2.49	0.01	5
HD285957	A-B	9.463-9.504	1.74-1.84	0.04-0.05	5
	A-C	10.345-10.396	4.63-4.72	0.04-0.05	5
VY Tau	A-B	0.66	1.46-1.5	0.01-0.02	1,3
IW Tau	A-B	0.27	0-0.1	0.66-1	1,3

TABLE 7 — *Continued*

Object	Pairing	Separation (")	ΔK	<i>R</i> -band flux ratio ^a	References ^b
CoKu Tau/4.....	A–B	0.0536	0.2	0.73	7
HD283798.....	A–B	1.631	3.42	0.01	5
	AB–C	7.147	5.75	0.01	5
RX J0444.3+2017	A–B	9.868	2.45	0.01	5
HD30171.....	A–B	12.926	1.71	0.14	5
V1001 Tau A.....	A–B	2.7	0.87	0.17	1
RX J0447.9+2755 A ...	A–B	0.639	0.12	0.79	5
RX J0450.0+2230	A–B	2.072	3.74	$\lesssim 0.01$	5
	AB–C	8.361	3.7	~ 0.01	5
UY Aur A.....	A–B	0.88–0.89	1.14–1.38	0.02–0.06	1,2
RX J0452.8+1621	A–B	0.478	0.19	0.67	5
RX J0452.9+1920	A–B	0.425	1.85	0.01	5
HD286179.....	A–B	0.112	1.26	0.22	5
RX J0457.2+1524	A–B	0.57	0.05	0.94	5
RX J0458.7+2046	A–B	6.113	6.75	$\lesssim 0.01$	5
RW Aur B.....	A–B	1.5	1.6	0.08	1,2,4
	B–C	0.12	4.03	0.08	1,2,4

^a *R*-band flux ratios are given as the fainter object to the brighter object, and are derived from ΔK as outlined in §4.1.

^b (1) Leinert et al. (1993); (2) Ghez et al. (1993); (3) Simon et al. (1995); (4) Ghez et al. (1997b); (5) Kohler & Leinert (1998); (6) Lafrenière et al. (2008); (7) Ireland & Kraus (2008)